Effects of N and O-based Lewis base additives on crystallinity, carrier recombination and performance of perovskite solar cells

Muhammad Abdelshakour Muhammad Youssef

February 2022

Effects of N and O-based Lewis base additives on crystallinity, carrier recombination and performance of perovskite solar cells

Muhammad Abdelshakour Muhammad Youssef

Doctoral Program in Materials Science

Submitted to the Graduate School of

Pure and Applied Sciences

in Partial Fulfillment of the Requirements

for the Degree of Doctor of Philosophy in

Engineering

at the

University of Tsukuba

Abstract

In recent years, as global demand for environmentally friendly and renewable energy sources has continued to increase, photovoltaic technology has evolved tremendously as a possible route for solar energy conversion into electricity. With a power conversion efficiency (PCE) jump from 3.8% to 25.6% in the last decade and a low-cost manufacturing technique, perovskite solar cells (PSCs) have already been seen as an exciting development in photovoltaics. They've been considered one of the most promising technologies. Miyasaka et al. in 2009 were the first report on the organic–inorganic metal halide perovskite material as light absorbers in dye-sensitized solar cells (DSSCs). The next-generation solar cell devices based on this innovative material have made enormous progress. The perovskite material has several unique features, including excellent optoelectronic properties, long carrier recombination lifetime, small effective masses of electrons and holes, wide absorption of light and high carrier mobility. These amazing features have propelled PSCs to the forefront of the solar cell race, where they will face off against traditional silicon solar cells.

The surface and grain boundaries (GBs) of solution-fabricated perovskite films can easily create trap states, which serve as carrier recombination sites and impact the photovoltaic performance and the stability of the PSCs. Furthermore, the perovskite film possesses a higher sensitivity to moisture and air, which causes deterioration of the perovskite film and hence the device efficiency. In addition to the fast interaction between the perovskite precursor, which affect the crystallinity and morphology of the fabricated perovskite films. It is necessary to control the fabrication process of the PSCs with fewer defects, better morphology, improved crystallinity, reduced carrier recombination and higher stability. To accomplish these objectives, the main goal of this thesis is to investigate the effect of different types of N and O-based Lewis base additives on the crystallinity, carrier recombination, and the photovoltaic performance of the fabricated PSCs.

The low thermal stability of the $CH_3NH_3PbI_3$ ($MAPbI_3$) perovskite material led to evaporation of iodide ions from the perovskite crystal lattice during the fabrication process, which generates iodide vacancies and form undercoordinated Pb^{2+} defects. These defects form a net positive charge

on the perovskite lattice, which increase the recombination rate. The Lewis base additives were used to suppress these defects by neutralizing the formed positive charge. However, in perovskite films, the defect configuration created by solution processing or evaporation is substantially more complicated and defects can't by efficiently suppressed. A more effective and stronger Lewis base additives needed to suppress the defects efficiently. The using of bidentate Lewis base additives as trap passivators can form a more stable bond and thus block such defects efficiently, because it have two sites to interact with such defects. In this thesis, the passivation of surface defects in $CH_3NH_3PbI_3$ perovskite film was studied by incorporating two β-diketone Lewis base additives 2,4-pentanedione (acetylacetone; acac) and 3-methyl-2,4-nonanedione (R-acac) within the chlorobenzene antisolvent, which are not explored yet. When compared to the pristine PSC, the two β-diketone Lewis bases demonstrated greater passivation for the defects, resulting in PCE increases of 19% and 45 % for the acac and R-acac passivated PSCs, respectively. Additionally, their bidentate interaction with two carbonyl groups aids in the creation of a more stable bond with the under coordinated Pb^{2+} defects. As a result, the defects were effectively passivated, and the PSCs showed improved stability.

Although the Pb-PSCs have achieved a high PCE of 25.6%, which is one of the highest PCEs ever reported in solar cell generations, Pb is possibly hazardous to the ecosystem. The replacement of Ca^{2+} or Zn^{2+} in protein by the stable Pb^{2+} with a specific ionic radius can cause cytotoxicity. Simultaneously, the carcinogenic PbI_2 is a fairly water-soluble compound that can be generated through heat or moisture degradation of unstable perovskite materials. These negative environmental consequences obstruct the commercial implementation of Pb-PSCs. Fortunately, Sn is an excellent option for the non-toxic photovoltaic applications. Compared to Pb, the Sn metal is less poisonous and can form perovskite compounds with a variety of cations. Furthermore, a narrower bandgap, a lower exciton binding energy, and a smaller radius than Pb^{2+} are all advantages of Sn perovskite materials over their Pb analogs. Theoretically, the Sn-PSCs can reach a PCE over 33% due to their optimal bandgap, between 1.1 and 1.4 eV. Sn-PSCs, on the other hand, have critical drawbacks, such as rapid interaction between perovskite components in the precursor solution, which affects the

crystallinity and morphology of the generated perovskite films. Moreover, Sn^{2+} is quickly converted to Sn^{4+}, resulting in Sn vacancies in the $FASnI_3$ absorber layer.

In order to understand the parameters controlling the photovoltaic performance of Sn-PSCs, the chemistry of Sn^{2+} compounds, including their structural properties, nature of bonding, and the way of interaction were explained in this thesis. This allows to know about the interaction mechanism between Sn^{2+} halides and Lewis base additives during Sn-PSCs fabrication.

The quality of the fabricated Sn-PSCs could be improved by the inclusion of the Lewis base additives within the perovskite precursor, which working as a morphology controller. However, the faster recombination of the photo-generated electron-hole pairs is still crucial in Sn-PSCs and leads to performances and stability loss. The efficient electrons transportation from the Sn perovskite layer to the adjacent electron transport layer (ETL) has not been well explored in Sn-PSCs research, which can be a challenging factor for improving the photovoltaic performance. To facilitate the electron transportation from the $FASnI_3$ perovskite layer to the adjacent ETL, diaminomaleonitrile (DAMN) Lewis base additive was used in Sn-PSCs. DAMN, which has two cyano groups in its structure, can serve as an electron withdrawing group, extracting electrons from the perovskite layer and transferring them to the ETL. The results showed that the $FASnI_3$-DAMN based PSCs possess a 42% higher electron mobility compared to pristine $FASnI_3$ and the transient photocurrent decay lifetimes are accelerated by 2.3 times, revealing an enhancement in electron transportation after incorporation of DAMN. More importantly, the $FASnI_3$-DAMN perovskite absorbers also exhibited a decreased in charge carrier recombination rate, in addition to the simultaneous reduction of lattice strain of the $FASnI_3$-DAMN film. Consequently, the fabricated Sn-PSCs with $FASnI_3$-DAMN perovskites showed enhanced PCE of 8.11% and a highly light soaking stable performance of over 300 h when measured under maximum power point tracking conditions. However, the problem of easier oxidation of Sn^{2+} to Sn^{4+} increasing the carrier recombination and reduces the stability of Sn-PSCs.

In attempt to reduce the oxidation of Sn^{2+} to Sn^{4+} in Sn-PSCs another Lewis base additives formamidine sulfonic acid ($FASO_2H$) was added to the perovskite solution. The $FASO_2H$ Lewis base

additive was chosen because it is a strong reducing agent and it comes with the sulfonic group in structure, which is hydrophobic group. It was observed that, the utilizing of $FASO_2H$ Lewis base additive could diminish the oxidation of Sn^{2+} to Sn^{4+} due to its strong reduction ability. In addition to improving the crystallinity and the morphology of the perovskite film. Consequently, the PCE of the $FASnI_3$-$FASO_2H$-based PSCs increased to 7.43 % compared to 6.67% for the pristine $FASnI_3$-based PSCs. Most impressively, the $FASnI_3$-$FASO_2H$-based PSCs retained 90% of their initial PCE after 2880 hours of N_2 storage.

Contents

Chapter 1 Introduction

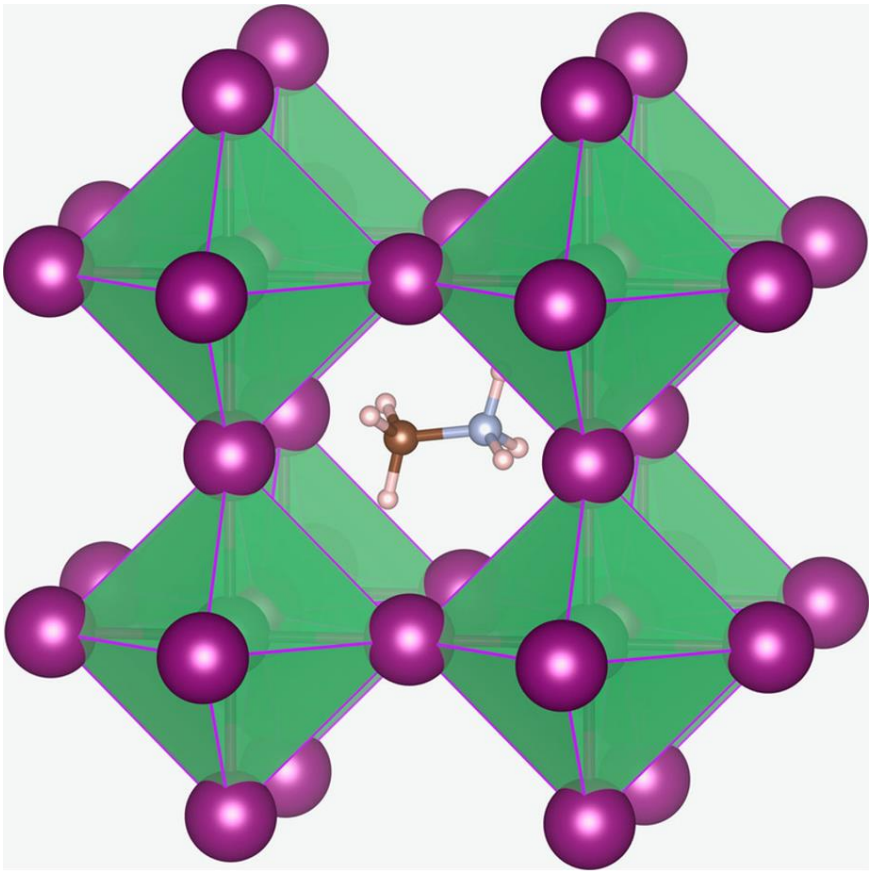

$CH_3NH_3PbX_3$

1.1 Motivation

1.1.1 Energy Crisis

The world has become more technologically and economically progressed, due to that a more energy being consumed. The human population requires more energy than ever before to propel civilization forward into the future. People in the 21st century have to figure out how to meet a growing need for energy while also keeping it safe for the environment. For example, in 2018, the U.S. Energy Information Administration (EIA) anticipated that about 80% of all energy came from fossil fuels, including 36% from petroleum, 13% from coal, and 30% from natural gas, which are all types of fossil fuel.[1] Oil may be depleted in 40 years, a better estimate of the amount of natural gas that can last 60 years and coal's supply for 150 years. Furthermore, the combustion of these fossil fuels releases greenhouse gases into the atmosphere such as carbon dioxide (CO_2), which are the main reasons for global warming and climate changes **(Figure. 1**). The greenhouse gases trap the energy and increased the earth temperature. This is making polar ice in the north and south poles melt. There are many countries at or below the sea level, which make them at risk because the sea level is rising.[2]

Figure 1. Greenhouse gases emission in the atmosphere.[2]

The rising demand, environmental concerns and higher prices of fossil fuels directed the government to search for alternative environmentally, friendly and low carbon energy source.[3] The nuclear energy accounts for 11% of world electricity generation.[4] However, the nuclear energy industry has faced numerous challenges in disposing of radioactive waste. Additionally, other severe

nuclear and radiation disasters have happened throughout history, including the three Mile Island accident (1979), the Chernobyl disaster (1986), and the Fukushima disaster, which occurred in March 2011 in Japan as a result of an earthquake and tsunami. Due to theses drawbacks many countries like Germany, Switzerland suspends and reconsider using nuclear energy. [5] Governments throughout the world have been working on rules and policies to promote environmentally friendly renewable energy generation, as well as conservation innovations in both strategy and technology. It is necessary to come up with energy policies that are beneficial to the environment and for people who use them. Renewable energy sources have a lot of benefits, including low environmental effect, little or no CO_2 and other damaging gas emissions into the atmosphere, natural resource with no external dependence, and a great complement to traditional energy sources. Growing use of renewable energy sources could result in a much more sustainable economy.

1.1.2 Renewable energy sources

Renewable energy is also called "green energy" because it comes from a source that will never run out and is also good for the environment, which makes it both renewable and green. A clean and natural source of energy with no adverse effect on the earth's climate can be produced from renewable sources such as solar power, wind, rain, tidal currents, waves, biomass and geothermal heat. Renewable energy resources, in compared to other energy sources, are widely distributed over the globe. As a result, the growth of renewable energy can address many of today's main issues, including the energy crisis, climate change, and economic calamity. The renewable energy sources such as solar hydropower, wind, biomass, tidal and geothermal energies are expected to play a vital role in moving the world to more secure reliable and sustainable energy system. [6] Biomass, hydropower, wind, solar and geothermal energy represent 13% of global energy consumption.[1]

In order to be cost competitive with energy derived from conventional sources, renewable energies must be priced competitively. In this regard, each renewable energy source has its own set of constraints. Hydropower, for example, is significantly less expensive to produce electricity, but it has a number of drawbacks, including the location of the plant, its dependence on rainfall, the expense

of energy transmission, and the environmental impact of flooding a broad region. The other renewable sources of energy, such as geothermal, wave, and biomass, are extremely inefficient and heavily dependent on nature, making them unsuitable for use in practical situations. As a result, wind and solar energy are the only viable alternatives to fossil fuels and the sole hope for satisfying future energy needs. These sources, however, have certain drawbacks, including a high cost of manufacture and a reliance on nature, such as wind and sun light. Because of this reliance, the power grid, which incorporates a significant amount of wind and solar power, will need to develop a storage system or a highly efficient technique of energy re-distribution among various remote areas. Despite these restrictions, due to their abundant source materials, wind and sun are considered the sole future green energy sources. Among many renewable energy sources, solar power is most succeeded candidate, because of the high energy, which supplied to the earth and its abundance. The sun can supply the earth with heat and light which can touch a lot of applications in our life. [7] The sun supplies energy to us with 3×10^{24} Joules/year, which is about 10,000 time more than what mankind consumes currently, if only 0.1% of this energy can converted to electricity with efficiency 10% it would be four times the world total generation capacity.[8] As a result, the efficient harnessing of solar light has the potential to solve the majority of the world's urgent energy challenges. The sun, according to a theoretical calculation, will continue to shine for more than six billion years. Using exclusively solar energy as a source of energy, the world's energy needs can be fulfilled without causing any harm to humans or releasing any greenhouse gases into the atmosphere. As a result, solar energy is the only potentially renewable source that can meet present and future energy demand. To address their energy needs, most developing countries are turning to solar cells or photovoltaic technologies. The advantages of photovoltaics (PV) include that PV need little maintenance, off-grid operation and silence which are ideal for usage in remote sites or mobile applications. As result, solar power PV technology has received considerable attention as a potentially more secure sustainable energy source and is the fastest growing generation technology, the sector has been growing with annual rate of about 40 % for the past two decades.[1]

1.1.3 The History of Solar Cells

The solar cells devices are based on photoelectric effect, which was first observed and discovered in 1839 by the young physicist Edmond Becquerel. Then the phenomenon was fully understood by Albert Einstein in 1905. The scientist William Grylls Adam, in 1876 discovered that Selenium can generate electricity when illuminated by sunlight. Then, in 1883 the US inventor Charles Fritts make the first solar cell based on coating selenium with a thin layer of gold, this solar cell gives a power conversion efficiency (PCE) of 1-2%. By the 1950s, a PCE of 6% was obtained when silicon was introduced in solar cells instead if selenium in Bell laboratories. By 1956, the first solar cells were commercially available. However, due to the expensive and complicated fabrication process of photovoltaic devices they didn't commercialized. Space program research in the 1960s established the fundamental mechanism of photovoltaic, which dramatically enhanced performance and cost effectiveness Energy prices began to rise later, which made the researcher look into photovoltaic technology as an alternative source of fossil fuel. [9,10] There has been a steady rise in solar efficiency and government support since the beginning of the 21st century. Using the solar energy has exploded in the last decade and becoming a nationwide phenomenon, a credible and reliable energy source (**Figure 2**).

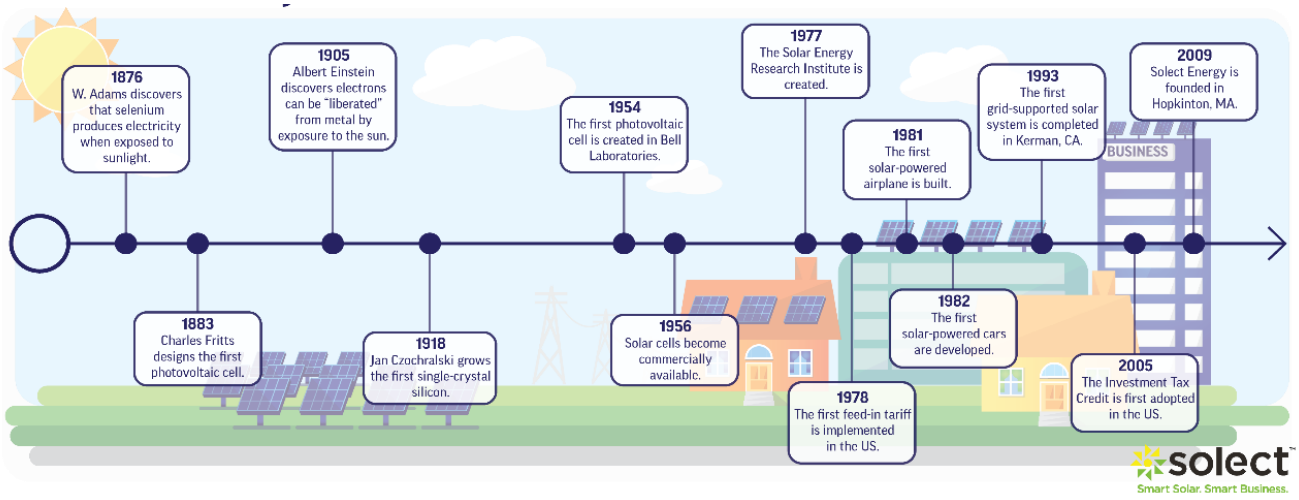

Figure 2. The history of solar cells. [10]

1.1.4 Solar Cells Generations

The solar cells can be classified into three generations (first, second and third) as illustrated in **Figure 3**. The first-generation solar cells are based on silicon wafer such as monocrystalline, polycrystalline and amorphous silicon solar cell. Although this generation of solar cells has highest cost of fabrication, it is still the dominant in the market till now due to the higher efficiency. The second-generation solar cells based on cheaper thin films such cadmium telluride and copper indium selenide/sulfide solar cells can reach relatively high PCE. However, this type of solar cells is are still expensive, because it based on sophisticated fabrication technology. The third-generation of solar cells is based on more cheaper components, easy and low-cost fabrication techniques and promising PCE. Organic photovoltaics, dye-sensitized solar cells (DSSC), quantum dot solar cells, and perovskite solar cells (PSCs) are all examples of third-generation solar cells. Within a very short period of time, PSCs demonstrate a rapid improvement in PCE and become a competitor to the market's existing silicon solar cells. Some critical limitations, such as toxicity of Pb, stability and reproducibility, have been found despite increased PCE of PSCs. In accord to the latest development of PSCs, the aims of the aim of this thesis are to investigate the effect of different types of Lewis base additives on the crystallinity, carrier recombination, and the photovoltaic performance of the fabricated PSCs. The reported efficiencies of different solar cells generations from 1975 till now are shown in **Figure 4**.

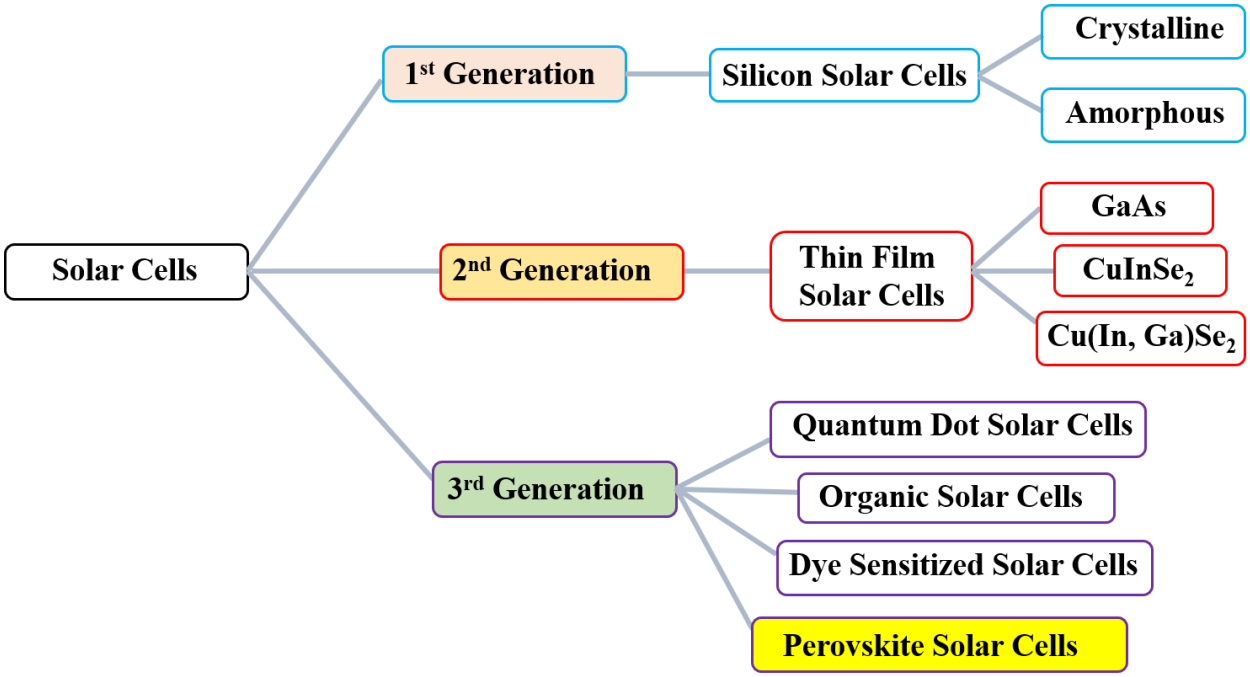

Figure 3. Different generations of solar cells

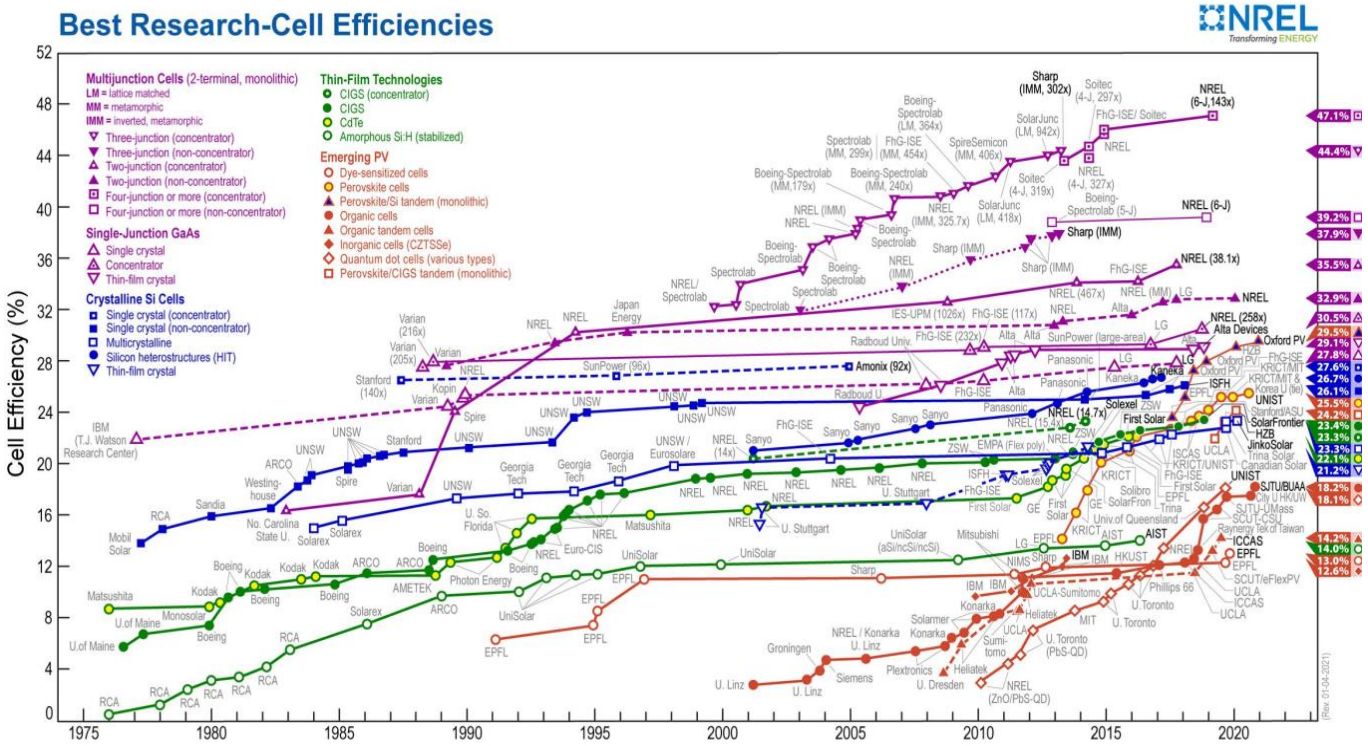

Figure 4. Maximum certified efficiencies of solar cells generations. [11]

1.2 Organic-Inorganic Hybrid Perovskites Solar Cells

1.2.1 Properties of perovskite materials

The perovskite material was first introduced as a sensitizer in DSSC by Prof. Miyasaka in 2009.[12] The $CH_3NH_3PbX_3$ perovskite material was used an absorbing layer on top of mesoporous TiO_2 in DSSC, which gives a PCE of 3.8%. However, the liquid electrolyte degraded the $CH_3NH_3PbX_3$ perovskite, which deteriorate the PCE rapidly. To solve this problem Prof. Park's group used a solid-state hole transport layer (HTL, spiro-MeOTAD) instead of the electrolyte and they obtained the PCE of 9.7%. [13] Then the researchers focused their work in PSCs with different structures, composition and preparation conditions, which lead to rocketing the PCE of PSCs to 25.5% in very short period. This remarkable achievements in the PCE of PSCs is coming from the interesting properties of these materials for photovoltaic applications. In the next part perovskite materials properties will be discussed in more details.

1.2.1.1 Suitable structure

The crystal structure of organic-inorganic perovskite is generally expressed by ABX_3 formula as shown in **Figure 5**. Here the $[BX_6]$ octahedrons share their corner in three-dimensional space. In this structure the A site is monovalent organic or inorganic cation ($CH_3NH_3^+$ $NH_2CHNH_2^+$ or Cs^+), B is the divalent metal cation (Pb^{2+} or Sn^{2+}) and X is the halogen anion (Cl^-, Br^- or I^-).

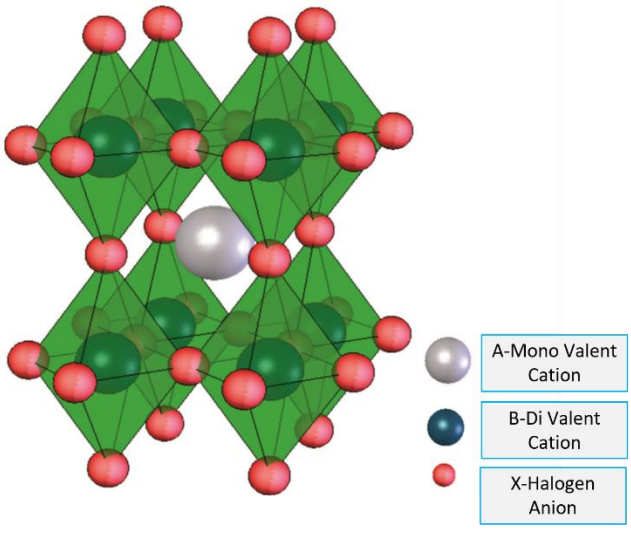

Figure 5. The crystal structure of perovskite material. [14]

Theoretical analysis shows that for obtaining a stable perovskite structure two factors must be taken into consideration, the tolerance factor (t) and the octahedral factor (μ). Equations 1 and 2 show how the tolerance factor and octahedral factor can be calculated.

$$\text{Tolerance factor, t} \frac{(rA + rX)}{\sqrt{2}\,(rM + rX)} \quad (1)$$

$$\text{Octahedral factor, } \mu = \frac{rM}{rX} \quad (2)$$

Where rA, rM, and rX are the ionic radii of the monovalent cation, divalent metal, and halide anion, respectively, on the perovskite formula ABX_3.

To form a stable perovskite structure, the tolerance factor must lie between $0.81 < t < 1.11$ and the octahedral factor (μ) must lie between $0.44 < \mu < 0.9$). By applying the ionic radii values of the Sn^{2+} and Pb^{2+} given in **Table 1** in the equations (1) and (2), we can observe that Sn^{2+} and Pb^{2+} can form more stable perovskite structures compared to Ge^{2+} due to the bigger ionic radii of Pb^{2+} and Sn^{2+}. [10] Additionally, the ionic radii of Sn^{2+} (118 pm) is close to those of Pb^{2+} (119 pm), indicating similar stability for Sn perovskite and Pb perovskite compounds according to these two factors. [16] Interestingly, the ionic radii of Sn^{2+} and Pb^{2+} (118 and 119 pm, respectively) are much bigger than those of Sn^{4+} and Pb^{4+} (69 and 78 pm, respectively), which means by considering the MA^+ cation and I^-, the Sn^{2+} and Sn^{4+} will have t of 0.924 and 1.1, and μ 0.573 and 0.335, respectively. [17-19] Based on t and μ values, the Sn^{2+} and Pb^{2+} can form more stable perovskite compared to Sn^{4+} and Pb^{4+}.

Table 1. The ionic radii of Ge, Sn, and Pb in group 14 elements.

Elements	Ionic radii [pm]	
	M^{2+}	M^{4+}
Ge	73	53
Sn	118	69
Pb	119	78

The group IV of elements of Periodic table (Pb, Sn, and Ge) have the potential to form stable perovskite structure because their first and second ionization energies are comparable to those of the group II elements (Ca, Mg) in addition to bivalent Fe, Mn, and Co, which are known to form stable

bivalent compounds, as shown in **Table 2**.[15]

Table 2. Ionization potentials of Ge, Sn and Pb in group 14 elements compared to bi-valent metals Mg, Ca, Mn, Fe and Co.

Ionization potentials [eV] / Elements	1st	2nd	3rd	4th
Ge	7.899	15.934	34.22	45.71
Sn	7.344	14.632	30.502	40.734
Pb	7.416	15.032	31.937	42.32
Mg	7.464	15.035	-	-
Ca	6.113	11.871	-	-
Mn	7.435	15.640	-	-
Fe	7.87	16.18	-	-
Co	7.86	17.06	-	-

1.2.1.2 High Absorption Coefficient

The absorption coefficient of perovskite materials is often very high. The absorption coefficient of the $CH_3NH_3PbI_3$ ($MAPbI_3$) is, for example, 10^4~10^5 cm^{-1} in the wavelength range smaller than 600 nm. The optical absorption coefficient of $MAPbI_3$ is higher than or at least comparable to that of conventional semiconductors, such as GaAs, CdTe, $Cu(In,Ga)Se_2$ (CIGS). [20] **Figure 6** illustrates the effective absorption coefficient of $CH_3NH_3PbI_3$ thin film in comparison with other materials. It is found that above the bandgap (1.57 eV), perovskite has comparable to or higher absorption coefficient than other materials. [21] This large absorption coefficient help the perovskite materials to absorb the incident light efficiently with thin layer. The thinner films will have a less defects and lower charge recombination which is very important for obtaining a high photovoltaic performance. [22, 23] If the thickness of the absorber is higher than diffusion length, this will lead to recombination of the generated carriers before reaching to the electron transport layer (ETL) or HTL.

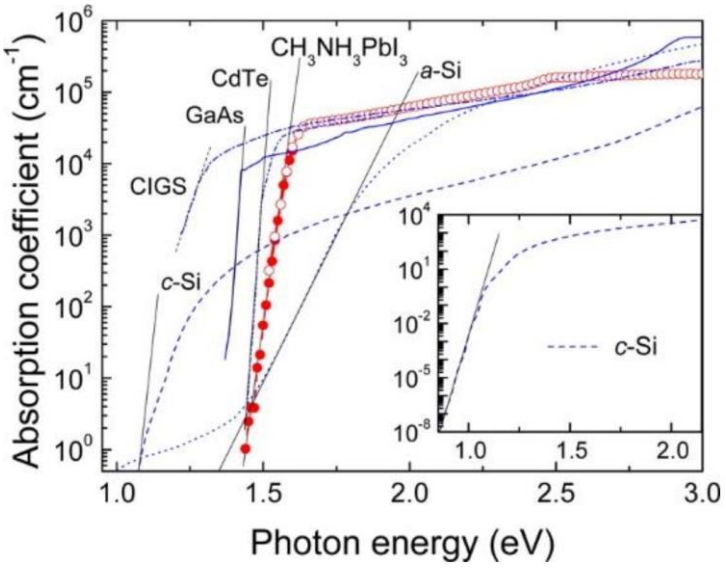

Figure 6. Optical absorption coefficient of the perovskite material $MAPbI_3$ in comparison with other materials. [21]

1.2.1.3 Low Exciton Binding Energy

In a semiconductor, the absorption of a photon with an energy higher or equal to the energy of the bandgap can lead to the formation of a quasiparticle which is known as an exciton. The photo-created electron–hole pair is bound by the attractive Coulomb interaction. This interaction is weak in perovskite material, which make the excitons to move free in the crystal. For example, the exciton binding energy of $CH_3NH_3PbI_3$ is 5-29 meV (at room temperature) and 15-34 meV (at low temperature). [24] Lower exciton binding energy is needed to reduce energy loss.

1.2.1.4 Long Charge Carrier Diffusion Length

The diffusion length, L_D, of electrons or holes in a semiconductor is defined by the average distance the relevant charge moves in the semiconductor. Long electron-hole diffusion lengths are a very critical factor in achieving the high photovoltaics performance. Because the longer diffusion length indicates that the charge carriers can move through the film without recombination. [25] Organic-inorganic perovskites exhibit significantly longer carrier diffusion lengths (500 nm–8000 nm) than organic semiconductors (~10nm). [26] For photovoltaic application, the carrier diffusion length is one of the most important parameters for efficient charge transportation. The diffusion length is related with charge carrier lifetime (τ) and mobility (μ) according to the following equation

(equation3):

$$L_D = \sqrt{K_B T \mu \tau}/\mathrm{e} \qquad (3)$$

Where, K_B, T and e are the Boltzman constant, temperature and elementary charge, respectively. All of these parameters depend on the crystallinity, morphology, and type of defects of perovskite materials.

1.2.1.5 Ambipolar Charge Transport

Most of semiconductors possess unbalanced trasport properties between electrons and holes with different effective masses of electrons and holes m_e* and m_h*. On another hand, the perovskite is well known for its ambipolar charge transport properties in which they can transport both electron and hole in a balance way. The first principal calculations show that effective mass of electron and hole in perovskite is nearly similar (m_e* = 0.23 m_0 and m_h* = 0.29m_0) which balance ambipolar charge transportation. [27] The ambipolar charge transport is critical factor for the photovoltaic performance, because it affects the charge transportation and collection properties. Consequently, it can affect the V_{OC}, short-circuits current (J_{SC}) and file factor (FF) of the PSCs.

1.2.2 Components and Device structure

The PSCs structure was generated from DSSC structure, where the PSCs structure is based on a perovskite layer as a light absorbing layer sandwiched between ETL and HTL to generate the electrons and holes. The structure of PSCs can be in three forms based on the used ETL and HTL layer (Mesoporous, Planar and Inverted Planar Structure). The structure arrangement is critical to the photovoltaic performance of PSCs, because it affects the charge transportation and recombination dynamics. [28]

1.2.2.1 Mesoporous structure

This structure as shown in **Figure 7** is composed of a fluorine doped tin oxide (FTO) glass, ETL, perovskite layer, HTL, and metal electrodes. The used ETL is usually TiO_2, SnO_2, and ZnO, while spiro-MeOTAD ([2,2',7,7'- Tetrakis(N,N-di-p-methoxyphenylamino)-9,9'-spirobifluorene] is

widely used for the HTL. The metal electrode may be Au, Ag or composition of both. Usually, the mesoporous structure contains compact layer followed by a mesoporous layer. The compact layer is usually deposited on FTO layer to extracts electrons and block holes. The mesoporous layer can be deposited on top of the compact layer by different methods such as spin coating, screen printing, magnetron sputtering, or electrospinning. [29] The structure and thickness of the mesoporous layer play acritical role on the device performance and decreasing the hysteresis. [29] Decreasing the thickness of the mp-TiO_2 layer can help the pore-filling process and thus result in improved efficiency. [30]

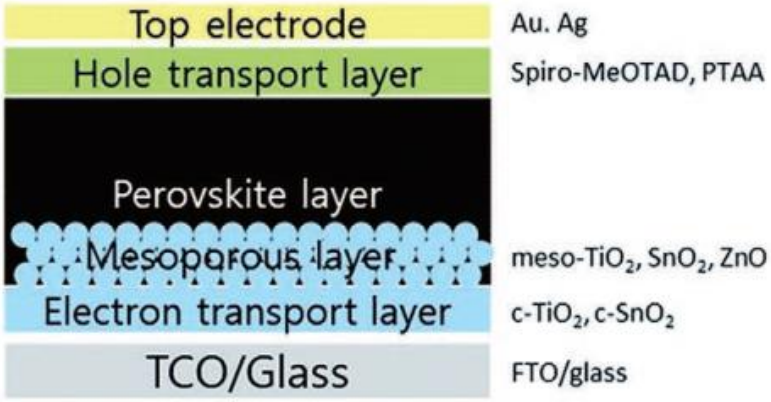

Figure 7. Mesoporous structure of perovskite solar cells. [29]

1.2.2.2 Planar structure (n–i–p)

This structure of PSCs is widely used in PSCs fabrication because it is composed of only compact layer without the mesoporous materials, which make it easier in fabrication and lower in cost without need for high temperature process (**Figure 8**). [31, 32] The planar architecture is industrially more preferable and more compatible with flexible and tandem applications. [33-35] Many successful ETLs were utilized in this structure such as (TiO_2, SnO_2 and ZnO), while for HTL the spiro-MeOTAD and PTAA are widely used.

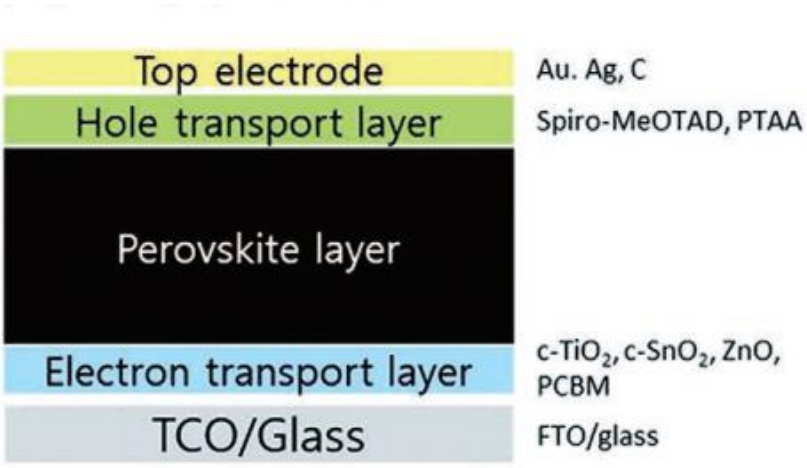

Figure 8. Planar structure (n–i–p) of perovskite solar cells. [29]

1.2.2.3 Inverted Planar structure (p–i–n)

This structure has the ETL and HTL in opposite positions to those of the normal planar type structure (**Figure 9**). [36, 37] The PSCs based on inverted structure possess many advantages such as easy fabrication process, negligible hysteresis, and high stability. [38] In this structure, [6,6]-phenyl C_{61}-butyric acid methyl ester (PCBM) and fullerene (C_{60}) are widely used for the ETL. While for HTL, and poly(3,4-ethylenedioxythiophene) poly(styrene-sulfonate) (PEDOT: PSS) and NiO are used.

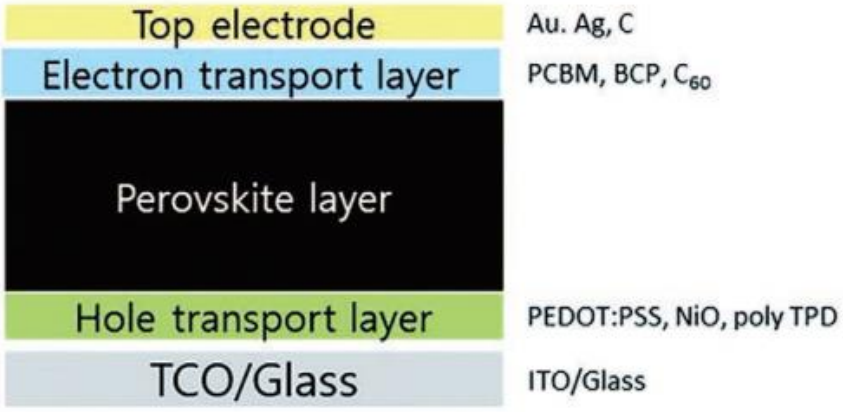

Figure 9. Inverted Planar structure (p–i–n) of perovskite solar cells. [29]

Device architectures of PSCs with only one charge transport layer, such as ETL-free or HTM-free, have been reported because perovskites were found to be an ambipolar semiconductor. [39-42] The chemical structure of used HTL and ETL in PSCs are given in **Figure 10**.

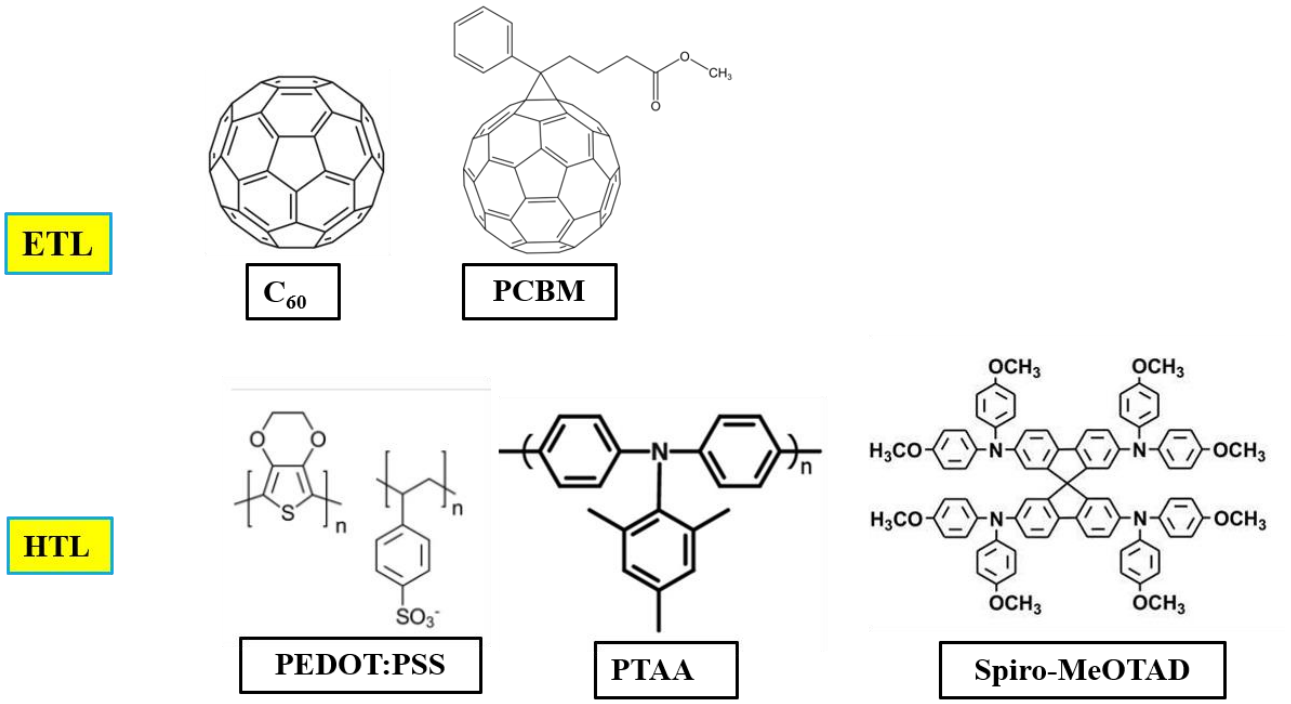

Figure 10. The chemical structures of used ETL and HTL layers in PSCs fabrication

1.2.3 Working Principles

The working principles of PSCs is based on three steps, light absorption, carrier separation and carrier transportation (**Figure 11**). When the light hit the perovskite materials, the perovskite dissociates to free electrons and holes due to the low binding energy (5-29 meV). This is because the perovskite has a high charge mobility and a long diffusion length. This makes it easy for electrons and holes to move across the perovskite. Thus, electrons move through the perovskite to the ETL, where they are collected by the electrode. The photogenerated holes move through the perovskite and are collected by the electrode. The selection of ETL and HTL with matched energy levels with conduction band (CB) and valence band (VB) of the perovskite is very important to guarantee efficient carrier transportation. The VB of the HTL should be higher than the VB of the perovskite layer to afford smoothly transportation of holes from the perovskite layer to the HTL. Whereas, in same time the CB of the ETL should be lower than the CB of perovskite for better electron transportation. This charge selectivity property is essential for the device performance because if an electron reach to wrong electrode, it will recombine non-radiatively with one of many holes present there. This process leads the unwanted loss of photogenerated charges. [43, 44]

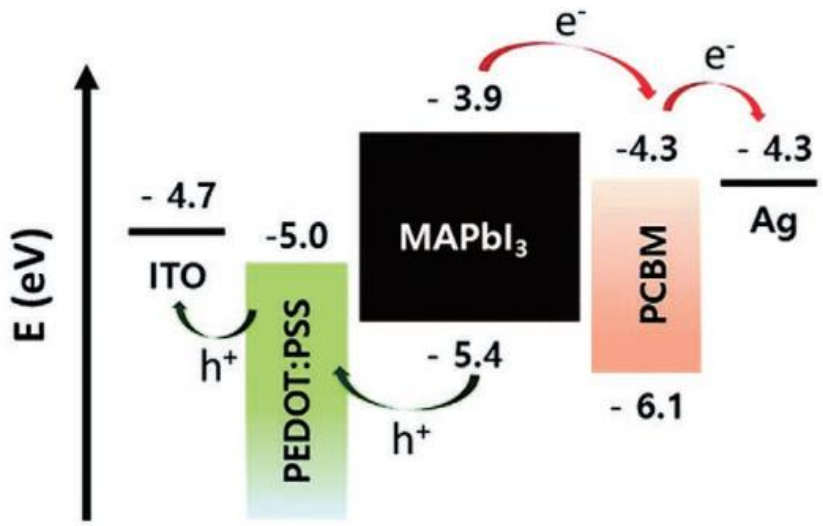

Figure 11. The working principles of perovskite solar cells. [29]

1.2.4 Fast Interaction of Perovskite precursor

The reaction rate between the divalent halide and the cation halide occurred very fast and even faster in Sn than Pb analogues as illustrated in equation 4. [45, 46]

$$AX + BX_2 \rightarrow ABX_3 \qquad (4)$$

Where **A** is the monovalent cation (CH_3NH_3, $CHNHNH_2$,..), **B** is the divalent cation (Sn^{2+}, Pb^{2+},..), X is the halide (I^-, Cl^-,…)

Consequently, the perovskite film fabrication needs more control to obtain high-quality perovskite films. The quick crystallization process in the precursor solutions of the perovskite has a significant effect on the perovskite film quality, which eventually leads to poor film coverage, with the presence of many pinholes. [47-50] Usually, the pinholes are generated on the surface of perovskite from the unbalanced rates of nucleation and crystal growth. [51,52] Based on the strong ability of Sn^{2+}/Pb^{2+} to act as a Lewis acid, the addition of numerous Lewis bases in the precursor solution of the perovskites, can act as morphology controller, agents to reduce the oxidation of Sn^{2+} to Sn^{4+} and/or passivate the undercoordinated Sn^{2+}/Pb^{2+} defects to get a highly crystalline perovskite layer with fewer pinholes. [53,54]

1.2.5 Carrier Recombination

The PSCs reached certified PCE above 25% due to the outstanding properties of perovskite materials such as tunable bandgap, long diffusion length, high absorption coefficient and carrier mobility. However, many types of defects generated due to the ionic properties of these materials, which effect on the PCE, stability and reproducibility. [55] Furthermore, due to the solution precursor compositions and quick processing conditions, enormous amounts of defects of various types are generated within perovskite absorbers or on their surfaces, which act as nonradiative recombination centers. [56] The polycrystalline perovskite films possess approximately five times defects density higher than single crystal perovskite and conventional crystalline silicon. [57] The defects in perovskites are charged (e.g., a halide ion vacancy leading to undercoordinated Pb^{2+}). The halide vacancies (e.g., Cl^-, Br^-, I^-) leading to exposure of under-coordinated positively charged Pb^{2+} atoms. [58] The surface under-coordinated Pb^{2+} is the main source of trap states and several chemicals have been proposed to heal this particular type of defect. It is critical for the photogenerated carriers to exhibit long lifetimes for collection by electrodes before non-radiative recombination. This non-radiative recombination will not only deteriorate photovoltaic properties, but also accelerate device degradation. The effective suppression of the defects will diminish the non-radiative recombination, which can improve the PSCs performance and stability. The low thermal stability of perovskite materials lead to formation of undercoordinated Pb^{2+} defects, which resulted from evaporation of iodide ions as explained by **Figure 12** and the following equation (equation 5):

$$I^0 \rightarrow V^+ + I^- \qquad (5)$$

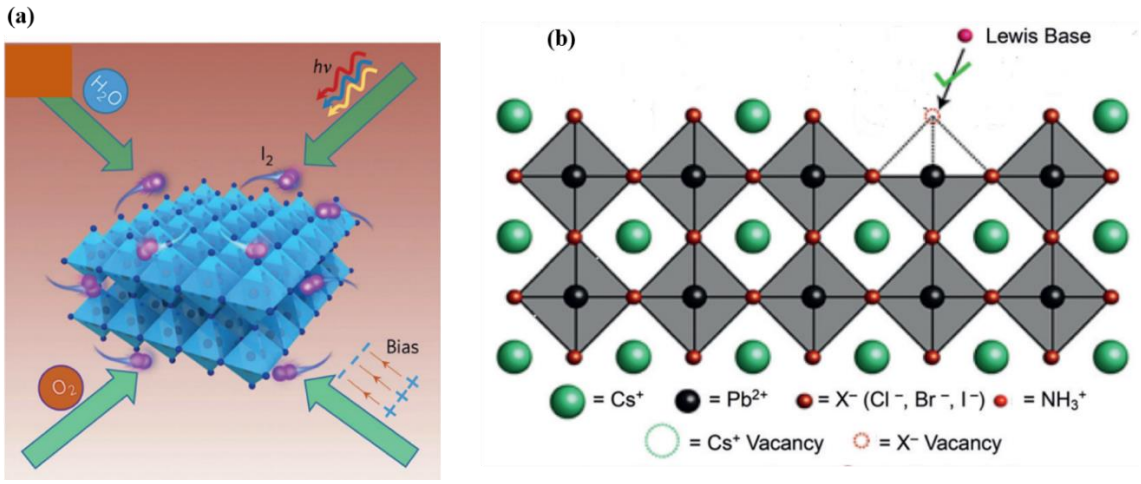

Figure 12. Graphical illustration of (a) Formation of defects in perovskite solar cells and (b) Suppression the defects using Lewis base additives. [58]

Where I^0 is iodide atom occupying its perfect site, V^+ the positively charged I vacancy defect and I^- the evaporated from perovskite lattice. Surface and grain boundary defects in perovskite films act as severe non-radiative recombination sites, reducing photovoltaic performance.

1.2.6 Toxicity

PSCs have undergone rapid progress during the last decade and reached the PCE over 25%. [58] Despite the impressive progress in Pb-based PSCs by reaching a PCE over 25%, their commercialization facing several challenges related to presence of toxic lead element and stability upon prolonged exposure to light, humidity, and high temperature. In 2011, the European Union released the ‘‘Directive on the restriction of the use of certain hazardous substances in electrical and electronic equipment (RoHS)’’, which restricts the maximum concentration of lead in any electronic devices to 0.1% in weight. [59] However, almost all the high-performance perovskites contain more than 10% lead in weight. The stabilized 2+ state of Pb^{2+} can result in the replacement of Ca^{2+} or Zn^{2+} in protein and thus causes cytotoxicity, while the moderately water-soluble carcinogen PbI_2 can be formed from thermal/moisture/polar solvent-induced degradation of the unstable perovskite materials. [60] The easy solubility of perovskite bears the risk of leakage into the environment and possess critical impact on environment and nature (see **Figure 13a**). The Pb-based perovskite material can interact easily with water or humidity and form water soluble compounds, which can step by step

accumulate with food and human body as explained in **Figure 13b**. [61] These potential environmental drawbacks hinder the commercialization of Pb-PSCs and encouraged the PSC community to replace Pb with less toxic alternative materials. On other hand, Sn is located above Pb in the periodic table, which is known to be safe metal and its known natural biological role in living organisms and its not easily absorbed by animals and humans. The low toxicity is relevant to the widespread use of tin in dinnerware and canned food. Furthermore, the Sn^{2+} halides can easily oxidize into the inactive and water-insoluble SnO_2 in air,

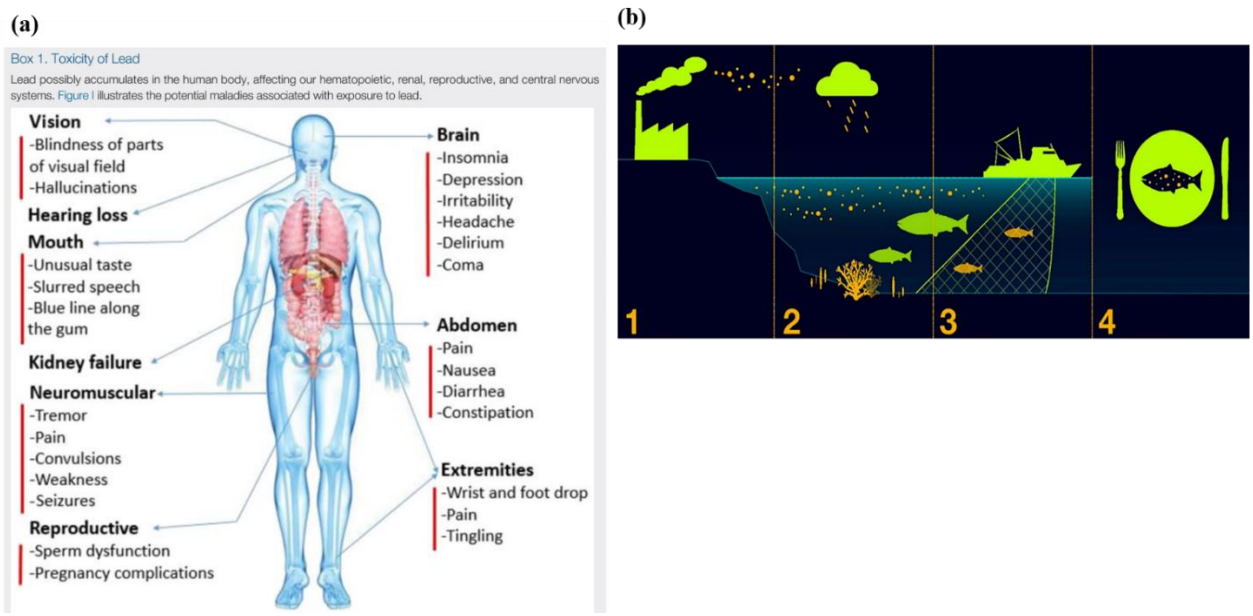

Figure 13. (a) The Pb toxicity in the human body. [60] (b) Risk of Pb-based PSCs for food chain. [61]

1.3 Lewis Base Additives

The elements Sn and Pb are found in the middle of the periodic table and have a high ability to form stable and fairly strong bonds with the bulk of other elements. They also have a wide range of coordination geometries. [15, 62a] Because of the high negative enthalpy of formation, the compounds of Pb^{2+} and Sn^{2+} are regarded thermodynamically stable. The enthalpy of formation tends to become more negative with decreasing size or increasing electronegativity. Based on their electrochemical potential, the oxidation state of Sn^{4+} is more stable than that of Sn^{2+}. However, the electrochemical energy difference between the two oxidation states is negligible. In case of Pb^{2+} it is more stable than Sn^{2+} as indicated by equation (6,7):

$$Sn^{2+} \rightarrow Sn^{4+} + 2e^- \qquad E^0 = -0.15\ V \qquad (6)$$

$$Pb^{2+} \rightarrow Pb^{4+} + 2e^- \qquad E^0 = -1.67\ V \qquad (7)$$

The electronic configuration of Sn^{50} ([Kr] $4d^{10}$ $5s^2$ $5p^2$) and Pb^{82} ([Xe] $6s^2$ $4f^{14}$ $5d^{10}$ $6p^2$) indicates the presence of four electrons on the last level distributed on orbitals *s* and *p*. The bonding structure of metal halides is shown in **Figure 14a**, which shows the presence of two nonbonding electrons located in the 5*s* orbital. The metal halides use the two electrons on the *p*-orbital to form the covalent bond with X, while the 5*s* two unshared electrons not included in the bonding structure. [62a] The remaining vacant *p* orbital in Sn^{2+} and Pb^{2+} is working as electron acceptor. Consequently, they are π-acceptors (strong Lewis acids) due to their tendency to accept two electrons to complete the octet structure and stabilize themselves, as shown in **Figure 14b**. [62a]

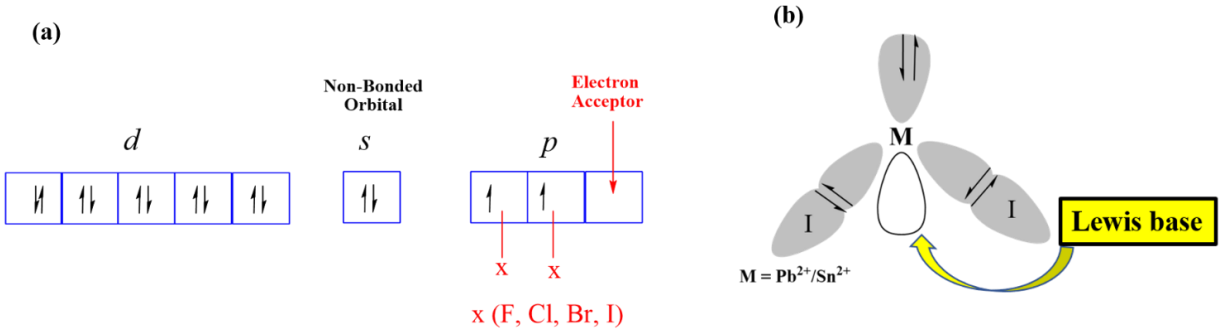

Figure 14. (a) The bonding structure of metal halide. (b) The interaction of Lewis base additives with the vacant orbital of the metal halides. [62a]

The halides of group IV elements increase in stability in the following sequence $CX_2 < SiX_2 < GeX_2 < SnX_2 < PbX_2$. The Sn^{2+} and Pb^{2+} halides can interact with Lewis base additives to form adducts, which is a useful property that may assist the crystallinity and control the film formation of perovskite films. The Lewis acidity of Sn^{2+} halides is stronger than the Pb^{2+} analogous, which means that the interaction between perovskite precursor is stronger and faster in case of Sn-based perovskites.

1.4 Perovskite Solar Cells Characterization

The perovskite solar cell is behaved like a diode in dark condition (**Figure 15a**) but when illuminated its current increased by an order of magnitude which is due to the photogenerated current (**Figure 15b**).

1.4.1 Current Density-Voltage Characterization

For solar cell, current density-voltage (*J-V*) curves are the most important and direct characterization method for performance of solar cells. To do this, usually several potentials is applied (from negative value to positive value) and measure the corresponding current. To determine the performance of solar cell, three parameters J_{SC}, V_{OC} and FF (**Figure 15c**) are needed which can be defined by the following equations (7-9):

$$\text{Power conversion efficiency (PCE)} = \eta = \frac{P_{\text{out}}}{P_{\text{in}}} X100 = 100 = \frac{J_{MAX}V_{MAX}}{P_{\text{in}}} X100 \quad (7)$$

$$FF = \frac{J_{MAX}V_{MAX}}{J_{SC}V_{OC}} \quad (8)$$

$$PCE = \frac{J_{SC}V_{OC}FF}{J_{SC}V_{OC}} X100 \quad (9)$$

Where P_{in}100 mW cm^{-2}.

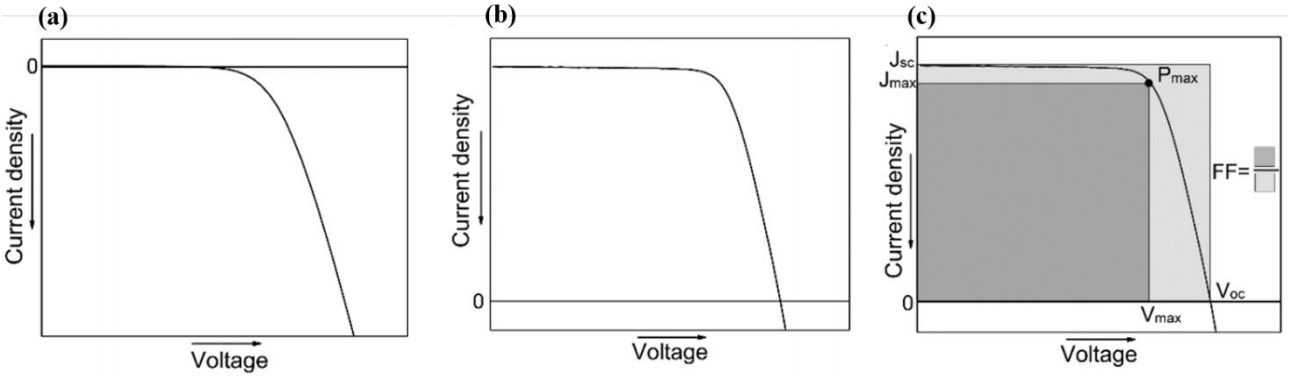

Figure 15. (a) *J-V* curves of PSCs measured under dark and (b) illumination conditions. (c) *J-V* curves measured under illumination and the corresponding performance parameters. [62b]

The J_{SC} indicates the maximum current density of the device, which is determined by the incident light-harvesting efficiency (LHE), charge injection, and charge collection at the interfaces. The V_{OC} is determined by differences between Fermi levels of the ETL and the HTL. The FF expressed as a ratio of the maximum obtained power to the product of the J_{SC} and V_{OC} is determined by the series resistance (Rs) and the shunt resistance (Rsh). The Rs is influenced by the resistance of the functional layer such as the absorber, ETL, HTL, electrode, and the conductive glass. The Rsh is influenced by recombination processes at the interfacial defects in the functional layers, for example,

a HTL deposited on the perovskite layer penetrated and attached directly to ETL. The generated excitons are recombined at the interface between the ETL and the HTL.

1.4.2 Incident Photon-to-Current Conversion Efficiency

The IPCE, called as external quantum efficiency (EQE), is one of the common measurements for determining the EQE of incident photons converted to currents to the external circuit at each wavelength of monochromatic light (**Figure 16**). The IPCE measurement is used to calculate the generated J_{SC} by irradiating monochromatic light. The IPCE is expressed by the equation 10:

$$\text{IPCE}\ (\lambda) = EQE(\lambda) = \frac{\text{electrons}\ /\text{cm}^2/\text{s}}{\text{photons}\ /\text{cm}^2/\text{s}} = \frac{j_{ph}\left(\frac{mA}{\text{cm}^2}\right) X 1239.8(\text{VXnm})}{P_{\text{mono}}\left(\frac{mW}{\text{cm}^2}\right) \times \lambda(\text{nm})} \quad (10)$$

Where, 1239.8V X nm is the product of plank's constant and speed of light (c), P_{mono} is the illuminated power intensity in mW/cm^2 and is the wavelength at which illumination power is measured. So, the integration of IPCE over the measured wavelength will give the J_{SC} of solar cell.

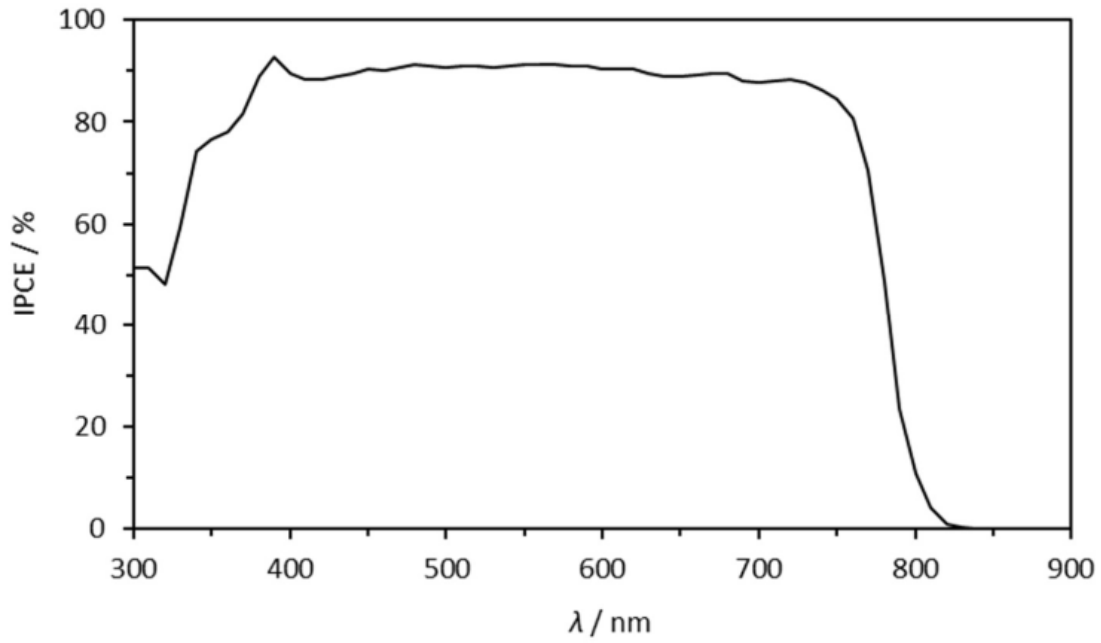

Figure 16. The IPCE spectra of fabricated PSCs with the configuration of FTO/TiO_2/$MAPbI_3$/spiroOMeTAD/Au. [62c]

1.4.3 Photoluminescence and Time-Resolved Photoluminescence

To analyses the carrier dynamics of the perovskite layer and carrier quenching of the defects in the perovskite polycrystalline film, photoluminescence (PL) is performed, which excitation

wavelength is ~420 nm, and the device configuration of glass substrate/perovskite. From the combination of PL and time resolved photoluminescence (TRPL) measurements, the detailed carrier dynamics can be provided.

1.4.4 Electrochemical Impedance Spectroscopy (EIS)

The impedance of the solar cells is measured at several frequencies by applying a small voltage and measuring the current in the frequency domain. By using a large range of frequencies different physical effects in the device can be distinguished due to their different transient dynamics. The size of the semi-circle in the Cole-Cole plot represents the recombination in the device, the bigger size means higher resistance to recombination.

1.4.5 Transient Photovoltage and Transient Photocurrent Decay

The transient photovoltage is measured under the open-circuit conditions, where the external current in the solar cell is zero. The voltage decay was recorded in the open circuit condition, and this decay gives information about the carrier recombination.

The transient photocurrent is measuring the short-circuit current when no light, the current decay was recorded. It gives information about carrier extraction.

1.5 Aim of This Thesis

The perovskite films fabricated based on the solution technique can easily generate trap states at the surface and grain boundaries (GBs), which act as carrier recombination centers. Furthermore, the faster interaction between perovskite precursors, affects the crystallinity and bad morphology of the resulted perovskite films. All these factors lead to diminish the photovoltaic performance and stability of the fabricated PSCs. It is crucial to control the fabrication process of the PSCs with fewer defects, better morphology, enhanced charge carrier transfer and improved stability.

The perovskite precursor can interact with the Lewis base additives by forming adducts. These formed adducts can improve the crystallinity and morphology of the perovskite film by retarding the interaction between perovskite percussor. Furthermore, because the Lewis base additives possess extra electrons, so by adding them to the perovskite materials they can suppress the generated

undercoordinated Pb^{2+} defects. To achieve these goals, the main focus of this thesis is to investigate the effect of different types of Lewis base additives using their different functional groups on the crystallinity, carrier recombination, and the resulted photovoltaic performance of the fabricated PSCs.

In the first part of chapter 3, I introduced the utilizing of two β-diketone Lewis base additives 2,4-pentanedione (acetylacetone; acac) and 3-methyl-2,4-nonanedione (R-acac) to passivate the undercoordinated Pb^{2+} defects formed on the $MAPbI_3$ perovskite film. The two β-diketone Lewis could interact with undercoordinated Pb^{2+} defects efficiently by using their bidentate carbonyl groups in their skeleton, which resulted in suppression these defects efficiently as indicated from the PL spectra. The fabricated $MAPbI_3$ perovskite films showed a better morphology and improved crystallinity. Consequently, the PSCs were fabricated using acac and R-acac to show their effect on the photovoltaic performance and the stability.

Although the Pb-PSCs have achieved a high PCE of 25.6%, which is one of the highest PCEs ever reported in solar cell generations, Pb is possibly hazardous to the ecosystem. These negative environmental consequences obstruct the commercial implementation of Pb-PSCs. Compared to Pb, the Sn metal is less toxic and can form perovskite compounds with various cations. Furthermore, Sn perovskite materials possess superior optoelectronic characteristics compared to Pb analogs, including a narrower bandgap, a lower exciton binding energy and a slightly smaller radius than Pb^{2+}. However, Sn-PSCs suffer from critical problems such as the fast interaction between the perovskite components in the precursor solution, which affects the crystallinity and morphology of the fabricated perovskite films. In addition, Sn^{2+} can be easily oxidized to Sn^{4+}, which forms Sn vacancies in the $FASnI_3$ absorber layer.

The inclusion of the Lewis base additives within the perovskite precursor could improve the quality of the fabricated Sn-PSCs. However, the problem of faster recombination of the photo-generated electron-hole pairs is still crucial and leads to performances loss in Sn-PSCs. To improve electron mobility and reduce carrier recombination in Sn-PSCs, I used the diaminomaleonitrile (DAMN) Lewis base additive as given second part of chapter 3. Based on presence of two effective

electron withdrawing cyano (CN) groups in DAMN, the electron transfer from perovskite layer to the adjacent ETL can be enhanced, which will decrease the carrier recombination. In same time, the morphology, crystallinity and the lattice strain of the pristine and modified perovskite films were investigated to understand the effect of adding DAMN Lewis base additive. Also, in this part the effect of using different concentration of DAMN Lewis base additives on PSCs performance have been showed.

In the last part of chapter 3, to reduce the oxidation of Sn^{2+} to Sn^{4+} in Sn-PSCs formamidine sulfonic acid ($FASO_2H$) Lewis base additive was added to the perovskite solution. The $FASO_2H$ Lewis base additive was chosen because it is a strong reducing agent and it comes with the sulfonic group in structure, which is hydrophobic group. The interaction between $FASO_2H$ and perovskite precursor was confirmed using FTIR. Furthermore, the improved resistance to water due to the presence of hydrophobic group $-SO_2H$ was investigated by measuring the water contact angle of $FASnI_3$ and $FASnI_3$-$FASO_2H$ perovskite films. So, this type of additives might be useful for Sn-based PSCs to simultaneously reduce the oxidation and improve the stability of Sn-PSCs. The crystallinity and morphology of the fabricated perovskite films were investigated.

1.6 References

(1) Lu, Y.; Khan, Z. A.; Alvarez-Alvarado, M. S.; Zhang, Y.; Huang, Z.; Imran, M. J. S. A critical review of sustainable energy policies for the promotion of renewable energy sources. *Sustainability*, **2020,** *12* (12), 5078.

(2) Greenhouse gases: Causes, sources and environmental effects, https://www.livescience.com/37821-greenhouse-gases.html, **2021**.

(3) Zissler, R.; Ohbayashi, M. The Rise of Renewable Energy and Fall of Nuclear Power, Competition of Low Carbon Technologies. *Renewable Energy Institute*, **2019**.

(4) U.S. Energy Information Administration. Energy information administration, Total Energy, http://www.eia.gov/totalenergy/, **2021**.

(5) World Energy Perspective: Nuclear Energy One Year After Fukushima, *World Energy Council*, **2012**.

(6) Twidell, J. *Renewable energy resources,* Routledge: **2021**.

(7) Francis, O. I.; Ikenna, A. Review of Dye-Sensitized Solar Cell (DSSCs) Development. *J. Nat. Sci.* **2021,** *13*, 496-509.

(8) Kumar, S.; Pawar, S. In THE ENERGY ASPECTS OF BIOMASS, *Biomass Energy Seminar Shivaji University, Kolhapur*, **1989**, 1-19.

(9) A Brief History of Solar Panels, *Smithsonian Magazine*, https://www.smithsonianmag.com/sponsored/brief-history-solar-panels-180972006/, **2021**.

(10) THE HISTORY OF SOLAR ENERGY, Solect energy, Avilable online: https://solect.com/history-solar-energy/, **2021**.

(11) Best Research-Cell Efficiency Chart, https://www.nrel.gov/pv/cell-efficiency.html, **2022**.

(12) Kojima, A.; Teshima, K.; Shirai, Y.; Miyasaka, T. Organometal halide perovskites as visible-light sensitizers for photovoltaic cells. *J. Am. Chem. Soc.* **2009,** *131*, 6050-6051.

(13) Kim, H.-S.; Lee, C.-R.; Im, J.-H.; Lee, K.-B.; Moehl, T.; Marchioro, A.; Moon, S.-J.; Humphry-Baker, R.; Yum, J.-H.; Moser, J.; Grätzel, M.; Park, Nam-G. Lead iodide perovskite sensitized all-solid-state submicron thin film mesoscopic solar cell with efficiency exceeding 9%. *Sci Rep.* **2012,** *2*, 1-7.

(14) Nikonov, A.; Kuterbekov, K.; Bekmyrza, K. Z.; Pavzderin, N. A brief review of conductivity and thermal expansion of perovskite-related oxides for SOFC cathode. *Eurasian Journal of Physics and Functional Materials*, **2018,** *2*, 274-292.

(15) P. J. Smith**,** Chemistry of Tin**,** *Springer Science & Business Media,London* **1998.**

(16) Xu, Q.; Yang, D.; Lv, J.; Sun, Y. Y.; Zhang, L. Perovskite solar absorbers: materials by design. *Small Methods* **2018,** *2*, 1700316.

(17) Kieslich, G.; Sun, S.; Cheetham, A. K. An extended tolerance factor approach for organic–inorganic perovskites. *Chem. Sci.* **2015,** *6*, 3430-3433.

(18) McGehee, M. D. Fast-track solar cells. *Nature* **2013**, 501, 323-325.

(19) Mitzi, D. B.; Feild, C.; Harrison, W.; Guloy, A. Conducting tin halides with a layered organic-based perovskite structure. *Nature* **1994**, 369, 467-469.

(20) Fan, Z.; Sun, K.; Wang, J. Perovskites for photovoltaics: a combined review of organic–inorganic halide perovskites and ferroelectric oxide perovskites. *J. Mater. Chem. A* **2015,** *3*, 18809-18828.

(21) The Duong, Development of High Efficiency Four-Terminal Perovskite-Silicon Tandems. *The Australian National University*, **2017**, 1001, 48106-41346.

(22) De Wolf, S.; Holovsky, J.; Moon, S.-J.; Löper, P.; Niesen, B.; Ledinsky, M.; Haug, F.-J.; Yum, J.-H.; Ballif, C. Organometallic halide perovskites: sharp optical absorption edge and its relation to photovoltaic performance. *J. Phys. Chem. Lett.* **2014,** *5*, 1035-1039.

(23) Jensen, N.; Hausner, R.; Bergmann, R.; Werner, J.; Rau, U. Optimization and characterization of amorphous/crystalline silicon heterojunction solar cells. *Prog Photovolt* **2002,** *10* (1), 1-13.

(24) Baranowski, M.; Plochocka, P. Excitons in metal‐halide perovskites. *Adv. Energy Mater.* **2020**, 10, 1903659.

(25) Zhang, F.; Yang, B.; Li, Y.; Deng, W.; He, R. Extra long electron–hole diffusion lengths in $CH_3NH_3PbI_{3-x}Cl_x$ perovskite single crystals. *J. Mater. Chem. C* **2017,** *5*, 8431-8435.

(26) Xing, G.; Mathews, N.; Sun, S.; Lim, S. S.; Lam, Y. M.; Grätzel, M.; Mhaisalkar, S.; Sum, T. C. Long-range balanced electron-and hole-transport lengths in organic-inorganic $CH_3NH_3PbI_3$. *Science* **2013,** *342*, 344-347.

(27) Giorgi, G.; Fujisawa, J.-I.; Segawa, H.; Yamashita, K. Small photocarrier effective masses featuring ambipolar transport in methylammonium lead iodide perovskite: a density functional analysis. *J. Phys. Chem. Lett.* **2013,** *4*, 4213-4216.

(28) Liu, M.; Endo, M.; Shimazaki, A.; Wakamiya, A.; Tachibana, Y. Identifying an optimum perovskite solar cell structure by kinetic analysis: planar, mesoporous based, or extremely thin absorber structure. *ACS Appl. Energy Mater.* **2018,** *1*, 3722-3732.

(29) Wang, R.; Mujahid, M.; Duan, Y.; Wang, Z. K.; Xue, J.; Yang, Y. A review of perovskites solar cell stability. *Adv. Funct. Mater.* **2019,** *29*, 1808843.

(30) Leijtens, T.; Lauber, B.; Eperon, G. E.; Stranks, S. D.; Snaith, H. The importance of perovskite pore filling in organometal mixed halide sensitized TiO_2-based solar cells. *J. Phys. Chem. Lett.* **2014,** *5*, 1096-1102.

(31) Matsui, T.; Seo, J. Y.; Saliba, M.; Zakeeruddin, S. M.; Grätzel, M. Room-Temperature Formation of Highly Crystalline Multication Perovskites for Efficient, Low-Cost Solar Cells. *Adv. Mater.* **2017,** *29*, 1606258.

(32) Jeon, N. J.; Noh, J. H.; Kim, Y. C.; Yang, W. S.; Ryu, S.; Seok, S. Solvent engineering for high-performance inorganic–organic hybrid perovskite solar cells. *Nat. Mater.* **2014,** *13*, 897-903.

(33) Park, I. J.; Kang, G.; Park, M. A.; Kim, J. S.; Seo, S. W.; Kim, D. H.; Zhu, K.; Park, T.; Kim, J. Y. Highly efficient and uniform 1 cm^2 perovskite solar cells with an electrochemically deposited NiO_x hole-extraction layer. *ChemSusChem* **2017,** *10*, 2660-2667.

(34) Shao, Y.; Yuan, Y.; Huang, J. Correlation of energy disorder and open-circuit voltage in hybrid perovskite solar cells. *Nat. Energy* **2016,** *1* (1), 1-6.

(35) Chen, W.; Wu, Y.; Yue, Y.; Liu, J.; Zhang, W.; Yang, X.; Chen, H.; Bi, E.; Ashraful, I.; Grätzel, M.; Han, H. Efficient and stable large-area perovskite solar cells with inorganic charge extraction layers. *Science* **2015**, 350, 944-948.

(36) Jeng, J. Y.; Chiang, Y. F.; Lee, M. H.; Peng, S. R.; Guo, T. F.; Chen, P.; Wen, T. C. $CH_3NH_3PbI_3$ perovskite/fullerene planar-heterojunction hybrid solar cells. *Adv. Mater.* **2013,** *25* (27), 3727-3732.

(37) Jeng, J. Y.; Chen, K. C.; Chiang, T. Y.; Lin, P. Y.; Tsai, T. D.; Chang, Y. C.; Guo, T. F.; Chen, P.; Wen, T. C.; Hsu, Y. J. Nickel oxide electrode interlayer in $CH_3NH_3PbI_3$ perovskite/PCBM planar-heterojunction hybrid solar cells. *Adv. Mater.* **2014,** *26*, 4107-4113.

(38) Crispin, X.; Jakobsson, F.; Crispin, A.; Grim, P.; Andersson, P.; Volodin, A. v.; Van Haesendonck, C.; Van der Auweraer, M.; Salaneck, W. R.; Berggren, M. The origin of the high conductivity of poly (3, 4-ethylenedioxythiophene)− poly (styrenesulfonate)(PEDOT− PSS) plastic electrodes. *Chem. Mater.* **2006,** *18* (18), 4354-4360.

(39) Etgar, L.; Gao, P.; Xue, Z.; Peng, Q.; Chandiran, A. K.; Liu, B.; Nazeeruddin, M. K.; Grätzel, M.. Mesoscopic $CH_3NH3PbI_3/TiO_2$ heterojunction solar cells. *J. Am. Chem. Soc.* **2012,** *134* (42), 17396-17399.

(40) Laban, W. A.; Etgar, L. Depleted hole conductor-free lead halide iodide heterojunction solar cells. *Energy Environ. Sci.* **2013,** *6* (11), 3249-3253.

(41) Liu, D.; Yang, J.; Kelly, T. L. Compact layer free perovskite solar cells with 13.5% efficiency. *J. Am. Chem. Soc.* **2014,** *136* (49), 17116-17122.

(42) Ke, W.; Fang, G.; Wan, J.; Tao, H.; Liu, Q.; Xiong, L.; Qin, P.; Wang, J.; Lei, H.; Yang, G.; Qin, M.; Zhao, X.; Yan, Y. Efficient hole-blocking layer-free planar halide perovskite thin-film solar cells. *Nat. Commun.* **2015,** *6*, 1-7.

(43) Tress, W.; Marinova, N.; Inganäs, O.; Nazeeruddin, M. K.; Zakeeruddin, S. M.; Graetzel, M. In The role of the hole-transport layer in perovskite solar cells-Reducing recombination and increasing absorption, *IEEE 40th Photovoltaic Specialist Conference (PVSC)* **2014**, 1563-1566.

(44) Bi, D.; Yang, L.; Boschloo, G.; Hagfeldt, A.; Johansson, E. M. Effect of different hole transport materials on recombination in $CH_3NH_3PbI_3$ perovskite-sensitized mesoscopic solar cells. *J. Phys. Chem. Lett.* **2013,** *4*, 1532-1536.

(45) Liang, K.; Mitzi, D. B.; Prikas, M. T. Synthesis and characterization of organic− inorganic perovskite thin films prepared using a versatile two-step dipping technique. *Chem. Mater.* **1998,** *10*, 403-411.

(46) Hao, F.; Stoumpos, C. C.; Chang, R. P.; Kanatzidis, M. G. Anomalous band gap behavior in mixed Sn and Pb perovskites enables broadening of absorption spectrum in solar cells. *J. Am. Chem. Soc.* **2014,** *136*, 8094-8099.

(47) Ke, W.; Stoumpos, C. C.; Kanatzidis, M. G. "Unleaded" perovskites: status quo and future prospects of tin-based perovskite solar cells. *Adv. Mater.* **2019,** *31*, 1803230.

(48) Kayesh, M. E.; Matsuishi, K.; Kaneko, R.; Kazaoui, S.; Lee, J.-J.; Noda, T.; Islam, A. Coadditive engineering with 5-ammonium valeric acid iodide for efficient and stable Sn perovskite solar cells. *ACS Energy Lett.* **2018,** *4* (1), 278-284.

(49) Kayesh, M. E.; Chowdhury, T. H.; Matsuishi, K.; Kaneko, R.; Kazaoui, S.; Lee, J.-J.; Noda, T.; Islam, A. Enhanced photovoltaic performance of $FASnI_3$-based perovskite solar cells with hydrazinium chloride coadditive. *ACS Energy Lett.* **2018,** *3*, 1584-1589.

(50) Jokar, E.; Chien, C.-H.; Fathi, A.; Rameez, M.; Chang, Y.-H.; Diau, E. W.-G. Slow surface passivation and crystal relaxation with additives to improve device performance and durability for tin-based perovskite solar cells. *Energy Environ. Sci.* **2018,** *11* (9), 2353-2362.

(51) Gu, F.; Zhao, Z.; Wang, C.; Rao, H.; Zhao, B.; Liu, Z.; Bian, Z.; Huang, C. Lead‐free tin‐based perovskite solar cells: strategies toward high performance. *Sol. RRL* **2019**, 3 (9), 1900213.

(52) Jung, M.; Ji, S.-G.; Kim, G.; Seok, S. Perovskite precursor solution chemistry: from fundamentals to photovoltaic applications. *Chem. Soc. Rev.* **2019,** *48*, 2011-2038.

(53) Kumar, M. H.; Dharani, S.; Leong, W. L.; Boix, P. P.; Prabhakar, R. R.; Baikie, T.; Shi, C.; Ding, H.; Ramesh, R.; Asta, M.; Mathews, N. Lead-free halide perovskite solar cells with high photocurrents realized through vacancy modulation. *Adv. Mater.* **2014,** *26* (41), 7122-7127.

(54) Noel, N. K.; Stranks, S. D.; Abate, A.; Wehrenfennig, C.; Guarnera, S.; Haghighirad, A.-A.; Sadhanala, A.; Eperon, G. E.; Pathak, S. K.; Johnston, M.; Snaith, H. Lead-free organic–inorganic tin halide perovskites for photovoltaic applications. *Energy Environ. Sci.* **2014**, 7, 3061-3068.

(55) Cao, W.; Hu, Z.; Lin, Z.; Guo, X.; Su, J.; Chang, J.; Hao, Y. Defects and doping engineering towards high performance lead-free or lead-less perovskite solar cells. *J. Energy Chem.* **2021**, 68, 420-438.

(56) Li, Y.; Wu, H.; Qi, W.; Zhou, X.; Li, J.; Cheng, J.; Zhao, Y.; Li, Y.; Zhang, X. Passivation of defects in perovskite solar cell: From a chemistry point of view. *Nano Energy* **2020**, 77, 105237.

(57) Chen, Y.; Zhou, H. Defects chemistry in high-efficiency and stable perovskite solar cells. J. *Appl. Phys.* **2020**, 128, 060903.

(58) Ono, L. K.; Liu, S.; Qi, Y. Reducing detrimental defects for high-performance metal halide perovskite solar cells. *Angew. Chem. Int. Ed.* **2020,** *59*, 6676-6698.

(58) Green, M. J. S. c. e. t. P. i. P. A, Hishikawa Y, Dunlop ED, Levi DH, Hohl-Ebinger J, Ho-Baillie AWY. Solar Cell Efficiency Tables (version 51). *Prog Photovolt Res Appl.* **2018,** *26*, 3-12.

(59) Cao, J.; Yan, F. Recent progress in tin-based perovskite solar cells. *Energy Environ. Sci*. **2021,** *14* (3), 1286-1325.

(60) Wang, R.; Wang, J.; Tan, S.; Duan, Y.; Wang, Z.-K.; Yang, Y. Opportunities and challenges of lead-free perovskite optoelectronic devices. *Trends Chem.* **2019,** *1*, 368-379.

(61) Abate, A. Perovskite solar cells go lead free. *Joule* **2017**, 1, 659-664.

(62) (a) Abdel-Shakour, M.; Chowdhury, T. H.; Matsuishi, K.; Bedja, I.; Moritomo, Y.; Islam, A. High-Efficiency Tin Halide Perovskite Solar Cells: The Chemistry of Tin (II) Compounds and Their Interaction with Lewis Base Additives during Perovskite Film Formation. *Sol. RRL* **2021,** *5*, 2000606. (b) Emrul, M. Performance Enhancement of Solution-Processed Organic-Inorganic Halide Perovskite Solar Cells. *University of Tsukuba*, **2019**. (c) Kaneko, R. Dopant-Free Organic and Inorganic Hole Transport Materials for Perovskite Solar Cells. *Nihon University*, **2020**.

Chapter 2 Experimental

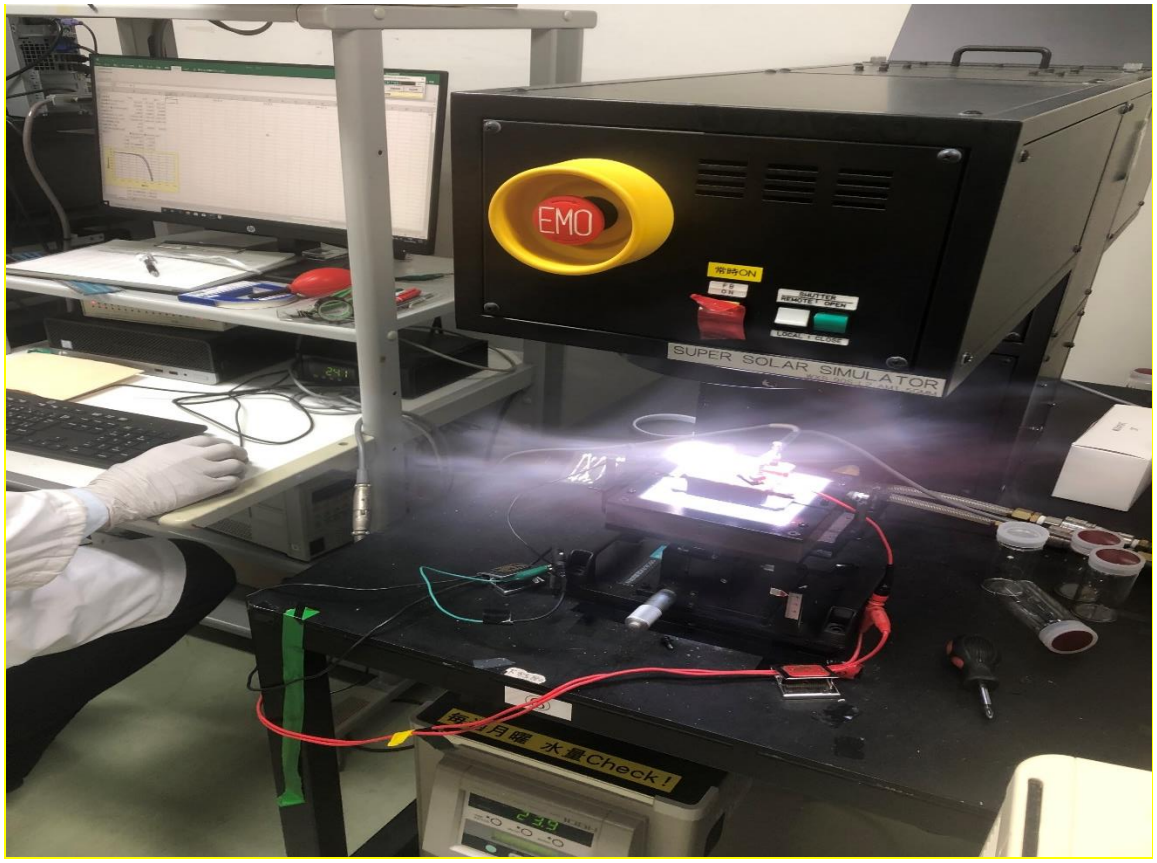

2.1 Materials

All the chemicals were used as received without any further purification, including PbI_2 (99%, Sigma–Aldrich), SnI_2 (99.99%, Sigma–Aldrich), Methyl ammonium iodide (MAI) (>98%, Tokyo Chemical Industry Co., Japan), Formamidine Hydroiodide (FAI) (> 98%, Tokyo Chemical Industry Co., Japan), acetylacetone (> 99.0%, GC) and 3-methyl-2,4-nonanedione (> 97.0%, GC) from (Tokyo Chemical Industry Co., Japan), Diaminomaleonitrile (>96.0%, Tokyo Chemical Industry Co., Japan), formamidine sulfinic acid(>93.0%, Tokyo Chemical Industry Co., Japan), SnF_2 (>99%, Sigma Aldrich), ethylenediammonium diiodide ($EDAI_2$) (Merck), Poly (3,4- ethylenedioxythiophene)- poly (styrenesulfonate) (PEDOT:PSS) (Clevious PVP Al 4083), Nickel acetylacetonate (95%, Sigma–Aldrich), PCBM (PhenylC_{61}-butyric acid methyl ester) (99.5%, Lumtec Co., Taiwan) and C_{60} (99.5%, Lumtec Co., Taiwan). Magnesium acetatetetrahydrate (99%), Bathocuproine (BCP) and super dehydrated solvents of Dimethylformamide (DMF) (Super Dehydrate, 99.5+%)), Dimethyl sulfoxide (DMSO)(Super Dehydrate, 99.0+%), chlorobenzene (anhydrous, 99.8%) and methanol, were all purchased from Wako Co., Japan.

2.2 Preparation of the adducts

The PbI_2-(β-diketones)$_x$ adducts were synthesized by mixing PbI_2 powders with excess ligand (molar ratio > 2) in DMF. Typically, 0.3 M of PbI_2 in DMF solvent was mixed with 0.9 M of the corresponding Lewis bases acac and R-acac followed by stirring for 30 min at room temperature. The adduct precipitate was obtained after cooling the reaction mixture to room temperature overnight. Finally, the obtained powders were washed by toluene to remove excess molecules.

The SnI_2-DAMN or SnI_2-$FASO_2H$ adducts was prepared by mixing SnI_2 (50 mg, 0.134 mmol) with DAMN (17.29 mg, 0.16 mmol) or $FASO_2H$ (17.29 mg, 0.16 mmol) in 400 μL of DMSO. The reaction mixture was stirred for 30 minutes. Then the reaction mixture was kept overnight. The final precipitate was collected, washed with chlorobenzene and dried under vacuum.

2.3 Fabrication of perovskite solar cells

2.3.1 Fabrication of Pb-Based Perovskite Solar Cells

(A) Perovskite film fabrication:

The precursor solution of the $MAPbI_3$ perovskite was prepared by mixing 1.2 mmol of PbI_2 and MAI in 1.8 ml of the mixed solvent (DMF:DMSO; 4:1% volume). The perovskite film was deposited by spin-coating 70 µL of precursor solution at 5000 rpm for 42 s. During the spin-coating, typically 100 µL of chlorobenzene anti-solvent without and with β-diketones ligands (60 mM) was dripped on the substrate after 17 s, then the spin-coated films were annealed at 100 °C for 30 min.

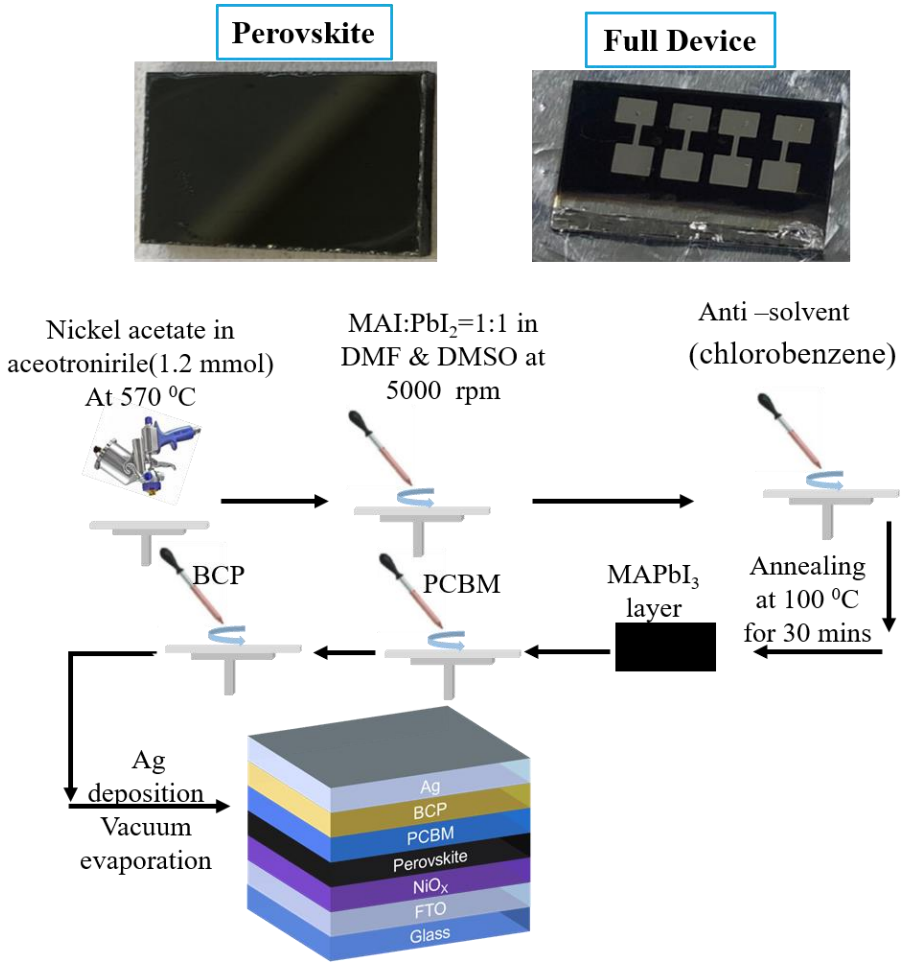

Thickness of each layer	
Layer	Thickness (nm)
NiO_X	~ 20
Perovskite	~ 350
PCBM	~ 65
BCP	~ 10
Silver (Ag)	~ 100

Figure 1. The fabrication steps of Pb-based perovskite solar cells.

(B) Solar cells fabrication:

The PSCs were fabricated on the patterned fluorine-doped tin oxide (FTO) coated glass substrates. The substrates were ultrasonically cleaned with detergent, deionized water, acetone, and

ethanol, respectively, for 15 min each. The cleaned substrates were treated with ultraviolet/ozone radiation for 30 min. The NiO_x layer was deposited onto the FTO substrate by spraying a nickel acetylacetonate solution and magnesium acetate tetrahydrate in acetonitrile/ethanol (with 95:5% volume) at 570 °C. The NiO_x films were then annealed at 570 °C for 15 min and cooled down to room temperature. After cooling at room temperature, the substrates were transferred to the glove box, and the $MAPbI_3$ perovskite films were deposited. An electron transporting layer PCBM (20 $mgml^{-1}$ in chlorobenzene) and BCP (0.5 $mgml^{-1}$ in methanol) were deposited by spin-coating at 1000 rpm for 30 s and 6000 rpm for 30 s, respectively. Finally, a 100 nm thick silver layer was vacuum-deposited through a shadow mask with an active area of 0.09 cm^2. The steps of Pb-PSCs fabrication are given in **Figure 1**.

2.3.2 Fabrication of Sn-Based Perovskite Solar Cells

(A)Perovskite film fabrication:

An equimolar ratio of (1 mmol) SnI_2 and FAI with 10 mol% SnF_2 in 600µL DMSO solvent were mixed for the $FASnI_3$ perovskite film preparation. For the modified perovskite solution, a varying amount of additives DAMN or $FASO_2H$ was added. ~1 mol% of the $EDAI_2$ was added to all of the precursor solutions.

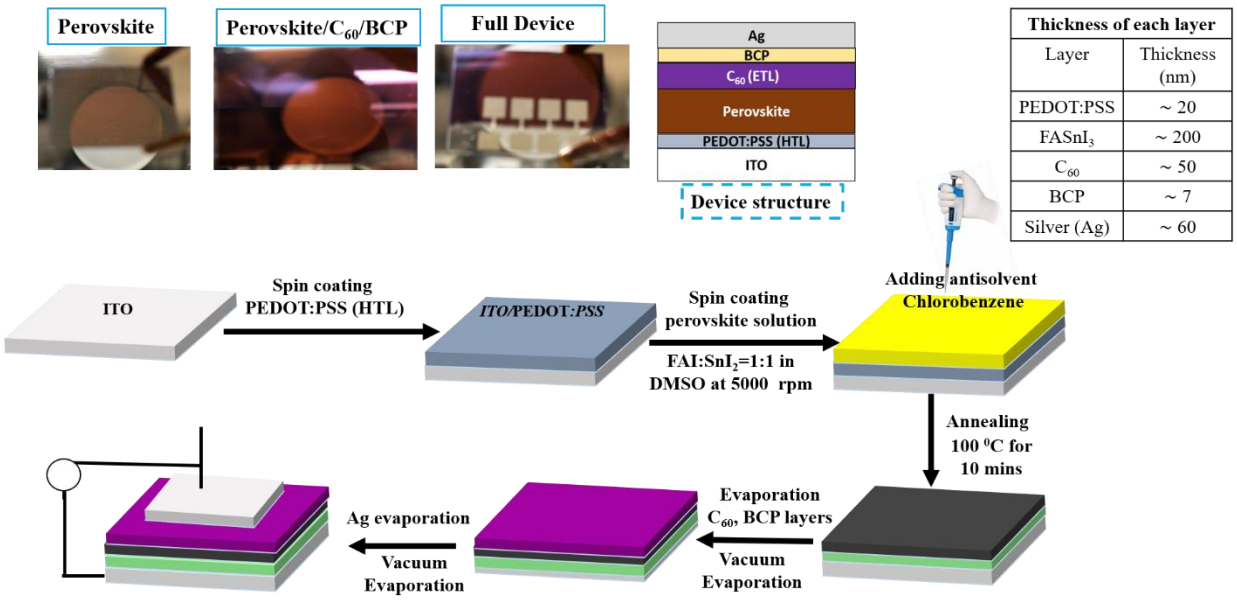

Figure 2. The fabrication steps of the Sn-based perovskite solar cells.

(B) Solar cells fabrication:

PSCs were fabricated on the well-cleaned indium tin oxide (ITO) coated glass substrates. Then ultraviolet (UV)/ozone radiation was used for 30 minutes to remove any contamination from the cleaned ITO substrates. The poly(3,4-ethylenedioxythiophene) polystyrene sulfonate (PEDOT:PSS, (1.3-1.7 wt%)) layer was deposited on top of the ITO substrate by spin-coating at 4000 rpm for 30 s. The PEDOT:PSS films were then annealed at 150 °C for 30 min and cooled down to room temperature. After cooling at room temperature, the substrates were transferred to the N_2 glove box and the $FASnI_3$ films were deposited. The perovskite films were deposited by spin-coating the precursor solution at 5000 rpm for 75 s. Chlorobenzene was dripped on the substrate after 20 seconds of spin coating. Subsequently, C_{60} (50nm) and BCP (7 nm) were deposited by thermal evaporation at the rate of 1.0 /s. Finally, a 60 nm thick Ag layer was vacuum-deposited through a shadow mask with an active area of 0.09 cm^2. The steps of Sn-PSCs fabrication are given in **Figure 2**.

2.4 Characterization

The Fourier transform infrared (FTIR) was performed to study the bonding between the used Lewis base additives with PbI_2 or SnI_2. The X-ray diffraction (XRD) was carried on the perovskite films to confirm the crystal structure. X -ray photoelectron spectroscopy (XPS) was performed on the film deposited on the glass substrate by using PHI Quantera SXM (ULVAC- PHI). XPS measurement was carried out at an ultrahigh vacuum as high as $5x10^{-11}$ mbar. X-ray from monochromatic Al Kα source (hυ =1486.7 eV) was used to excite the samples and electrons were detected at 45° take-off angle. Multipack software was used for curve fitting. Scanning electron microscope (SEM) images were obtained by using a JSM- 6500F field-emission scanning electron microscope under an acceleration voltage of 5 kV. The UV−visible (UV–vis) absorption was used to study the absorption spectra of the perovskite films. The photoelectron emission spectra measured using AC-3E photoelectron spectrometer. Both UV−visible absorption spectra and AC-3E data were used to construct the energy band diagram of the perovskite films. The steady-state photoluminescence (PL) and time-resolved photoluminescence (TRPL) spectra were measured to understand the charge

transfer properties and kinetics of the fabricated perovskite films. The changes in electron mobility and electron trap-state density of the perovskite films were evaluated by dark current-voltage ($J-V$) analysis for electron-only devices. To investigate the effect of Lewis base additives on the photovoltaic performance of PSCs, we fabricated the PSCs. The current density-voltage (J-V) and incident photon to current efficiency (IPCE) of the fabricated PSCs were measured. The transient photocurrent (TPC) decay and a transient photovoltage (TPV) decay were performed in the PSCs to get information about the electron transportation process and the change in the carrier recombination process. The charge recombination of the PSCs was also examined using electrochemical impedance spectroscopy (EIS). Finally, the operational stability under maximum power point conditions and stability inside the N_2 glovebox were checked. Some images of the instrumental tools used for fabrication and characterization of PSCs are given in **Figure 3**.

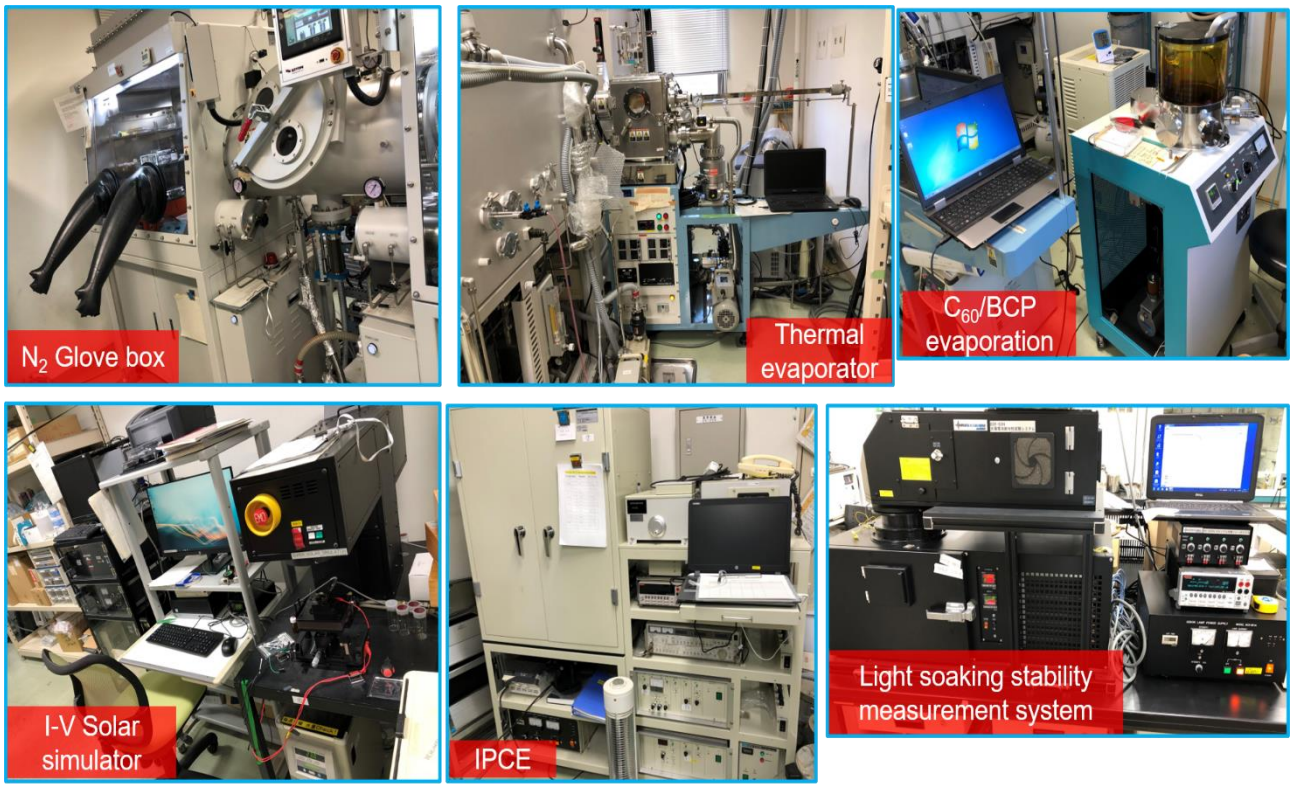

Figure 3. The instrumental tools used for fabrication and characterization of perovskite solar cells/

Chapter 3 Results and Discussion

3.1 Chemical passivation of the under coordinated Pb^{2+} defects in inverted planar perovskite solar cells via β-diketone Lewis base additives

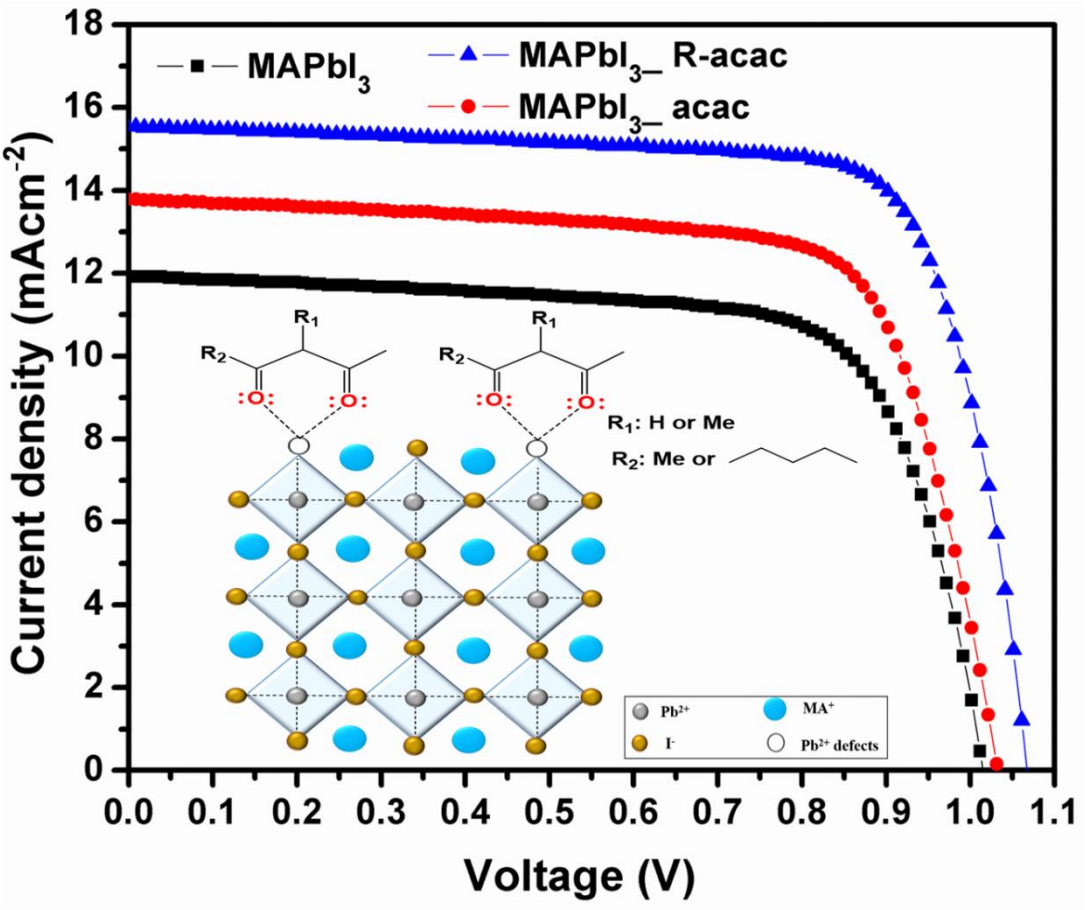

3.1.1 β-diketone Lewis base additives

Trap states at the surface and in GBs can easily be generated by perovskite films fabricated using the solution approach, which affects the photovoltaic performance of PSCs. [1-5] The majority of surface or grain boundary traps are produced by ion migration, oxidization of I^-, or evaporation of methylammonium iodide, which are mainly revealed as under coordinated metal cations or halide anions. [6, 7]. These defects are generated due to the low thermal stability of the $MAPbI_3$, which causes a nonstoichiometric composition and decompose the $MAPbI_3$ to PbI_2 on the surface or at the GBs. [8, 9] As a result, the perovskite films develop a net positive charge, which could imapct the photovoltaic performance in the resultant PSCs, such as V_{OC}, J_{SC}, FF, and PCE. [9] Thus, it is necessary to eliminate these under coordinated Pb^{2+} defects, which were originally expected to be the major source of charge traps. [10, 11] While numerous sensitive approaches have been utilized to investigate the surface defects of perovskite single crystals [12, 13], the defect configuration created during solution processing or evaporation is significantly more complicated in perovskite films. Fortunately, the Lewis base chemistry has been used as an effective methodology for the passivation of the under coordinated sites. [14, 15] PSCs performance can be improved by the formation of adducts with the defects, which can limit non-radiative charge recombination. [9] The defect passivation was induced by creating a coordination bond using a variety of surface passivators. For example, Zhao et al. showed the function of benzylamine Lewis base as a passivator on top of the perovskite layer reduced the traps by forming a coordination bond with the under coordinated Pb^{2+}.[16] Snaith et al. revealed that the Lewis base molecules thiophene or pyridine might be used to repair trapped states in perovskite films by establishing coordination with under coordinated Pb^{2+} ions. [14] Recently, Han et al. reported using organic dyes with the antisolvent chlorobenzene, which passivated the under coordinated Pb^{2+} by forming a coordination bond using its carboxylic group. [17] However, few studies have explored the use of bidentate Lewis base additives as trap passivators, which can form a more stable bond and so help to suppress such defects. Herein, the passivation of

surface defects in $MAPbI_3$ perovskite film was performed by the incorporating two β-diketone Lewis base additives 2,4-pentanedione (acetylacetone; acac) and 3-methyl-2,4-nonanedione (R-acac) with the chlorobenzene antisolvent. The chemical structures of acac and R-acac has been shown in **Figure 1**. The chlorobenzene's role is to speed up the heterogeneous nucleation and the formation of a homogenous perovskite layer with crystalline properties. [1] The β-diketone additives can interact with the under coordinated Pb^{2+} using carbonyl (C=O) groups. Through bidentate anchoring, this interaction can provide optimum binding strength and adhesion to the perovskite layer, hence reducing defects inside the perovskite lattice. These additives can also facilitate the complete conversion of PbI_2 to the $MAPbI_3$ perovskite crystals with better morphology by the dissolution of the non-converted PbI_2.

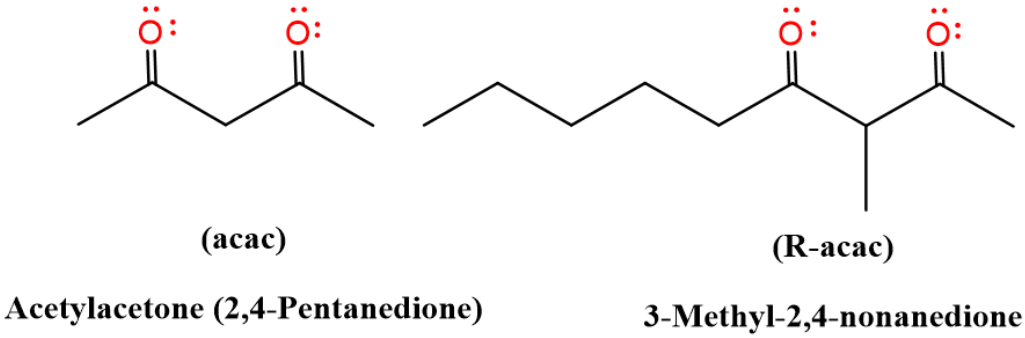

Figure 1. The chemical structures of the acac and R-acac

3.1.2 The formation of PbI_2-(β-diketones)$_x$ adduct

The β-diketones can be tautomerized in two forms, the enol form (80%) and the keto form (20%) [18]. The enol form of the β-diketones can easily loss the proton due to the lower acidity which resulted in the formation of anionic moiety acting as a strong bidentate ligand [19, 20]. The interaction of the Pb^{2+} with acac and R-acac ligands has been elucidated using the FTIR spectra of the prepared adducts PbI_2-(acac)$_x$ and PbI_2-(R-acac)$_x$. As we can see from **Figure 2a**, the PbI_2 did not show any peak at 1600–1700 cm^{-1} region. While the two ligands acac and R-acc showed peaks at 1608 cm^{-1} and 1624 cm^{-1}, respectively, corresponding to the coupled enolic C=O and C=C stretching vibration of the β-diketones [18]. After the binding with PbI_2, the enolic peak of β-diketones was shifted to

1635 cm^{-1} and 1630 cm^{-1} for PbI_2-$(acac)_x$ and PbI_2-$(R\text{-}acac)_x$ adducts, respectively, which indicated the interaction between the ligands and PbI_2. [18, 21] To gain more information about the anchoring of the two ligands with PbI_2, we measured the UV–vis absorption spectra for the PbI_2, PbI_2-$(acac)_x$ and PbI_2-$(R\text{-}acac)_x$ solutions in DMF. As shown in **Figure 2b**, the absorption spectra of the PbI_2 solution shows two peaks at 270 nm and 321 nm, respectively, which are related to solvated PbI^+/PbI_2 or a combination of the two species. [22] For the PbI_2-$(acac)_x$ adduct, the peak at 321 nm was reduced and become a shoulder, while for the PbI_2-$(R\text{-}acac)_x$ adduct the peak totally disappeared.

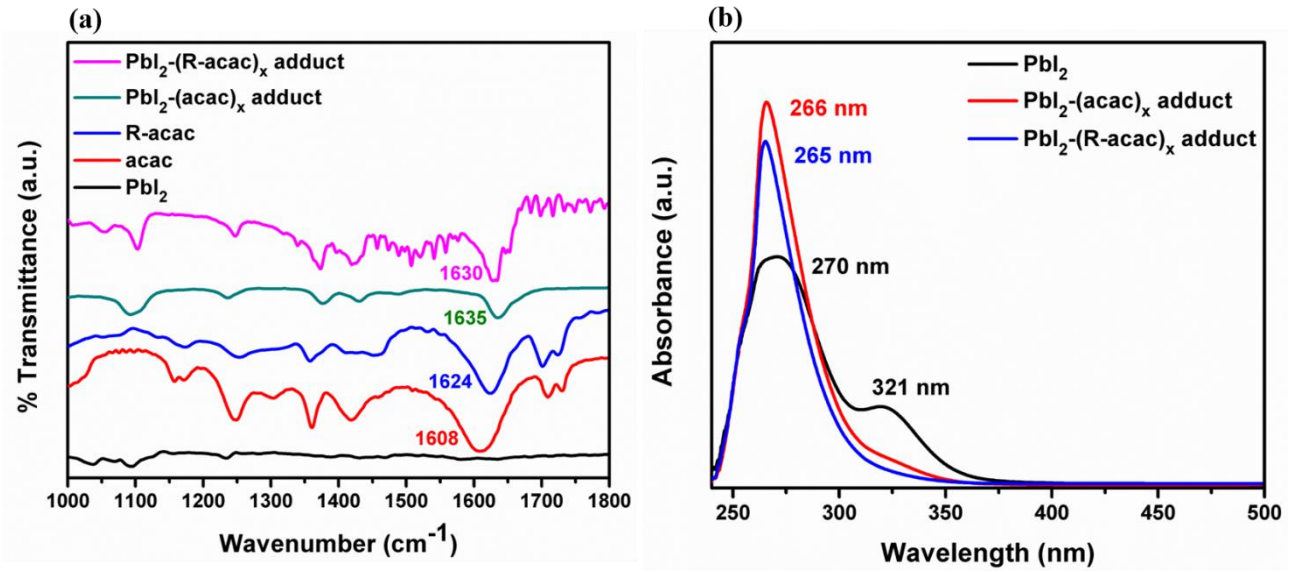

Fig. 2 a) The FTIR of the PbI_2, acac ligand, R-acac ligand, PbI_2-$(acac)_x$ and PbI_2-$(R\text{-}acac)_x$ powders; b) The UV–vis absorption of PbI_2, PbI_2-$(acac)_x$ and PbI_2-$(R\text{-}acac)_x$ solutions in DMF (1.25×10^{-5} M)

3.1.3 Perovskite films formation

Since the β-diketones ligands possess enhanced binding strength using their two carbonyl groups to form a stabilized coordination. [19, 20] The acac and R-acac Lewis bases have been used as a passivator for the $MAPbI_3$ perovskite films to chelate the under coordinated Pb^{2+} defects. The two additives were added within the antisolvent chlorobenzene and dripped on top of the spin-coated perovskite precursor compared to the chlorobenzene antisolvent only (pristine) as illustrated in **Figure 3a**. By this way, the two additives can interact with Pb^{2+} defects and suppress the surface traps generated from the under coordinated Pb^{2+} structural defects [23] as schematically shown in

Figure 3b.

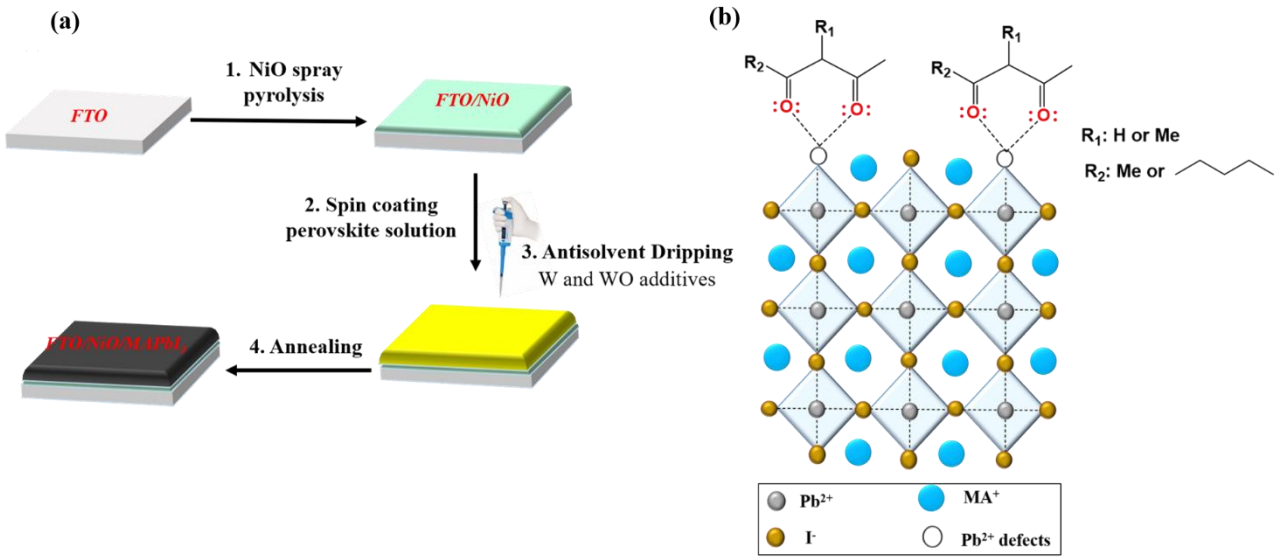

Figure 3. (a) The addition of the modified antisolvent during fabrication process. (b) Schematic illustration of the defect's passivation using β-diketone ligands.

3.1.4 Photophysical and morphological properties of the perovskite films

The two Lewis base additives acac and R-acac were added to the antisolvent chlorobenzene during the fabrication of the $MAPbI_3$ perovskite film. The UV–vis spectra of the films were measured to investigate the change in absorption spectra for the $MAPbI_3$ perovskite film when the antisolvent was added with and without acac and R-acac. From the absorption spectra shown in **Figure 4a**, we can see the presence of the absorption band edge at 780 nm, which corresponds to the bandgap excitation of $MAPbI_3$ perovskite material. The $MAPbI_3$ perovskite films fabricated with acac and R-acac show a slight increase in the absorption intensity which indicates improved film quality. [24] The PL is a useful tool for obtaining information regarding passivation. The strong PL response is commonly considered to be a sign of a high-quality surface. [25] Stronger emission of the perovskite materials is related to the reduced surface-trap states and defects in the perovskite film, which are responsible for non-radiative recombination. As shown from **Figure 4b**, the PL intensity of passivated films by acac and R-acac exhibits enhanced intensity as compared to the pristine one. This suggests that including acac and R-acac in the antisolvent can effectively passivate surface defects while also reducing non-radiative recombination channels. [26] Furthermore, the PL peak of the perovskite films

after passivation was blue shifted from 774 nm of the pristine compared to 772 nm and 769 nm for acac and R-acac passivated films, respectively. This blue shift indicates that the introduction of β-diketone Lewis bases formed perovskite films with less defect states. [27]

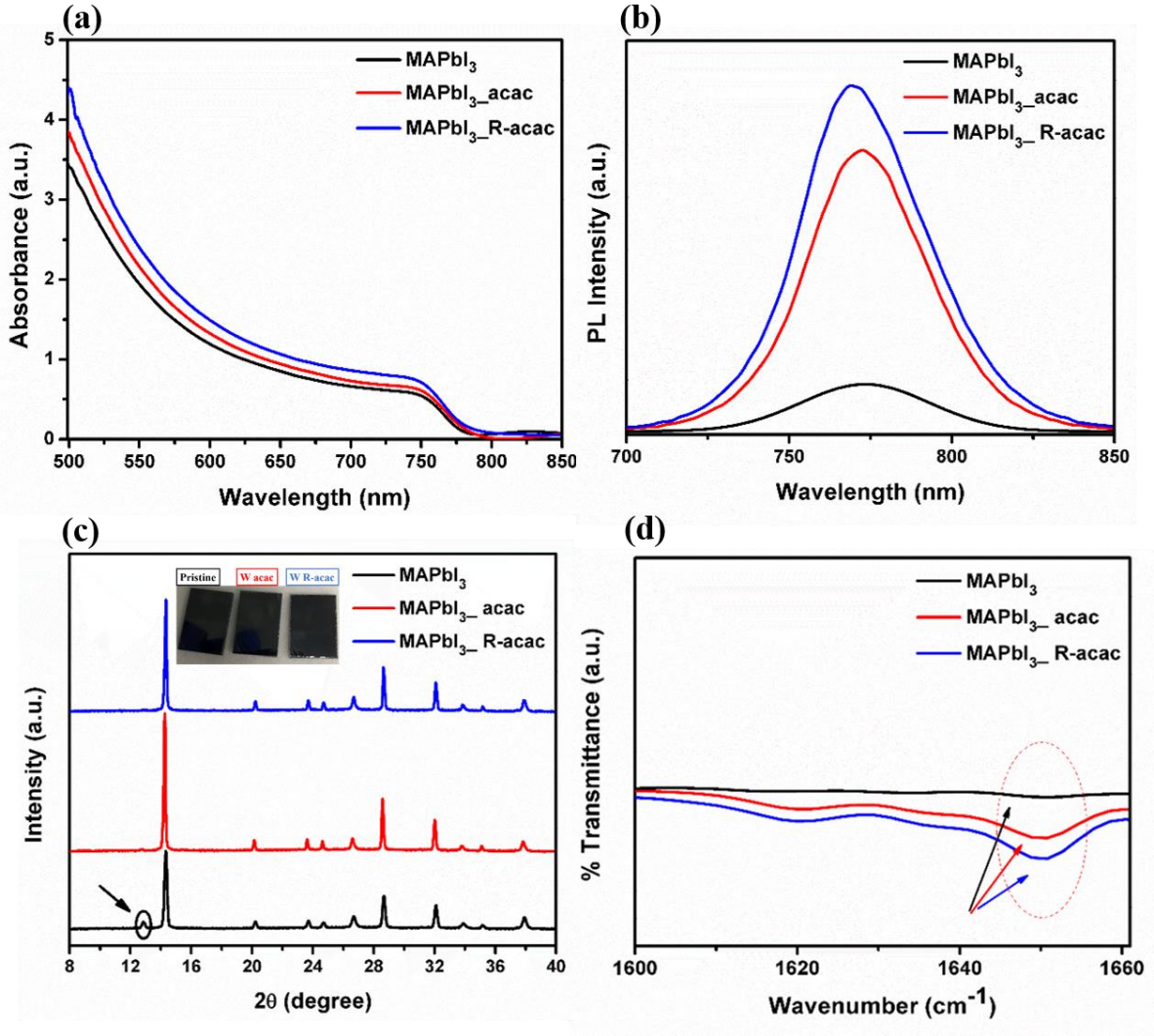

Figure 4. (a) UV–vis absorption; (b) PL; (c) XRD; (d) FTIR of the pristine and modified $MAPbI_3$ perovskite films using the chlorobenzene antisolvent compared to chlorobenzene antisolvent modified with acac and R-acac

XRD was carried out on the $MAPbI_3$ perovskite films in order to get insight into the structural effects of utilizing the modified antisolvent with acac and R-acac on the phase and crystallinity of the perovskite film. As indicated from the XRD pattern in **Figure 4c**, the three main peaks were observed at 14.30°, 28.60° and 32.08° and represented by (110), (220) and (310) planes, respectively, indicating the formation of tetragonal $MAPbI_3$. [21, 28] For the perovskite films fabricated with acac and R-

acac, the full width at half maximum (FWHM) was decreased compared to the pristine film (see **Table 1**). The decreased FWHM for the acac and R-acac indicates the improved crystallinity of the $MAPbI_3$ absorber layer after using these additives. [29] Furthermore, the modified antisolvent could induce complete conversion to the perovskite material $MAPbI_3$ without any remaining non-converted PbI_2 (see **Figure 4c**) by the disappearance of the small peak at 2θ of 12.7°). [30] Importantly, we could confirm from **Figure 4c** that, the large-size molecules acac and R-acac could not affect the formation of the perovskite film or permeate into the perovskite crystal to induce a phase transition or form the 2D structure on the surface and GBs of perovskite films. [31]

Table 1. The FWHM of the pristine and modified perovskite films at peaks 14.30°, 28.60 ° and 32.08 °.

Peak	$MAPbI_3$ Perovskite film	$MAPbI_3$_acac Perovskite film	$MAPbI_3$_R-acac Perovskite film
14.3°	0.135°	0.126°	0.121°
28.6°	0.098°	0.099°	0.094°
32.08°	0.126°	0.118°	0.117°

To understand the interaction of acac and R-acac with the fabricated perovskite film, the FTIR for the pristine and modified perovskite films was measured. As shown in **Figure 4d**, the pristine perovskite film based on chlorobenzene antisolvent only did not show any peak at this region. However, a peak at around 1650 cm^{-1} for the two modified perovskite films was observed, which is corresponding to the (C=O) group [32, 33] of the β-diketone additives interacted with Pb^{2+}. Interestingly, the intensity of the FTIR peaks increased for the modified films compared to the pristine ones, which suggested that acac and R-acac are indeed passivating the perovskite surface. [34]

The SEM of perovskite films was measured to investigate the influence of the two additives within the antisolvent on the morphology of the perovskite films. As observed from the SEM images in **Figure 5a–c**, the utilizing of the two β-diketone ligands with chlorobenzene antisolvent could cure the defects at the GBs, which resulted in the formation of compact perovskite film with fewer defects and compact morphology. The grain size distributions of the perovskite films in **Figure 5d–f** showed

a higher distribution for the larger grain size (from 285 to 515 nm) on the modified perovskite films as compared to the pristine.

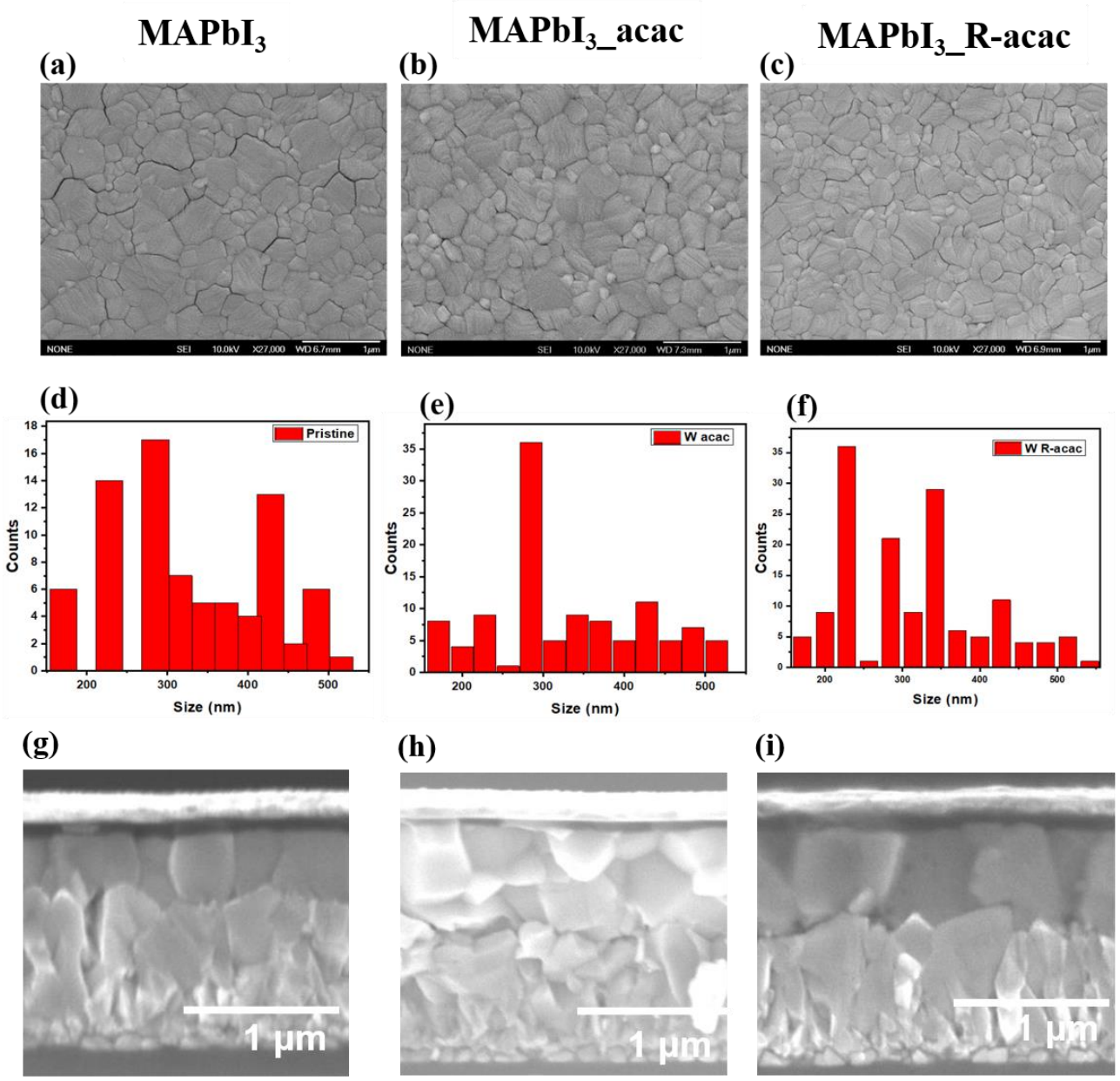

Figure 5. (a–c) The surface SEM and d–f the grain size distribution of the pristine perovskite film, acac and R-acac based perovskite films, respectively. (g–i) The cross sectional of the fabricated PSCs without and with additives

3.1.5 The photovoltaic performance

To study the effect of using the modified antisolvent on photovoltaic performance, the inverted planar device structure p-i-n (FTO/NiO_x/$MAPbI_3$/PCBM/BCP/Ag) was fabricated. The cross sections

of the fabricated PSCs without and with additives are depicted in **Figure 5g–i**. The device structure of the inverted PSCs is given in **Figure 6a**. The PSCs exhibited similar IPCE from the visible to the near-IR (300–800 nm) region as shown in **Figure 6b**. It is clear from the analysis that incorporating the additives with chlorobenzene antisolvent enhanced the IPCE of the PSCs, which is attributed to improved light absorption, charge transport and collection abilities [35]. Furthermore, the integrated J_{SC} from the IPCE curve is matched well with the measured J_{SC}, as shown in **Table 2**. The *J-V* curves of the PSCs based on pristine and passivated $MAPbI_3$ are given in **Figure 6c**, and the detailed photovoltaic parameters are listed in **Table 2**. The pristine device based on chlorobenzene antisolvent exhibited PCE 8.67% with a V_{OC} of 1.015 V, J_{SC} of 11.92 mA/cm^2 and FF of 72%. Interestingly, when acac was added to chlorobenzene antisolvent under the same conditions the device J_{SC}, Voc and FF increased to 13.79 mA/cm^2, 1.032 V and 73%, respectively; thus, the PCE jumped to 10.34%. Furthermore, by using R-acac additive, the device showed enhanced J_{SC} of 15.54 mA/cm^2, V_{OC} of 1.067 V and FF of 76 % with the highest PCE of 12.63%.

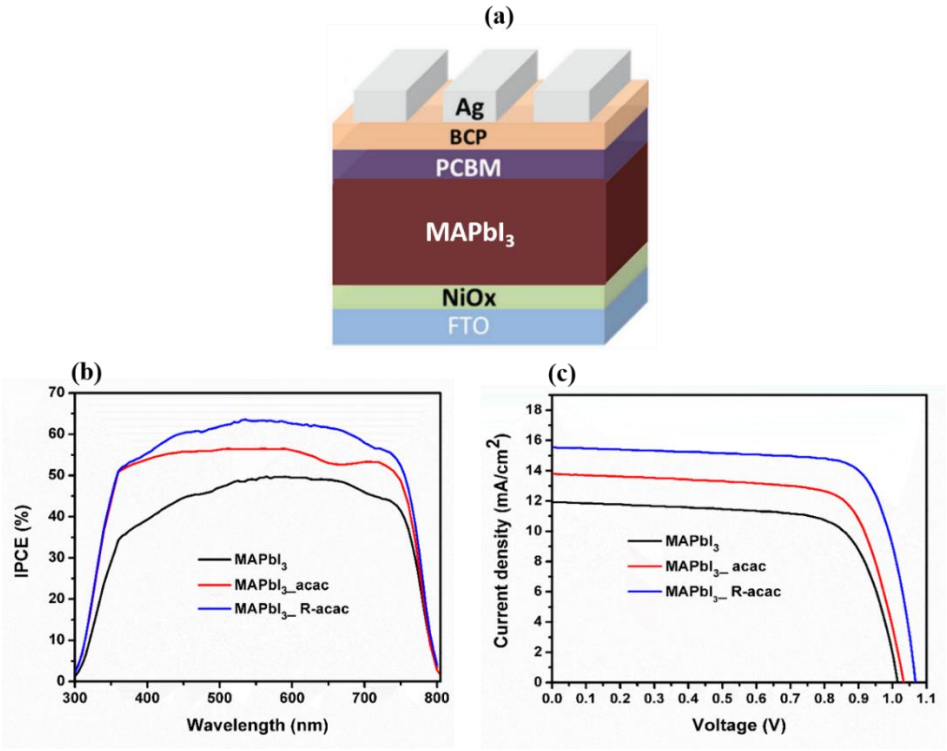

Figure 6. a) Device structure of the fabricated inverted PSCs; b, c) IPCE and *J–V* curves of the PSCs fabricated with chlorobenzene antisolvent compared to the chlorobenzene antisolvent modified with acac and R-acac

Table 2. The photovoltaic performance of $MAPbI_3$, $MAPbI_3$_aca**c** and $MAPbI_3$_R-acac based PSCs.

	Scan	J_{SC} (mA cm-^{2})	J_{SC}[a] (mA cm-^{2})	V_{OC} (V)	F.F	PCE (%)	HI	Rs (Ωcm^2)	Rsh (Ω cm^2)
$MAPbI_3$	F	11.92		0.976	0.69	8.09			
	R	11.92	11.8	1.015	0.72	8.67	0.06	7.99	539.25
	F	14.18		0.986	0.73	10.17			
$MAPbI_3$_acac	R	13.79	13.8	1.032	0.73	10.34	0.01	6.84	440.5
	F	15.88		1.028	0.74	12.02			
$MAPbI_3$_R-acac	R	15.54	15.25	1.067	0.76	12.63	0.04	5.96	638.3

[a]The integrated current density from the IPCE spectra

The two additives could successfully help in curing the device defects which resulted in increasing the V_{OC} by 17 mV and 52 mV for the device based on acac and R-aca, respectively, compared to the pristine PSCs. The increase in V_{OC} could be attributed to the deactivation of traps through passivation [9]; these traps normally create many pathways for the recombination, which reduce the splitting of quasi-Fermi level and consequently diminish the V_{OC} [36]. The addition of passivation agents can improve the perovskite film quality with less defects [9]. The perovskite film with less morphological defect at the surface will form a better contact between the ETL and the HTL. This resulted in the reduction of the surface charge trap site at perovskite/ETL or perovskite/HTL interface. In addition to improving the charge collection efficiency of solar cells [21]; hence the J_{SC} of the device also was enhanced [37]. The increased FF for the modified PSCs compared to the pristine suggests that charge transportation in the modified films is more facile than that of pristine. The decrease in Rs and increase of Rsh after using the additives indicate the better contact between different layers which enhanced the FF from 0.72 to 0.73 and 0.76 for the pristine and modified PSCs, respectively (**Table 2**). We believe that the improved J_{SC} and FF are likely due to a more favorable perovskite films with less defects, leading to a compact perovskite surface [21].

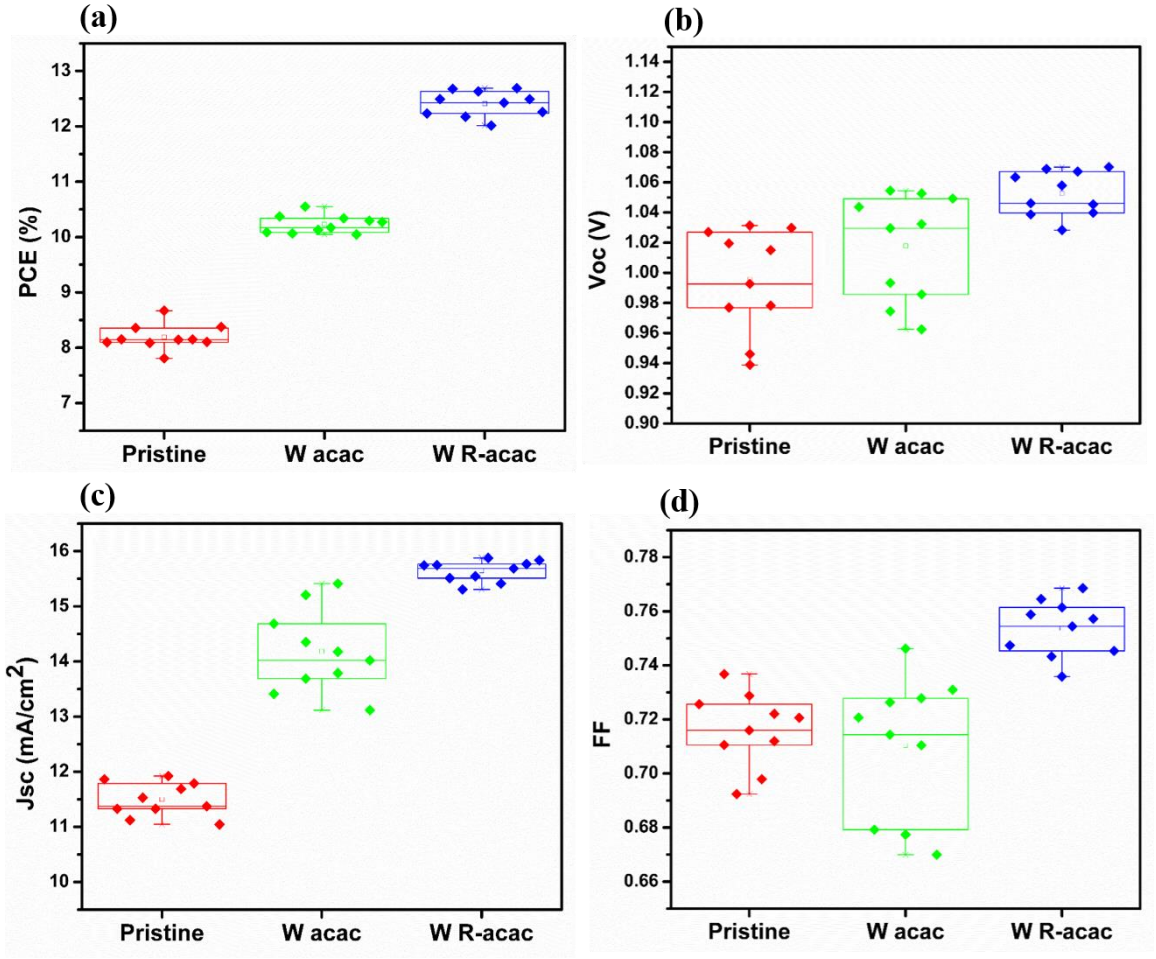

Figure 7. Statistical distribution of the (a) PCE; (b) V_{OC}; (c) J_{SC}; (d) FF of the PSCs with or without passivation

3.1.6 Stability and reproducibility

The PCE of the fabricated PSCs showed a good reproducibility as shown in **Figure 7a** and the PSCs based on R-acac passivation showed the best average performance. Furthermore, the average V_{OC} enhancement caused by R-acac passivation is the highest between all other fabricated PSCs as shown by **Figure 7b**. Additionally, we can observe the improvement of the J_{SC} and FF after passivation (see **Figure 7c, d**), which resulted from reducing the defects and improving the perovskite film quality.

Furthermore, the *J-V* hysteresis of the PSCs was also investigated, as shown in **Figure 8a–c** and **Table 2**. The hysteresis index (HI) [HI = (PCE $_{Reverse}$ − PCE $_{Forward}$)/PCE $_{Reverse}$)] [11, 38] was decreased after using the additives as following 0.06, 0.01 and 0.04 for the pristine device, acac and

R-acac based PSCs respectively, which confirm enhancing the stability of the PSCs after using the additives.

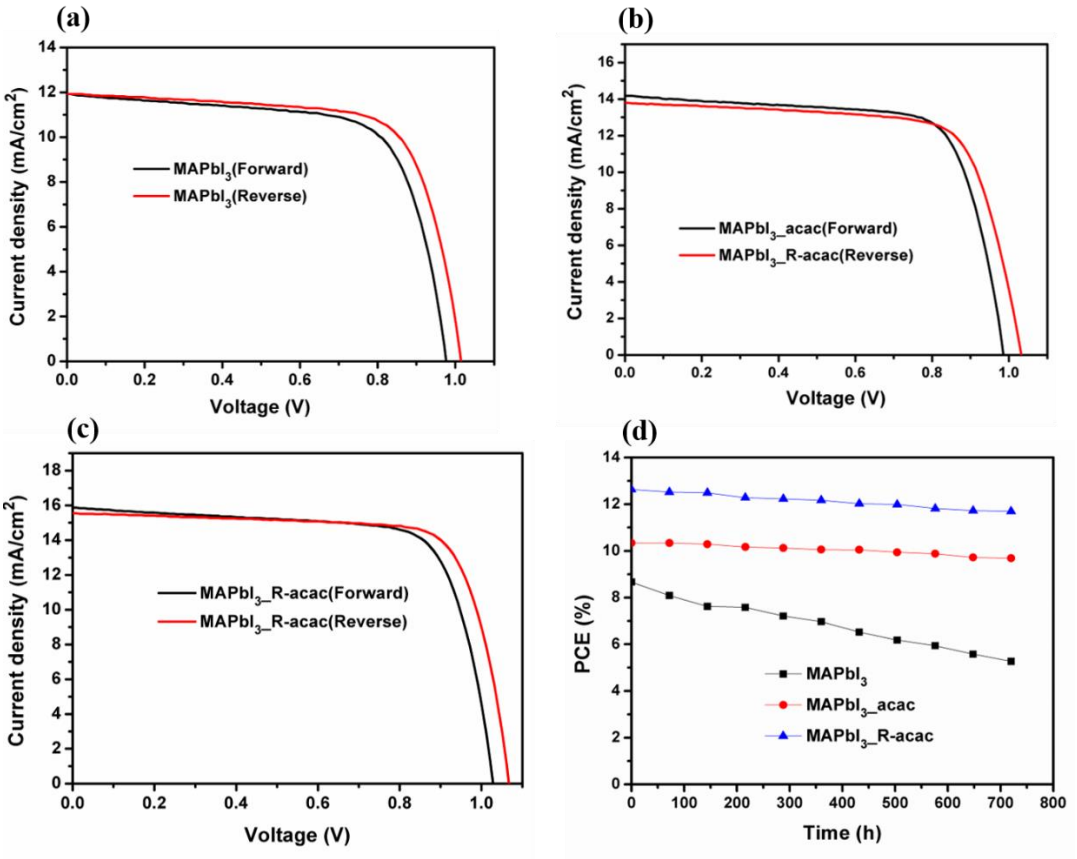

Figure 8. (a–c) The forward and reverse scan of the PSCs fabricated using: chlorobenzene antisolvent; chlorobenzene antisolvent modified with acac and R-acac, respectively. (d) The PCE stability over time for the pristine and modified PSCs.

The stability of the respective PSCs was measured as shown in **Figure 8d**. The acac and R-acac based PSCs showed improved stability as compared to the pristine when measured for a period of 720 h. The reduced hysteresis and improved stability can be attributed to the interaction between the additives and the perovskite, which suppresses the defects and improve the perovskite film quality [39].

Interestingly, it could be understandable from the results that the PSCs based on R-acac passivator showed better photovoltaic properties compared to acac, which may be attributed to the presence of a longer alkyl chain of R-acac [29]. The presence of donating alkyl chain stabilized the negative charge of the carbonyl group leading to the enhanced binding ability of R-acac with Pb^{2+} [40].

3.1.7 Summary

Using a one-step spin-coating method, two bidentate anchors acac and R-acac were used to chemically passivate the under coordinated Pb^{2+} defects on the perovskite films. The two β-diketone passivators could successfully interact with Pb^{2+} defects by forming a coordination bond using the two carbonyl groups. The interaction between PbI_2 and the two Lewis base passivators was confirmed by measuring the FTIR, XRD and UV–vis of the prepared adducts. The FTIR for the modified perovskite films showed a clear peak for C=O group, which ensured the interaction. The two Lewis bases showed enhanced passivation for the defects compared to the pristine, which has been clarified by the intensity of the PL peaks and the blue shift for the passivated perovskite films. Consequently, the PCE increased by 19% and 45% for the acac and R-acac passivated PSCs, respectively, compared to the pristine PSC. The effective passivation for R-acac Lewis base can be attributed to the presence of longer alkyl chains, which helps in the formation of a more stable bond with the under coordinated Pb^{2+} defects. These results ensured the enhancement effect of using the bidentate ligands, which can efficiently passivate the surface defects of the PSCs. Further work can be applied by utilizing a molecularly effective ligand with different functional groups to stabilize the coordination bond with defects for improving the photovoltaic performance of PSCs.

3.1.8 References

(1) Kayesh, M. E.; Matsuishi, K., Chowdhury; T. H., Kaneko, R.; Lee, J.-J.; Noda, T. Influence of anti-solvents on $CH_3NH_3PbI_3$ films surface morphology for fabricating efficient and stable inverted planar perovskite solar cells. *Thin Solid Films* **2018***,* 663, 105–115.

(2) Liu, S.; Guan, Y.; Sheng, Y.; Hu, Y.; Rong, Y.; Mei, A. A review on additives for halide perovskite solar cells. *Adv. Energy Mater.* **2020**, 10, 1902492.

(3) Abdel-Shakour, M.; Chowdhury, T. H.; Matsuishi, K.; Bedja, I.; Moritomo, Y.; Islam, A. High efficiency tin halide perovskite solar cells: the chemistry of tin (II) compounds and their interaction with Lewis base additives during perovskite film formation. *Sol. RRL* **2020**, 5, 2000606.

(4) Yuan, Y.; Huang, J. Ion migration in organometal trihalide perovskite and its impact on photovoltaic efficiency and stability. *Acc. Chem. Res.* **2016**, 49, 286–293.

(5) Azpiroz, J. M.; Mosconi, E.; Bisquert, J.; De Angelis, F. Defect migration in methylammonium lead iodide and its role in perovskite solar cell operation. *Energy Environ. Sci.* **2015**, 8, 2118–2127.

(6) Son, D.-Y.; Lee, J.-W.; Choi, Y. J.; Jang, I.-H.; Lee, S.; Yoo,
P. J. Self-formed grain boundary healing layer for highly efficient $CH_3NH_3PbI_3$ perovskite solar cells. *Nat. Energy* **2016**, 1, 1–8.

(7) Shao, Y., Xiao, Z., Bi C.; Yuan, Y.; Huang, J. Origin and elimination of photocurrent hysteresis by fullerene passivation in $CH_3NH_3PbI_3$ planar heterojunction solar cells. *Nat. Commun.* **2014**, 5, 1–7.

(8) Lin, Y.; Shen, L.; Dai, J.; Deng, Y.; Wu, Y.; Bai, Y. π-Conjugated Lewis Base: efficient trap-passivation and charge extraction for hybrid perovskite solar cells. *Adv. Mater.* **2017**, *29*, 1604545.

(9) Chen, B.; Rudd, P. N.; Yang, S.; Yuan, Y.; Huang, J. Imperfections and their passivation in halide perovskite solar cells. *Chem. Soc. Rev* **2019**, 48(14), 3842–3867.

(10) Zhang, H.; Wu, Y.; Shen, C.; Li, E.; Yan, C.; Zhang, W. Efficient and stable chemical passivation on perovskite surface via bidentate anchoring. *Adv. Energy Mater.* **2019**, *9*, 1803573.

(11) Tavakoli, M. M.; Bi, D.; Pan, L.; Hagfeldt, A.; Zakeeruddin, S. M.; Grätzel, M. Adamantanes enhance the photovoltaic performance and operational stability of perovskite solar cells by effective mitigation of interfacial defect states. *Adv. Energy Mater.* **2018**, 8, 1800275.

(12) Ono, L. K.; Qi, Y. Surface and interface aspects of organometal halide perovskite materials and solar cells. *J. Phys. Chem.* **2016**, 7, 4764–4794.

(13) She, L.; Liu, M.; Zhong, D. Atomic structures of $CH_3NH_3PbI_3$ (001) surfaces. *ACS Nano* **2016**, 10, 1126–1131.

(14) Noel, N. K.; Abate, A.; Stranks, S. D.; Parrott, E. S.; Burlakov, V. M.; Goriely, A. Enhanced photoluminescence and solar cell performance via Lewis base passivation of organic–inorganic lead halide perovskites. *ACS Nano* **2014**, 8, 9815–9821.

(15) Zeng, Q.; Zhang, X.; Feng, X.; Lu, S.; Chen, Z.; Yong, X. Polymer-passivated inorganic cesium lead mixed-halide perovskites for stable and efficient solar cells with high open circuit voltage over 1.3 V. *Adv. Mater.* **2018**, 30, 1705393.

(16) Wang, F.; Geng, W.; Zhou, Y.; Fang, H. H.; Tong, C. J.; Loi, M. A. Phenylalkylamine passivation of organolead halide perovskites enabling high-efficiency and air stable photovoltaic cells. *Adv. Mater.* **2016**, 28, 9986–9992.

(17) Li, X.; Chen, C. C.; Cai, M.; Hua, X.; Xie, F.; Liu, X. Efficient passivation of hybrid perovskite solar cells using organic dyes with -COOH functional group. *Adv. Energy Mater.* **2018**, 8, 1800715.

(18) Cramer, R. E.; Chudyk, M. A. Studies of an acetylacetone complex of zinc perchlorate. *Inorganic chemistry* **1972**, 12, 1193–1195.

(19) Aromí, G.; Gamez, P.; Reedijk, J. Poly beta-diketones: prime ligands to generate supramolecular metalloclusters. *Coord. Chem. Rev.* **2008**, 252, 964–989.

(20) Garra, P.; Morlet-Savary, F.; Graff, B.; Dumur, F.; Monnier, V.; Dietlin, C. Metal Acetylacetonate-Bidentate Ligand Interaction (MABLI) as highly efficient free radical
generating systems for polymer synthesis. *Polym. Chem.* **2018**, 9, 1371–1378.

(21) Xie, L.; Hwang, H.; Kim, M.; Kim, K. Ternary solvent for $CH_3NH_3PbI_3$ perovskite films with uniform domain size. *Phys. Chem. Chem. Phys.* **2017**, 19, 1143–1150.

(22) Radicchi, E.; Mosconi, E.; Elisei, F.; Nunzi, F.; De Angelis, F. Understanding the solution chemistry of lead halide perovskites precursors. *ACS Appl. Energy Mater.* **2019**, *2*, 3400–3409.

(23) Niu, T.; Lu, J.; Munir, R.; Li, J.; Barrit, D.; Zhang, X. Stable high-performance perovskite solar cells via grain boundary passivation. *Adv. Mat.* **2018**, 30, 1706576.

(24) Huang, Z.; Hu, X.; Liu, C.; Tan, L.; Chen, Y. Nucleation and crystallization control via polyurethane to enhance the bendability of perovskite solar cells with excellent
device performance. *Adv. Funct. Mater.* **2017**, 27, 1703061.

(25) Gfroerer, T. theory, & instrumentation. Photoluminescence in analysis of surfaces and interfaces. *Chichester: John Wiley & Sons Ltd.* **2006**.

(26) Chaudhary, B.; Kulkarni, A.; Jena, A. K.; Ikegami, M.; Udagawa, Y.; Kunugita, H. Poly (4-Vinylpyridine)-Based interfacial passivation to enhance voltage and moisture stability of lead halide perovskite solar cells. *Chem.Sus.Chem.* **2017**, *10*, 2473–2479.

(27) Kayesh, M. E.; Chowdhury, T. H.; Matsuishi, K.; Kaneko, R.; Kazaoui, S.; Lee, J.-J. Enhanced photovoltaic performance of $FASnI_3$-based perovskite solar cells with hydrazinium chloride coadditive. *ACS Energy Lett.* **2018**, *3*, 1584–1589.

(28) Gharibzadeh, S.; Nejand, A.; Moshaii, A.; Mohammadian, N.; Alizadeh, A. H.; Mohammadpour, R. Two-step physical deposition of a compact CuI Hole-Transport layer and the formation of an interfacial species in perovskite solar cells. *Chem.sus.chem* **2016**, 9, 1929–1937.

(29) Liang, P. W.; Liao, C. Y.; Chueh, C.; Zuo, F.; Williams, S. T.; Xin, X. K. Additive enhanced crystallization of solution- processed perovskite for highly efficient planar-heterojunction solar cells. *Adv. Mate.* **2014**, 26, 3748–3754.

(30) Thakur, U.; Kwon, U.; Hasan, M. M.; Yin, W.; Kim, D.; Ha, N. Y. Investigation into the advantages of pure perovskite film without PbI_2 for high performance solar cell. *Sci. Rep.* **2016**, 6, 35994.

(31) Wu, T.; Wang, Y.; Li, X.; Wu, Y.; Meng, X.; Cui, D. Efficient defect passivation for perovskite solar cells

by controlling the electron density distribution of donor-π acceptor molecules. *Adv. Energy Mater.* **2019**, 9, 1803766.

(32) Li, H.; Li, Y.; Li, Y.; Shi, J.; Zhang, H.; Xu, X. Synergistic effect of caprolactam as lewis base and interface engineering for efficient and stable planar perovskite solar cells. *Nano Energy* **2017**, 42, 222–231.

(33) Zhuang, X.; Zhang, Y.; Zhang, J.; Chen, Y.; Zhu, Y. The roles of acetylacetone additives in enhancing perovskite solar cell performance. *Mater. Res. Express* **2018**, 6, 025512.

(34) Kamarudin, M. A.; Hirotani, D.; Wang, Z.; Hamada, K.; Nishimura, K.; Hayase, S. Suppression of charge carrier recombination in lead-free tin halide perovskite via Lewis base post-treatment. *J. Phys. Chem.* **2019**, 10, 5277–5283.

(35) Hou, X.; Huang, S.; Ou-Yang, W.; Pan, L.; Sun, Z.; Chen, X. Constructing efficient and stable perovskite solar cells via interconnecting perovskite grains. *ACS Appl. Mater. Interfaces* **2017**, 9, 35200–35208.

(36) Pazos-Outón, L. M.; Xiao, T. P.; Yablonovitch, E. Fundamental efficiency limit of lead iodide perovskite solar cells. *J. Phys. Chem.* **2018**, 9, 1703–1711.

(37) Sherkar, T.; Momblona, C. L.; Gil-Escrig, J.; Ávila, M. S.; Bolink, H. J.; Koster, L. Recombination in perovskite solar cells: significance of grain boundaries, interface traps, and defect ions. *ACS Energy Lett.* **2017**, 2, 1214.

(38) Habisreutinger, S. N.; Noel, N. K.; Snaith, H. Hysteresis index: A figure without merit for quantifying hysteresis in perovskite solar cells. *ACS Energy Lett.* **2018**, 3, 2472–2476.

(39) Wei, D.; Ma, F.; Wang, R.; Dou, S.; Cui, P.; Huang, H. Ion-Migration inhibition by the cation–π interaction in perovskite materials for efficient and stable perovskite solar cells. *Adv. Mat.* **2018**, 30, 1707583.

(40) Chen, J.; Ko, S.; Liu, L.; Sheng, Y.; Han, H.; Li, X. The effect of different alkyl chains on the photovoltaic performance of D–π–A porphyrin-sensitized solar cells. *New J. Chem.* **2015**, *39*, 3736–3746.

3.2 Diaminomaleonitrile Lewis base additive for push-pull electron extraction for efficient and stable tin-based perovskite solar cells

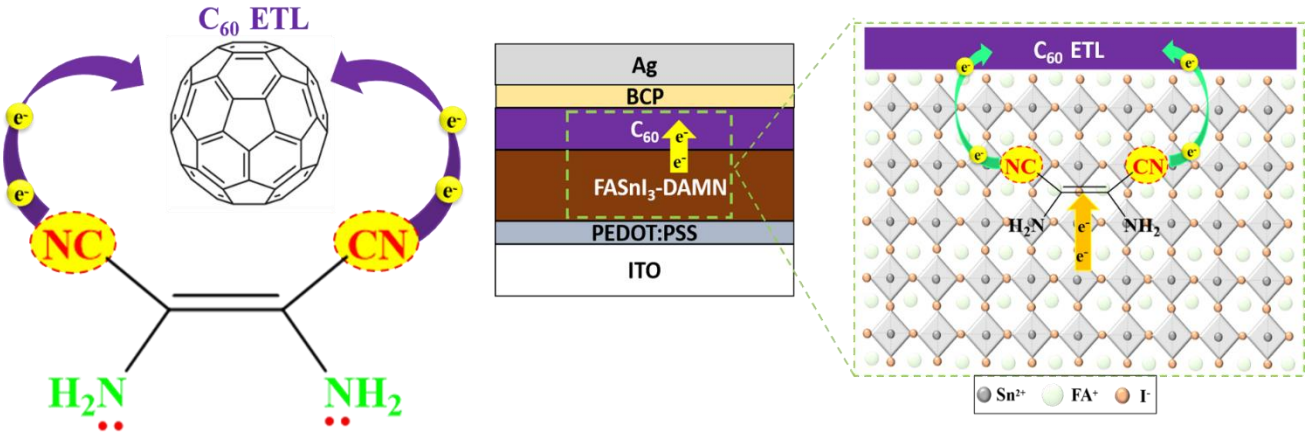

3.2.1 Diaminomaleonitrile Lewis base additive

In less than a decade, perovskite solar cells have increased their power conversion efficiency by 25.6%, making them one of the top candidates for the next generation of solar cells, and are now at the frontline competing against conventional Si solar cells. [1,2] However, commercialization and large-scale manufacture of Pb-based PSCs are hampered by Pb's toxicity and severe environmental consequences. [3] In the past few years, researchers have become interested in tin-based perovskite solar cells (Sn-PSCs) as a potential substitute for developing nontoxic PSCs. In addition to being less poisonous, Sn perovskite materials have better optoelectronic properties than Pb analogs, including a narrower band gap, lower exciton binding energy, and a smaller radius than Pb^{2+}. [2,4] With an ideal band gap of 1.1–1.4 eV, Sn-PSCs can possibly achieve a PCE of more than 33%. However, there are crucial issues with Sn-PSCs, such as the quick interaction between perovskite components in the precursor solution, which impacts the crystallinity and morphology of fabricated perovskite films. In addition, Sn^{2+} can be easily oxidized to Sn^{4+}, which forms Sn vacancies in the $FASnI_3$ absorber layer. [6] These critical drawbacks cause a high transportation loss of the photogenerated charge carriers and increase the recombination rate of Sn-PSCs compared to Pb-PSCs under solar illumination. [7,8] Lewis base additives were extensively introduced in Sn-PSC fabrication to reduce p-doping and improve the crystallinity of Sn perovskite materials. By utilizing their effective functional groups, Lewis base additives can work as a morphology controller, reducing agents, and/or antioxidants to improve the quality of the fabricated Sn-based perovskite film. [4, 9−13] For example, the introduction of SnF_2 as an additive in the Sn perovskite precursor solution reduced the Sn vacancies efficiently in the resultant Sn perovskite crystal lattice. [14] In another report, based on the hydrogen bonding interaction, Han et al. utilized poly(vinyl alcohol) (PVA) additive with SnF_2. The effective hydroxyl groups in PVA promoted the formation of a perovskite film with improved crystallinity and stabilized the perovskite crystal via hydrogen bonding as illustrated in **Figure 1a**. [15] Diau et al. reported the addition of ethylenediammonium diiodide ($EDAI_2$), which has bilateral ends as shown

in **Figure 1b**, to control the $FASnI_3$ film growth and passivate the surface defects of the $FASnI_3$ perovskite. [16] Although such inclusion of additives within the perovskite compounds could improve the respective Sn-PSC performances, the overall performance loss can be attributed to the faster recombination rate of the photogenerated electron−hole pairs. Additionally, efficient electron transportation from the Sn perovskite layer to the adjacent ETL has not been well explored in Sn-PSCs, which can be a challenging factor for achieving high photovoltaic performance. In this work DAMN Lewis base additive was used, which has two effective CN groups as electron-withdrawing units. The presence of two CN groups in DAMN can promote electron extraction from the perovskite layer, thereby facilitating efficient electron transfer from the perovskite layer to the adjacent ETL (fullerene (C_{60})) as illustrated in **Figure 1c**. The faster electron transfer from the perovskite layer to C_{60} can reduce the electron transport loss between these two layers, which can enhance V_{OC} and FF of the respective Sn-PSCs. Furthermore, the fast electron transfer can guarantee more electrons being transferred to the electrode, resulting in a higher J_{SC}. The two amino groups can interact with SnI_2 in the perovskite precursor, which can control the fast interaction in addition to reducing oxidation of Sn^{2+} to Sn^{4+}.

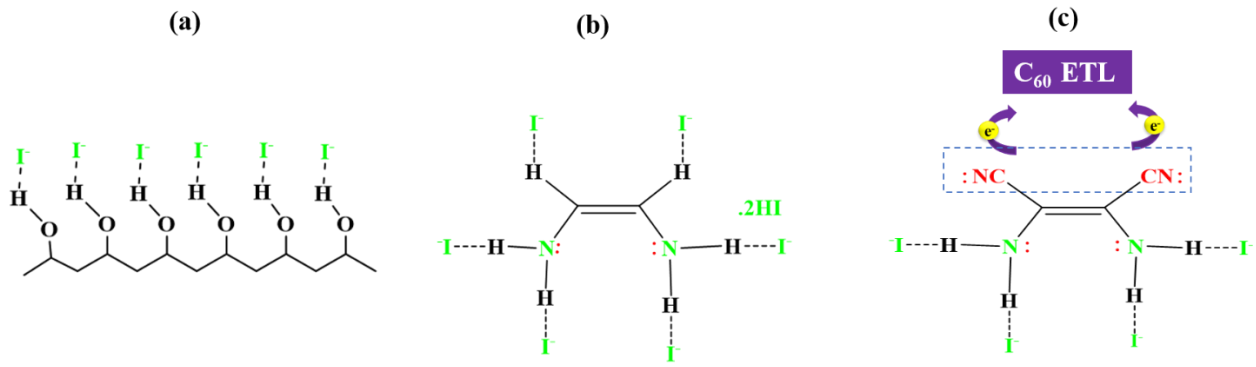

Figure 1. Chemical structure of Lewis base additives (a) poly(vinyl alcohol) (PVA), (b) ethylenediammonium diiodide ($EDAI_2$), and (c) diaminomaleonitrile (DAMN) with their proposed interaction mechanism using their active functional groups.

3.2.2 Interaction of diaminomaleonitrile with perovskite precursor

The DAMN Lewis base is an exciting compound with two electron-donating amino (NH_2) groups and two electron withdrawing CN groups. The two NH_2 groups can form hydrogen bonds with

iodide ions in the perovskite lattice. Hydrogen bonding can enhance the stability of the perovskite compound and passivate defects. [17,18] By adding DAMN to the $FASnI_3$ perovskite precursor solution, the hydrogen bonding interaction of DAMN with SnI_2 was observed using FTIR spectroscopy, as shown in **Figure 2a**. For SnI_2-DAMN, the stretching vibration of the NH group was shifted from 3198 to 3206 cm^{-1}, and for the NH_2 group, from 3341 to 3345 cm^{-1}, with increasing intensity of these peaks compared to DAMN, while for SnI_2, no peaks appeared in this region. These shifts with increased intensities explain the formation of hydrogen bonds between the hydrogen atoms in the amino group and the iodide anion in SnI_2. [15,19] Introducing hydrogen bonding can control the $FASnI_3$ film crystal growth and thus form a compact perovskite film. Besides, the H···I hydrogen bonding interactions can suppress iodide ion migration and stabilize the weak Sn−I bond, [20] which is vital for the long-term stability of the respective PSCs. Furthermore, we noticed a shift for the CN group of DAMN in the FTIR spectra from 2211 to 2213 cm^{-1}, and the peak became sharper after interaction with SnI_2, as shown in **Figure 2a, b**. This can be attributed to the donation of a lone pair of electrons from the nitrogen of the CN group in DAMN to the vacant orbital of the Sn element.[20] Moreover, the XRD analysis of SnI_2-DAMN adduct shows a decrease in the intensity of the main peak of SnI_2 with a noticeable shift in the peak position, which is ascribed to the interaction between SnI_2 and DAMN (see **Figure 2 c, d**).

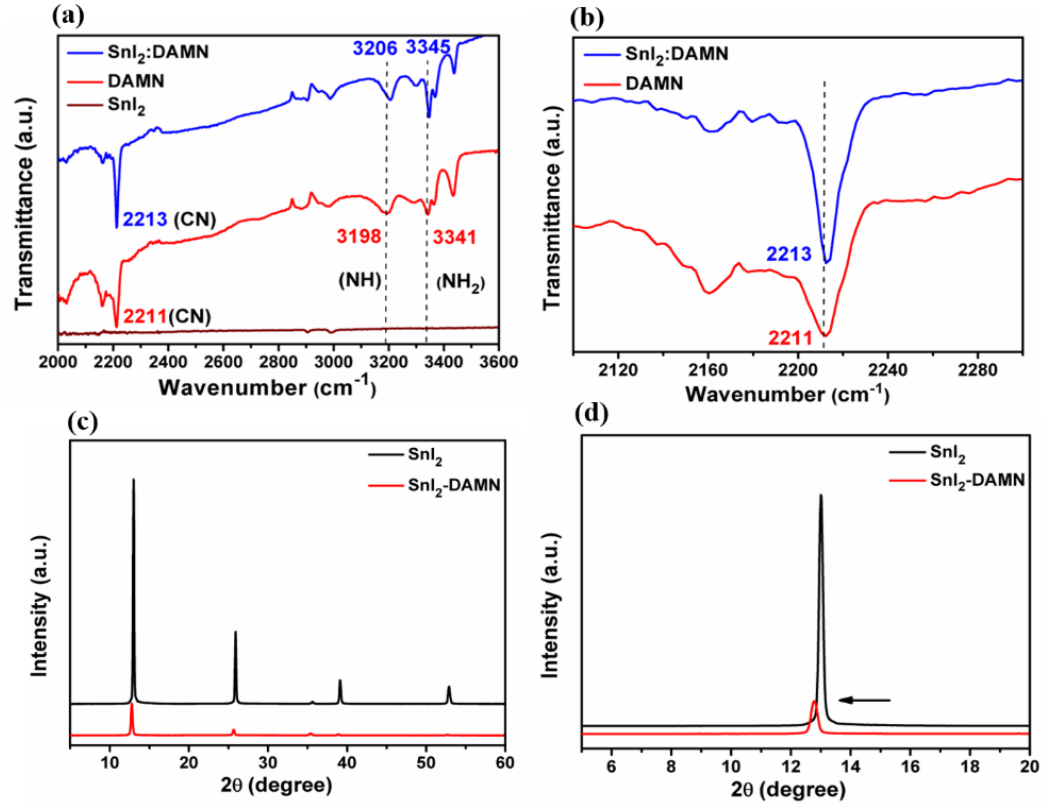

Figure 2. (a) FTIR spectra of SnI_2, DAMN, and SnI_2-DAMN Films. (b) Magnification of the FTIR spectra from the 2100 to 2300 cm^{-1} region for the DAMN and SnI_2-DAMN films. (c) The XRD for the SnI_2 compared to SnI2-DAMN, (d) Magnification of XRD for the SnI_2 compared to SnI_2-DAMN from 5° to 20°.

3.2.3 Crystallinity and lattice strain of perovskite films

To study the effect of DAMN on the crystal structure of $FASnI_3$, the XRD pattern of the pristine $FASnI_3$ film was compared with those of the $FASnI_3$-DAMN films. As shown in **Figure 3**, the XRD peaks of the fabricated films were mainly located at 13.96, 24.31, 28.15, 31.53, 40.17, and 42.79° which are assigned to (100), (102), (200), (122), (222), and (213) crystal planes of the orthorhombic $FASnI_3$ perovskite phase, respectively. [9] Interestingly, the modified $FASnI_3$-DAMN perovskite films showed a decrease in the FWHM compared to pristine $FASnI_3$ (see **Table 1**). The reduction in FWHM occurred in all angles with increased concentration of DAMN up to 3 mol %. This indicates better crystallinity across the $FASnI_3$ absorber layer after the inclusion of the DAMN additive. [21,22]

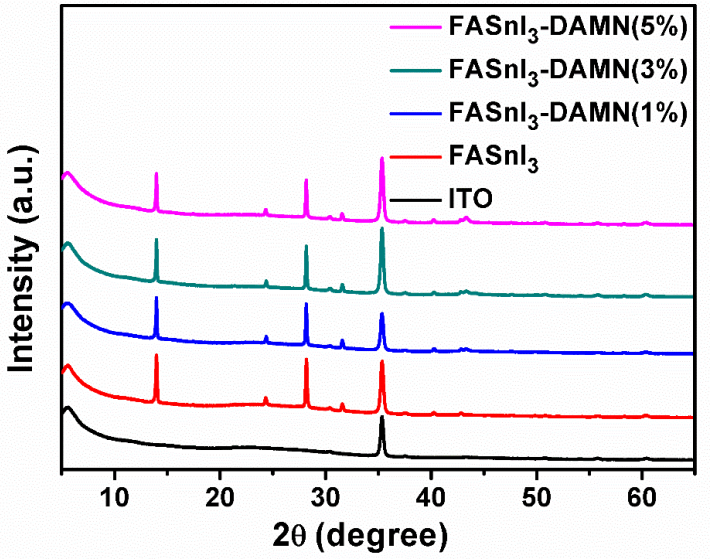

Figure 3. XRD patterns of $FASnI_3$ perovskite films with 0, 1, 3, and 5 mol % DAMN.

Table 1. The full width at half maximum (FWHM) of the XRD peaks of the $FASnI_3$ perovskite film with 0 mol%, 1 mol%, 3 mol% and 5 mol% of DAMN, respectively.

Perovskite film / 2 Theta (degree)	0% DAMN	1% DAMN	3% DAMN	5% DAMN
13.96°	0.1337°	0.0886°	0.0849°	0.0888°
24.31°	0.1615°	0.1312°	0.1208°	0.1412°
28.15°	0.137°	0.1093°	0.0995°	0.1063°
31.53°	0.1596°	0.1453°	0.1293°	0.1366°
40.17°	0.2091°	0.2179°	0.1617°	0.1894°
42.79°	0.269°	0.2395°	0.1532°	0.0981°

Importantly, it is known that the change in FWHM of the XRD peaks can affect the lattice strain, [23,24] which is a critical factor for the overall photovoltaic performance and stability of the PSCs.[25] The strain in PSCs contributes to the instability of these materials because it weakens bonds, favors the formation of defects, and lowers the activation energy for ion migration, thereby inducing the degradation of perovskites. [24,26,27] During Sn perovskite film fabrication, crystallization occurred very fast, which led to formation of a perovskite film with poor morphology, defects, and the perovskite lattice formed with strain. We calculated the lattice strain (ε) using the Halder− Wagner method for $FASnI_3$-DAMN films with varying concentrations of DAMN (**Figure 4**). The

Halder−Wagner equation (eq 1) has the form of a straight line, y = ax + b. We plot y = $(\beta/\tan\theta)^2$ against x = $\beta/(\tan\theta \sin\theta)$, where θ is in radians and β is the integral breadth (peak area/peak intensity) in radians. Then, the y-intercept of the resulting straight line affords $16\varepsilon^2$. Pristine $FASnI_3$ possesses a lattice strain of 0.29%, while on adding either 1, 3, or 5 mol % DAMN to $FASnI_3$, the lattice strain decreases to 0.23, 0.178, or 0.169%, respectively, as illustrated in **Figure 5**.

$$\left(\frac{\beta}{\tan\theta}\right)^2 = \frac{K\lambda}{D} \cdot \frac{\beta}{\tan\theta \sin\theta} + 16\varepsilon^2 \qquad (1)$$

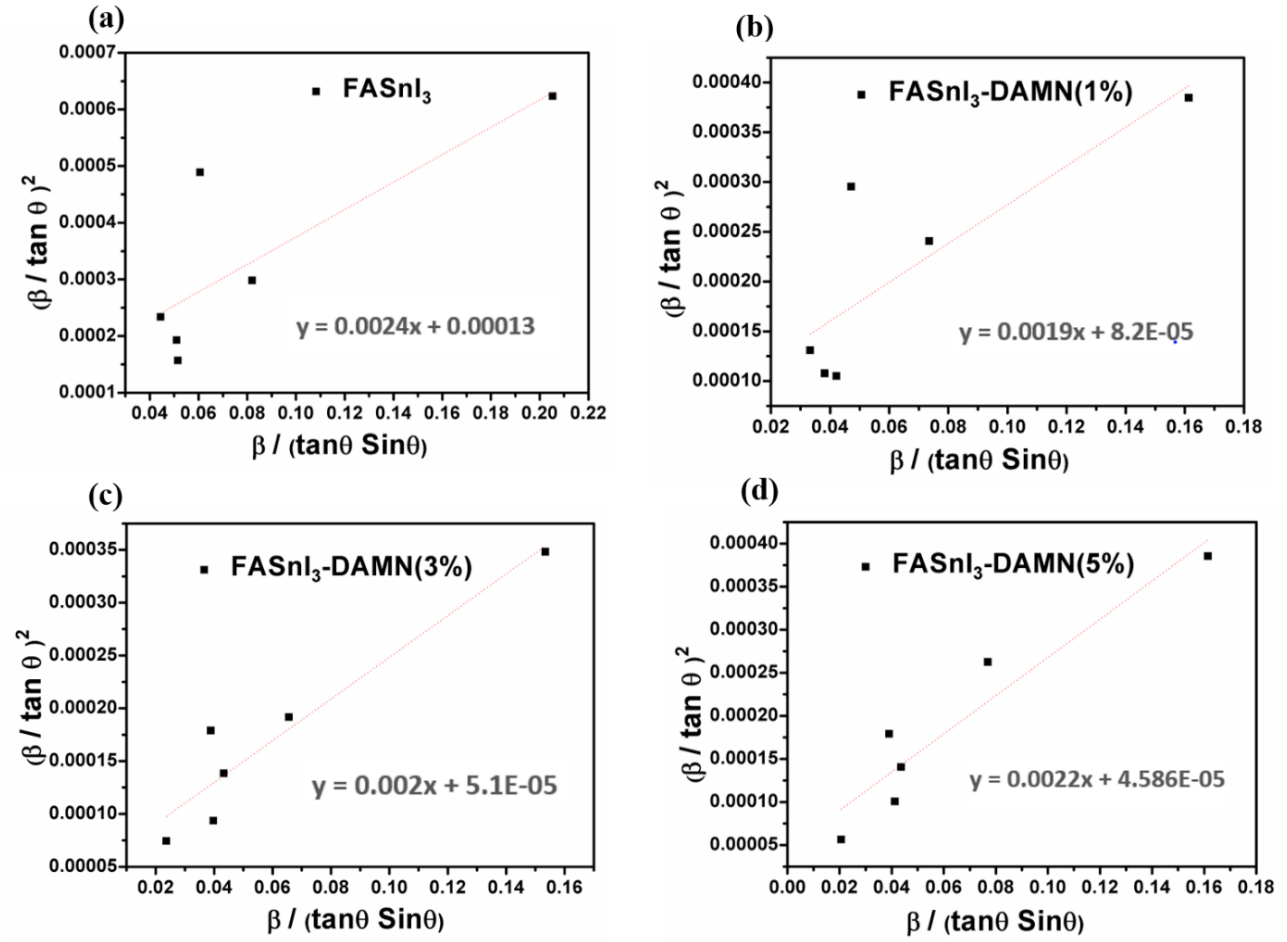

Figure 4. Halder–Wagner plots of the pristine $FASnI_3$ perovskite film with (a) 0 mol%, (b) 1 mol%, (c) 3 mol% and (d) 5 mol% of DAMN, respectively.

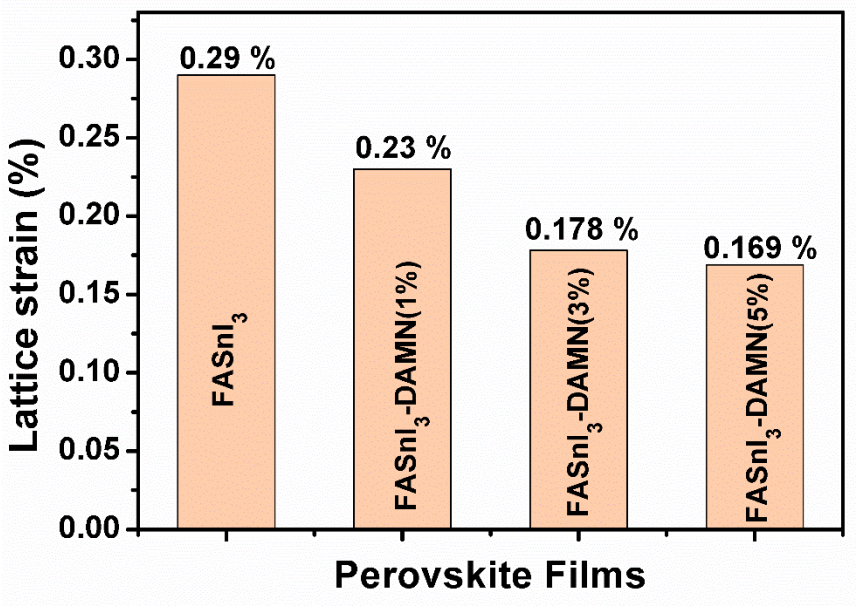

Figure 5. Change in lattice strain of the $FASnI_3$ perovskite with incorporation of DAMN.

Adding DAMN controls the crystal growth of the $FASnI_3$ perovskite due to hydrogen bonding with iodide ions and the interaction with Sn^{2+} of $FASnI_3$. This interaction improved the quality of the perovskite film, reduced the strain of the crystal lattice, decreased Sn^{2+} to Sn^{4+} oxidation, and enhanced stability. The reduction in the lattice strain of the $FASnI_3$ absorber layer after inclusion of the DAMN additive can improve the carrier mobility and carrier extraction and reduce recombination site ion migration, which can enhance the efficiency and stability of the respective PSCs. [28]

XPS was performed to explore the effect of DAMN on the $FASnI_3$-DAMN (3 mol %) film. For the $FASnI_3$-DAMN film, the ratio of Sn^{4+}/ Sn^{2+} decreased by 47% compared to pristine $FASnI_3$ (see **Figure 6 and Table 2**). This can be understood due to the presence of two amino groups in DAMN, which can minimize the oxidation of Sn^{2+} to Sn^{4+}. [29]

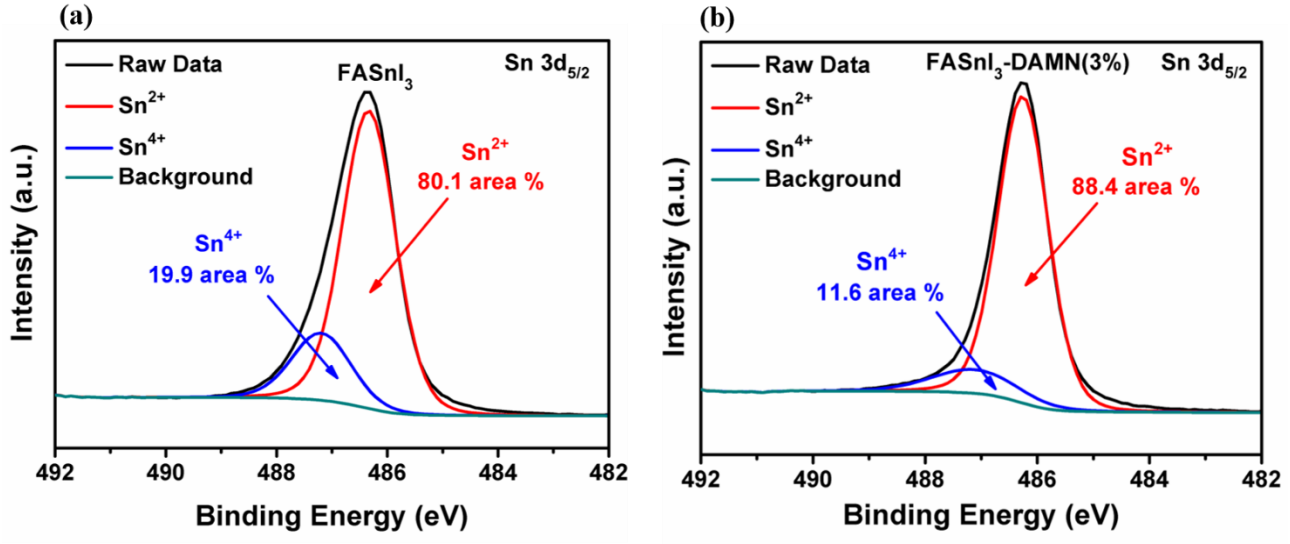

Figure 6. High-resolution X-ray photoelectron spectra of the $FASnI_3$ and $FASnI_3$-DAMN (3 mol %) films, respectively

Table 2. The area ratio of Sn^{2+} and Sn^{4+} in the XPS of the $FASnI_3$ and $FASnI_3$-DAMN(3mol%) perovskite films.

Samples	Sn^{2+}	Sn^{4+}
$FASnI_3$	80.1%	19.9%
$FASnI_3$-DAMN	88.4%	11.6%

Table 3. The area ratio of Sn:I in the XPS of the $FASnI_3$ and $FASnI_3$-DAMN(3mol%) perovskite films.

Sample	Sn:I ratio
$FASnI_3$	1:1.3
$FASnI_3$-DAMN	1:1.7

The ratio of Sn and I was calculated, and we found that the $FASnI_3$ perovskite suffers from a severe loss of I^-, which could be the cause of the instability and higher recombination rate of Sn-PSCs. As shown in **Table 3**, the Sn/I ratio for the $FASnI_3$ sample is 1:1.3 compared to 1:1.7 for $FASnI_3$-DAMN. This suggests that inclusion of DAMN stabilizes the iodide in the perovskite crystal through hydrogen bonding. Consequently, iodide ion migration reduces and the stability of $FASnI_3$-DAMN might be enhanced by decreasing the recombination rate.

3.2.4 Morphology of the perovskite films

Figure **7a–d** shows the surface morphology of the fabricated perovskite films using SEM. The pristine $FASnI_3$ film showed a small grain size with cracks. On adding 1 and 3 mol % DAMN, the

grain size became bigger with compact morphology and no cracks at the grain boundary. The grain size distribution of the perovskite films in **Figure 8** showed higher distribution for the larger grain size after inclusion of 1 and 3 mol % DAMN compared to the pristine $FASnI_3$. Furthermore, the crystalline size calculated using the Scherrer equation showed an increase after inclusion of DAMN up to 3 mol % as shown in **Table 4**. SEM images revealed that using DAMN improved the quality of the perovskite film, which is important for enhancing photovoltaic performance. However, a higher concentration of DAMN (5 mol %) forms a blocking layer on top of the perovskite film, as shown in **Figure 7d**. From the XRD and SEM results, we noticed improved crystallinity and morphology with strain reduction of the $FASnI_3$ film on inclusion of DAMN up to 3 mol %.

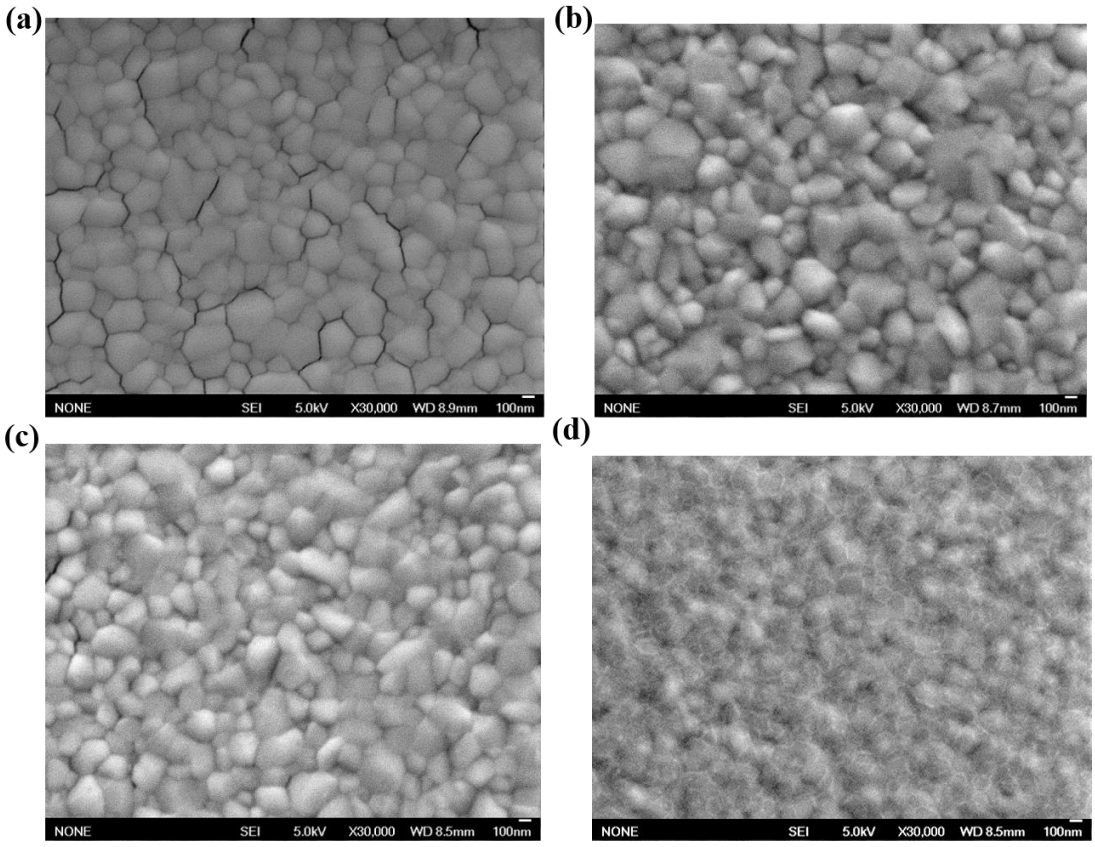

Figure 7. SEM images of the $FASnI_3$ perovskite film with (a) 0 mol %, (b) 1 mol %, (c) 3 mol %, and (d) 5 mol % DAMN.

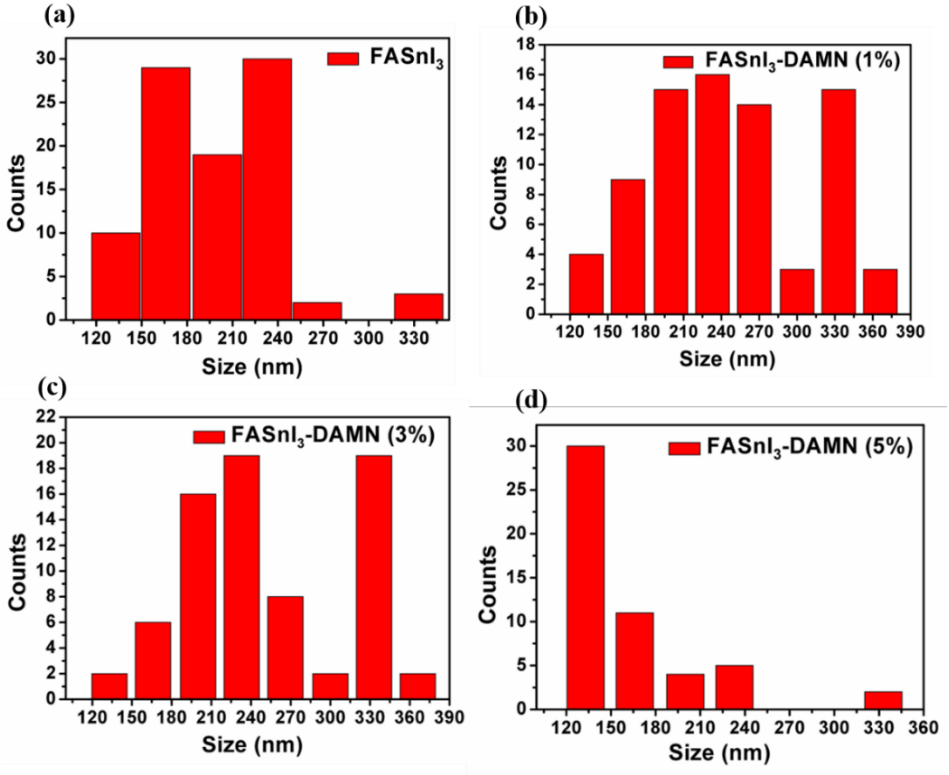

Figure 8. The graine size distribution of $FASnI_3$ perovskite film with (a) 0 mol%, (b) 1 mol%, (c) 3 mol% and (d) 5 mol% of DAMN, respectively.

Table 4. The crystalline size (nm) calculated from the XRD peaks of the $FASnI_3$ perovskite film with 0 mol%, 1 mol%, 3 mol% and 5 mol% of DAMN, respectively.

Perovskite film / 2 Theta (degree)	0% DAMN	1% DAMN	3% DAMN	5% DAMN
13.96°	59.862	90.334	94.270	90.130
24.31°	50.3187	61.939	67.272	57.552
28.15°	59.782	74.932	82.313	77.047
31.53°	51.721	56.812	63.842	60.430
40.17°	40.452	38.819	52.311	44.660
42.79°	31.718	35.625	55.693	86.975

3.2.5 Photophysical properties of perovskite films

The UV−visible absorption spectra of the perovskite films show a slight blue shift at the band edge 800−860 nm after addition of DAMN as shown in **Figure 9 a**. This indicates a slight change in the band gap of $FASnI_3$ after inclusion of DAMN (**Figure 9 b**).

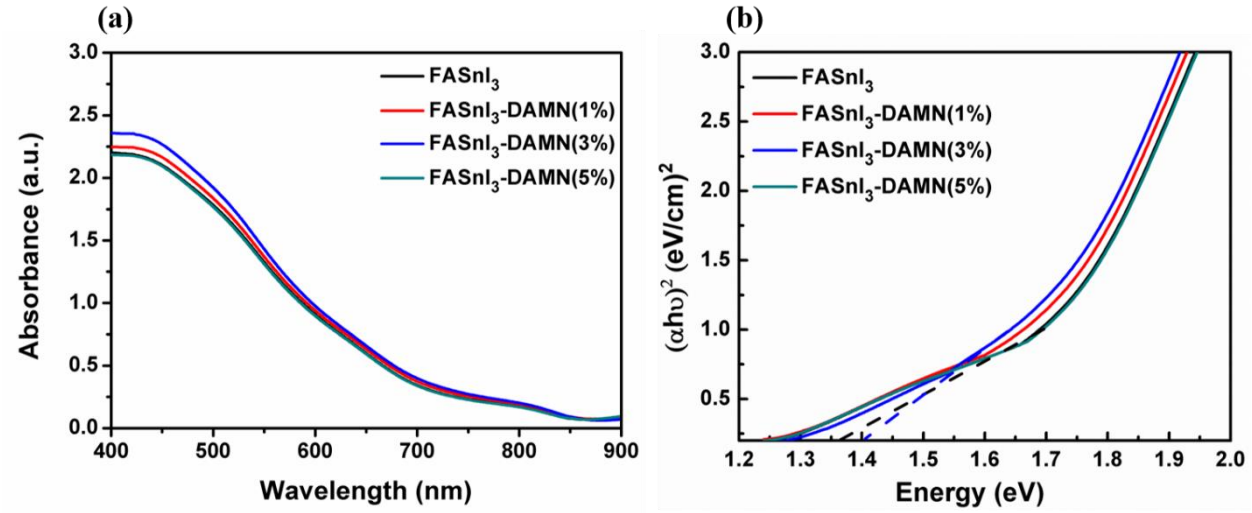

Figure 9. (a) The UV-visible spectra and (b) Tauc plot of $FASnI_3$ films with and without DAMN.

Furthermore, the photoluminescence (PL) spectrum shows the emission peak of pristine FASnI3 at ~860 nm. On adding DAMN to $FASnI_3$, the emission peak was blue-shifted and the blue shift increased with an increasing concentration of DMAN (**Figure 10 a**). We estimated the conduction band values of the perovskite films from the bandgap values and the valence band values obtained using an AC- 3E photoelectron spectrometer (**Figure 11**). Then, from the valence and conduction band values, we constructed an energy band diagram, shown in **Figure 12**.

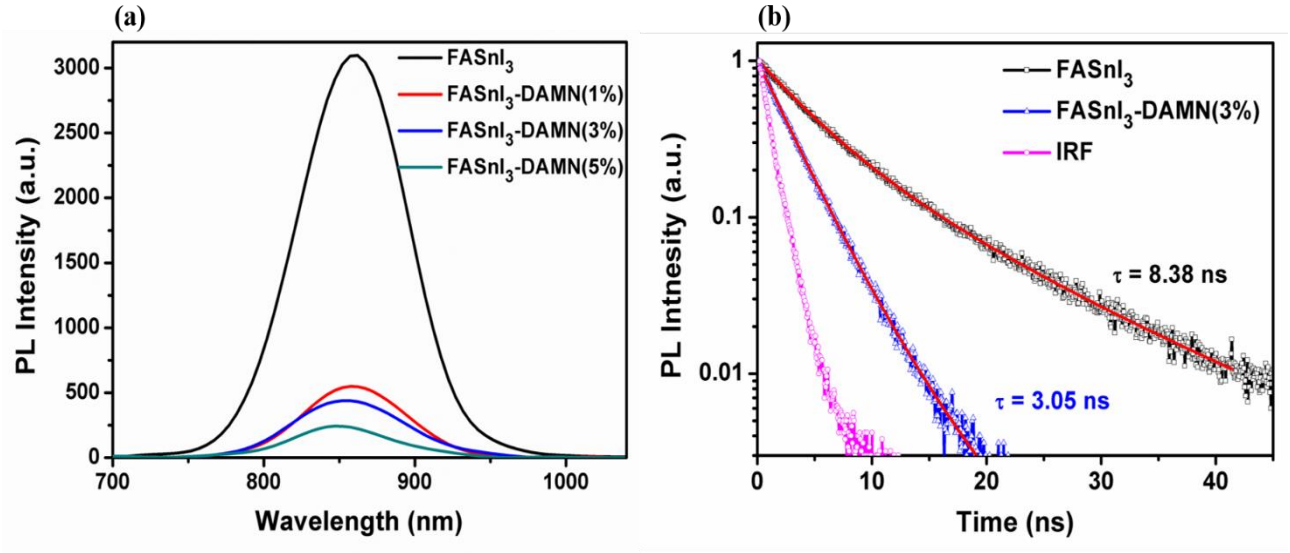

Figure 10. (a) Steady-state PL spectra of $FASnI_3$ perovskite films fabricated with 0, 1, 3, and 5 mol % DAMN prepared on glass substrates. (b) Normalized time-resolved photoluminescence spectra (TRPL) of the $FASnI_3$ and $FASnI_3$-DAMN (3mol%) perovskite films prepared on the glass substrate.

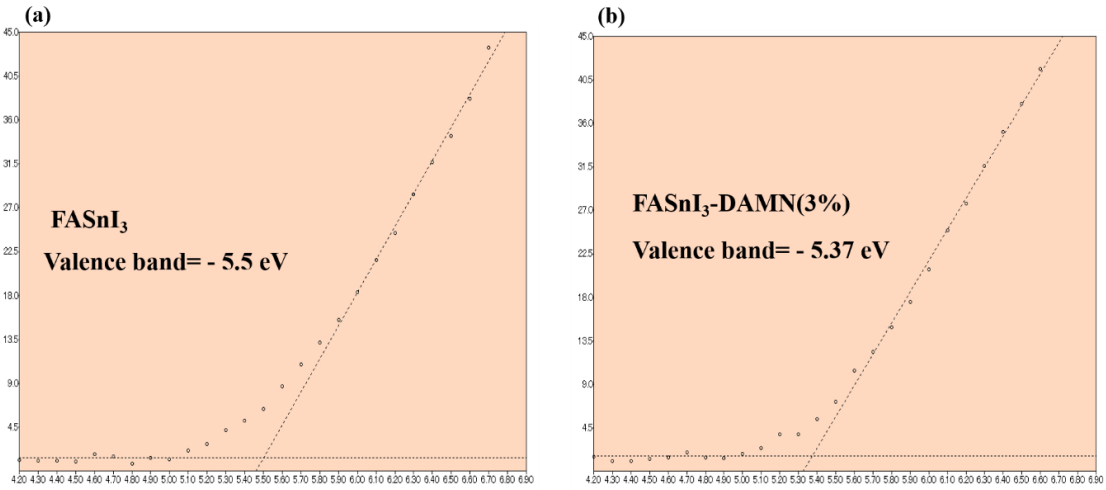

Figure 11. The photoelectron emission spectra of the perovskite films (a) $FASnI_3$ and (b) $FASnI_3$-DAMN(3%).

The conduction band of the $FASnI_3$-DAMN (3%) perovskite film tends to be shallower than that of the pristine $FASnI_3$, which is well-matched with the conduction band of C_{60}. Furthermore, the valence band of the $FASnI_3$-DAMN (3%) perovskite film becomes more matched with the work function of the PEDOT:PSS. The improved energy level alignment is expected to enhance the carrier transfer at both interfaces of perovskite/PEDOT:PSS and perovskite/C_{60}, which can increase the photovoltaic performance of PSCs.[4]

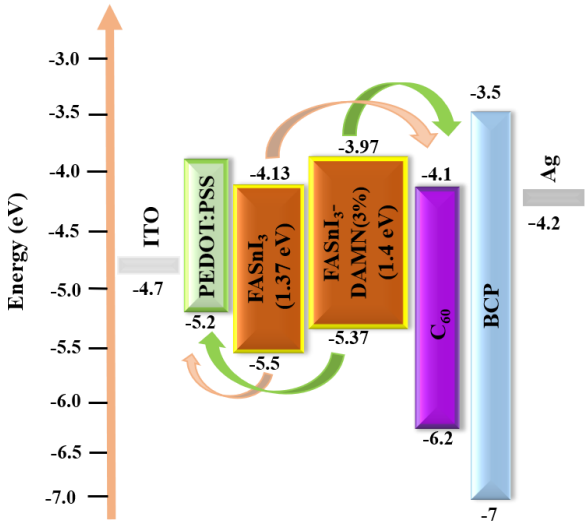

Figure 12. Schematic energy level diagram of the inverted planar PSCs of $FASnI_3$ compared to $FASnI_3$-DAMN(3mol%).

To understand the effect of DAMN on the electron transfer properties of the perovskite layer, we obtained the PL spectra of the $FASnI_3$-DAMN perovskite films and compared them with that of

$FASnI_3$. Using DAMN within the perovskite layer leads to stronger quenching, which increased with increasing DAMN concentration as shown in **Figure 10 a**. We further analyzed the charge transfer kinetics through the TRPL measurements (**Figure 10 b**). The TRPL showed that the decay lifetime was decreased to 3.05 ns after using FASnI3-DAMN (3 mol %) as compared to 8.38 ns for pristine $FASnI_3$. Both PL and TRPL data suggest that a more efficient electron extraction is possible when the $FASnI_3$ perovskite is doped with an optimal amount of DAMN (3 mol %). This behavior is due to the electron-withdrawing ability of the CN groups in DAMN. Based on these findings, we can predict an increase in electron mobility for $FASnI_3$- DAMN-based PSCs due to the efficient electron extraction from the perovskite layer.

3.2.6 Electron mobility and trap-state density of electron-only devices

The changes in electron mobility and electron trap-state density of the $FASnI_3$ perovskite films after inclusion of DAMN were evaluated by dark *J*–*V* analysis for electron-only devices (FTO/TiO_2/ $FASnI_3$ (with and without DAMN)/C_{60}/Ag) as shown in **Figure 13**. The low bias voltage plot shows a linear relation, indicating an ohmic-contact response, while the current increases sharply at higher bias voltage, indicating that the trap states are fully filled.[30] The electron mobility (μ) for the $FASnI_3$-DAMN and $FASnI_3$-based PSSCs is calculated using eq 2:

$$J = 9\varepsilon_r\varepsilon_0\mu V^2/8L^3 \qquad (2)$$

Where ε_0 is the absolute dielectric constant of vacuum (8.85×10^{-14} F·cm^{-1}), ε_r is the relative dielectric constant of $FASnI_3$ (5.7), μ is the electron mobility, L is the thickness of the perovskite film (∼180 nm), and *J* and *V* are the current and voltage of the electron-only device, respectively. [30,31] The electron-only device based on $FASnI_3$-DAMN showed electron mobility of 1.25×10^{-3} cm^2 V^{-1} s^{-1}, which is an order faster than that of the pristine $FASnI_3$-based electron-only device (8.79×10^{-4} cm^2 V^{-1} s^{-1}). The experimentally improved electron mobility after using the DAMN additive can be attributed to enhanced electron extraction from the perovskite film and reduction in the perovskite lattice strain by inclusion of DAMN. This enhancement in electron mobility is expected to increase

the J_{SC} of the PSCs. [32]

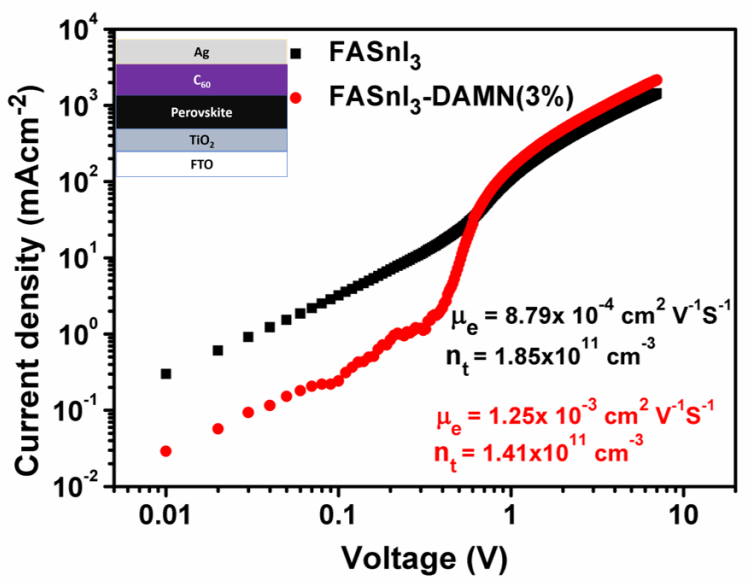

Figure 13. The dark *J–V* curves of the electron-only devices fabricated with $FASnI_3$ and $FASnI_3$-DAMN (3%).

Furthermore, we calculated the trap density of the fabricated electron-only devices using the space-charge limited current (SCLC) analysis. Equation 3 was used in the calculations of trap density.

$$V_{TFL} = en_tL^2/2\varepsilon_r\varepsilon_0 \qquad (3)$$

Here, V_{TFL} is the voltage at which all of the traps are filled, n_t is the trap-state density, and e is the elementary charge of the electron. Based on equation 3, a lower trap-state density of the materials results in a lower V_{TFL}. The electron-only devices based on $FASnI_3$-DAMN have a much lower V_{TFL} than the device based on pristine $FASnI_3$. The calculated trap-state density of the $FASnI_3$ and $FASnI_3$-DAMN films are 1.85×10^{11} and 1.41×10^{11} cm^{-3}, respectively. These results suggest that using DAMN additive increased the electron mobility and reduced the number of intrinsic traps in the $FASnI_3$ perovskite film, which is expected to improve the photovoltaic parameters of the modified PSCs. [25]

To further elucidate the role of DAMN in the electron transfer from the $FASnI_3$ perovskite to the C_{60} layer, the PL of the perovskite films $FASnI_3$-DAMN and $FASnI_3$ with the C_{60} layer was measured. DAMN induced stronger quenching as observed from the PL intensity and the decay lifetime was decreased from 6.7 ns ($FASnI_3$) to 2.31 ns ($FASnI_3$-DAMN) due to the electron extraction

from the perovskite layer as shown in **Figure 14 a, b**. DAMN extracted electrons from the perovskite layer (pull effect) and transfer them to C_{60} (push effect). The successful electron extraction from the perovskite layer was enhanced by the CN electron-withdrawing group in DAMN, while the electron transfer from the perovskite layer to C_{60} was promoted by the good matching of energy levels between the $FASnI_3$-DAMN and the C_{60} layer, as shown in **Figure 12**, in addition to the ability of C_{60} to accept electrons because it is an electron-transport layer. All of these factors improved the overall electron transfer between the perovskite layer and C_{60}, which led to higher electron mobility at the C_{60}/ perovskite interface. The push−pull effect of the DAMN molecule facilitates faster electron transfer from the $FASnI_3$ layer to C_{60}; therefore, better device performance can be expected. Based on the obtained results, we depicted the interaction mechanism of DAMN with the perovskite film, as shown in **Figure 14 c**. The DAMN molecule has two strong electron-withdrawing groups (CN), which extracted the electrons efficiently from the perovskite layer. Consequently, the electron mobility increased and electron transportation became faster through the perovskite/C_{60} interface. Furthermore, the amino groups in DAMN stabilized the perovskite lattice through hydrogen bonding with iodide ions.

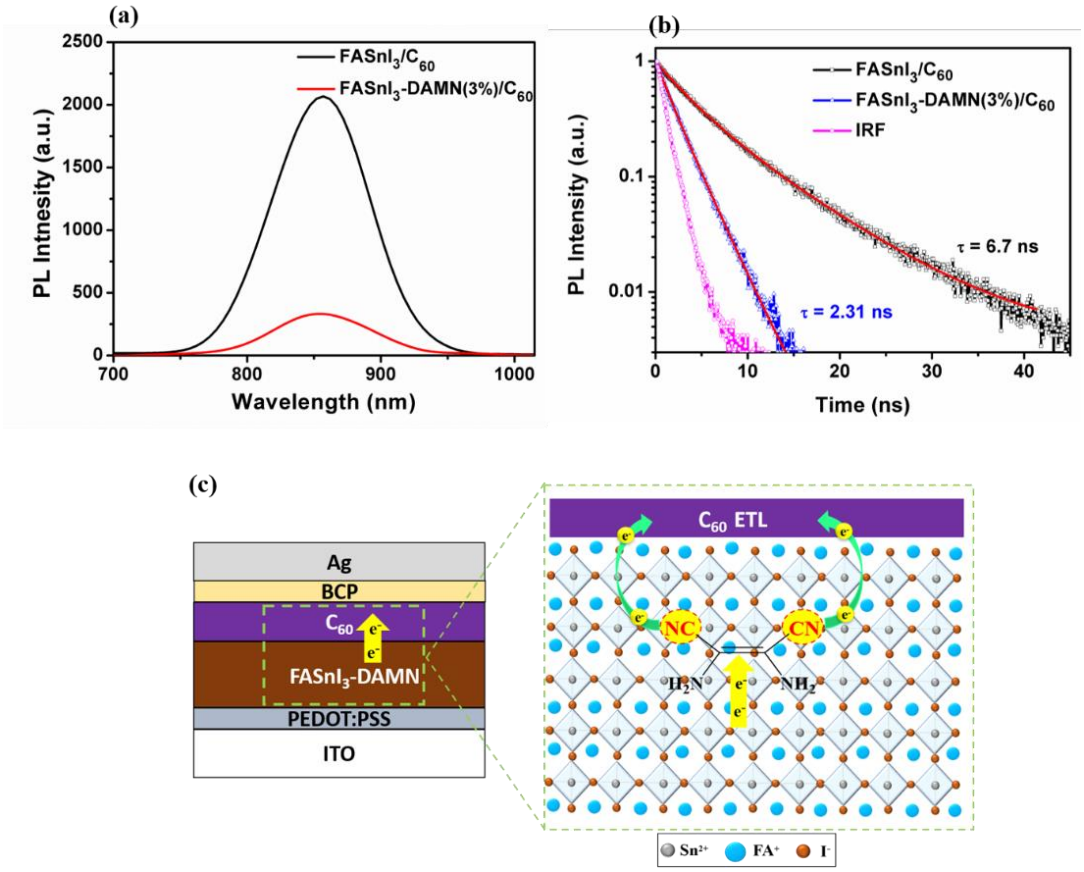

Figure 14. (a) Steady-state PL spectra and (b) normalized time-resolved photoluminescence (TRPL) spectra of the FASnI3/C60 and FASnI3- DAMN (3 mol %)/C60 films prepared on glass substrates. (c) Graphical illustration of DAMN interaction with the FASnI3 perovskite film.

3.2.7 The photovoltaic performance

To investigate the effect of DAMN on the photovoltaic performance of PSCs, the inverted planar PSCs with configuration ITO/PEDOT:PSS/$FASnI_3$/C_{60}/BCP/Ag was fabricated. The cross-sectional SEM images for the fabricated PSCs based on $FASnI_3$ and FASnI3-DAMN (3%) are shown in Figure 15. The cross-sectional images demonstrate formation of $FASnI_3$- DAMN perovskite with larger grain size and better morphology in addition to PSC layers being well connected together compared to the $FASnI_3$-based PSCs.

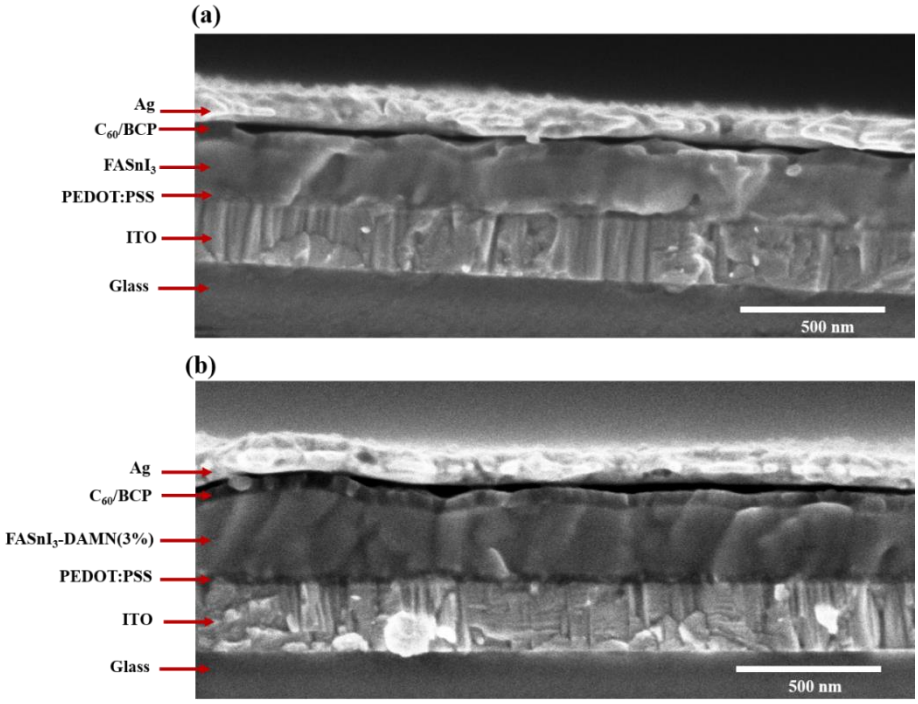

Figure 15. The cross-sectional SEM images of (a) $FASnI_3$ and (b) $FASnI_3$-DAMN(3%) based PSCs.

The IPCE of the fabricated PSCs is given in **Figure 16 a**. As shown, the incorporation of DAMN up to 3 mol % enhanced the photogenerated current of the modified PSCs. The $J-V$ curves of the fabricated PSCs were measured under 1 sun illumination conditions at 100 mW cm^{-2}. The $J-V$ curve of pristine $FASnI_3$ compared to those of $FASnI_3$-DAMN is shown in **Figure 16 b**. The $FASnI_3$-DAMNbased PSCs with 3 mol % DAMN showed J_{SC} of 16.62 mA cm^{-2}, V_{OC} of 0.654 V, and FF of 0.745, yielding a PCE of 8.11%. In contrast, the $FASnI_3$-based PSCs showed a PCE of 6.56% with lower J_{SC} and V_{OC} values of 14.857 mA cm^{-2} and 0.608 V, respectively. Further, 1 mol % DAMN gives a higher PCE of 6.98% compared to $FASnI_3$, while the 5 mol % DAMN shows a lower PCE of 5.88% compared to $FASnI_3$. The detailed PSC parameters are summarized in **Table 5**.

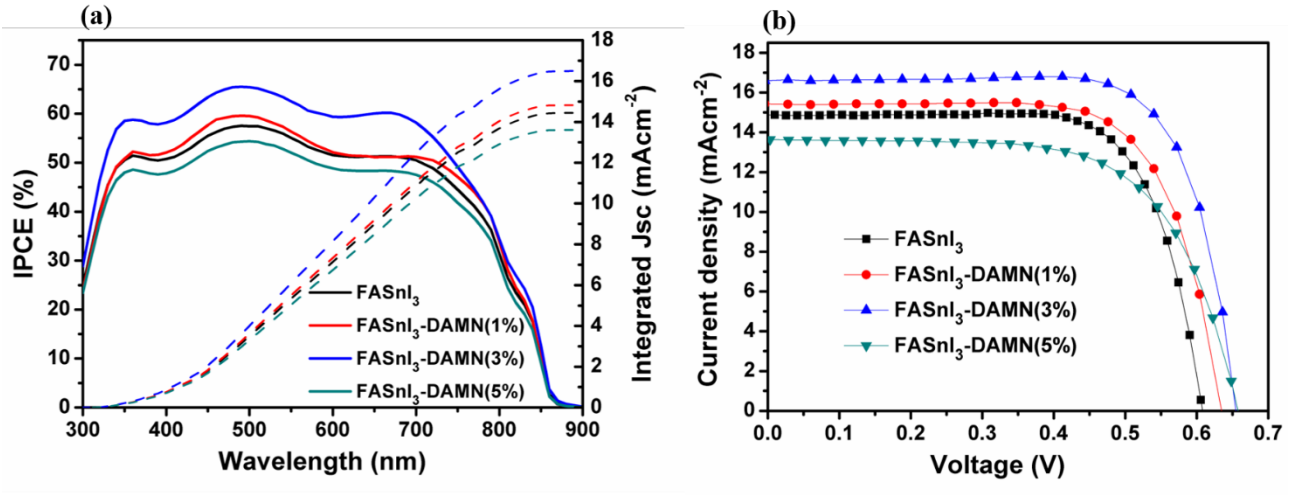

Figure 16. (a) IPCE and (b) the J−V curves of the FASnI3-based PSCs with 0, 1, 3, and 5 mol % DAMN, respectively.

Table 5. The Photovoltaic parameters of the fabricated $FASnI_3$ based PSCs with 0 mol%, 1 mol%, 3 mol% and 5 mol% of DAMN additive.

Device	J_{SC} (mAcm^{-2})	V_{OC} (V)	FF	PCE (%)
$FASnI_3$	14.857	0.608	0.726	6.56
$FASnI_3$-DAMN (1mol%)	15.392	0.635	0.714	6.98
$FASnI_3$-DAMN (3mol%)	16.622	0.654	0.745	8.11
$FASnI_3$-DAMN (5mol%)	13.640	0.658	0.656	5.88

Sn-PSCs were measured under simulated AM 1.5G illumination (25°C, relative humidity ~35%)

The photovoltaic results show that adding 1 and 3 mol % DAMN to FASnI3 boosted the J_{SC} of the PSCs due to the improved electron extraction from the $FASnI_3$ film and the transportation to the C_{60} ETL. This efficient electron transfer reduced the recombination rate of the generated electrons and holes, which increased the V_{OC} of the $FASnI_3$-DAMN modified PSCs compared to that of pristine $FASnI_3$. Moreover, in the XRD discussion section, we showed that using the DAMN additive reduced

the lattice strain, which had a good impact on improving the optoelectronic properties of the modified PSCs. Based on the obtained photovoltaic results, we observe that using a lower concentration of DAMN (1 and 3 mol %) is better for obtaining an enhanced photovoltaic performance. A higher concentration of DAMN (5 mol %) can form a blocking layer between the perovskite layer and C_{60} as we noticed in the SEM image shown in **Figure 7d**, which can suppress the electron transfer process. Interestingly, the photovoltaic parameters of the fabricated PSCs showed good reproducibility, as shown in **Figure 17**, and the PSCs based on DAMN (3 mol %) gave the best average performance.

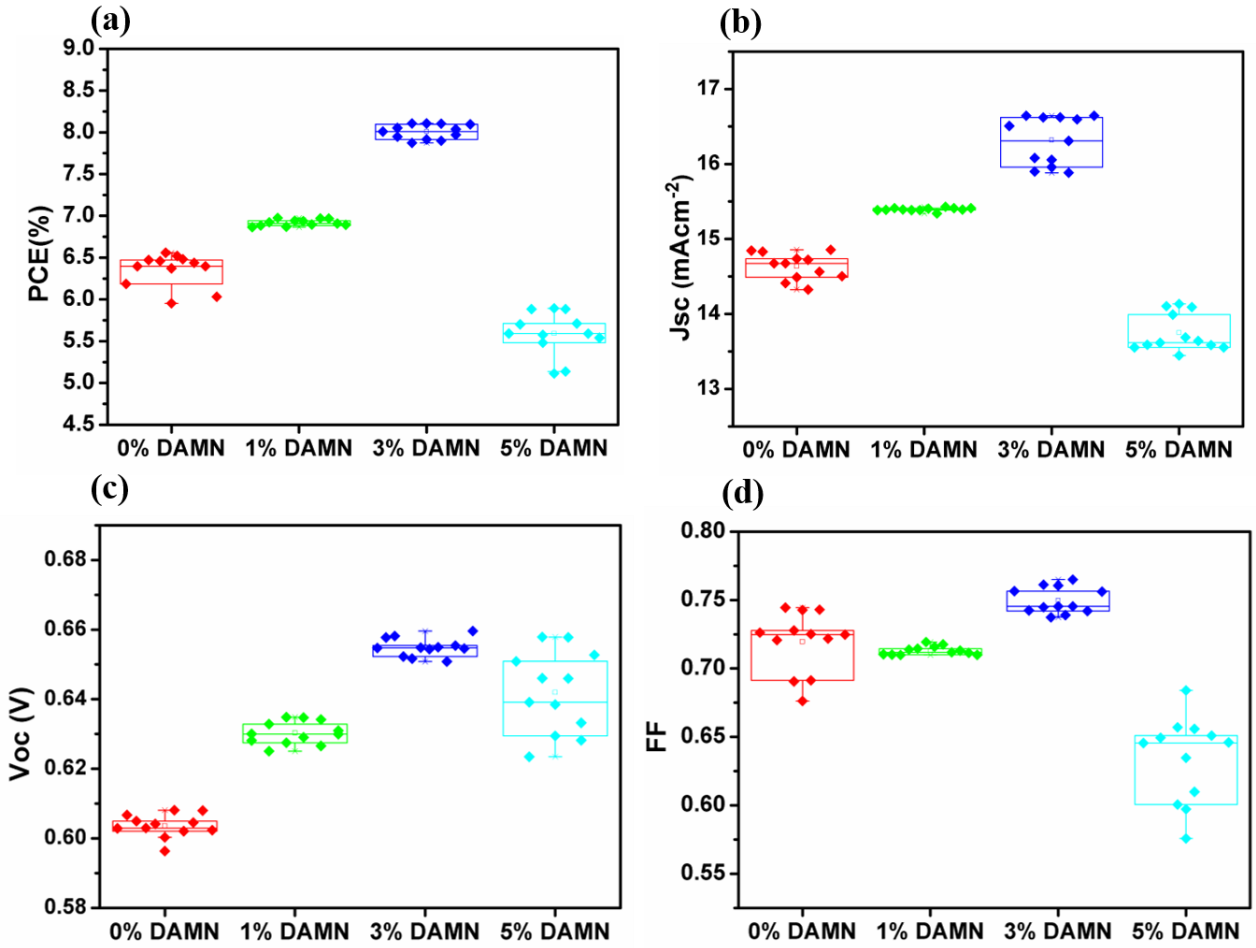

Figure 17. The statistical distribution of the (a) PCE, (b) Jsc, (c) Voc, (d) FF of the $FASnI_3$ based PSCs with 0 mol%, 1 mol%, 3 mol% and 5 mol% of DAMN, respectively.

3.2.8 Carriers transportation and recombination

To obtain deeper knowledge on the effect of DAMN on the electron transportation process across the fabricated PSCs, the transient photocurrent decay for the pristine and modified PSCs was

measured. As seen from **Figure 18 a**, the $FASnI_3$-DAMNbased PSCs showed a faster transient photocurrent decay lifetime (τ_t) of 1.29 μs as compared to the pristine $FASnI_3$ (3.59 μs), which indicates improved electron transportation after using DAMN. Importantly, these data are consistent with PL and TRPL results in addition to the reduction in the lattice strain observed from XRD. Furthermore, to clarify the change in the carrier recombination process after the inclusion of the DAMN additive, we conducted a transient photovoltage decay analysis, which can provide information about the recombination process. [33] A faster photovoltage decay indicates rapid recombination. [34] As seen from **Figure 18 b**, the recombination lifetime (τ_r) of the PSC fabricated with $FASnI_3$-DAMN (3 mol %) was delayed to 4.28 μs as compared to 2.4 μs of pristine $FASnI_3$, which indicates a slower recombination rate.

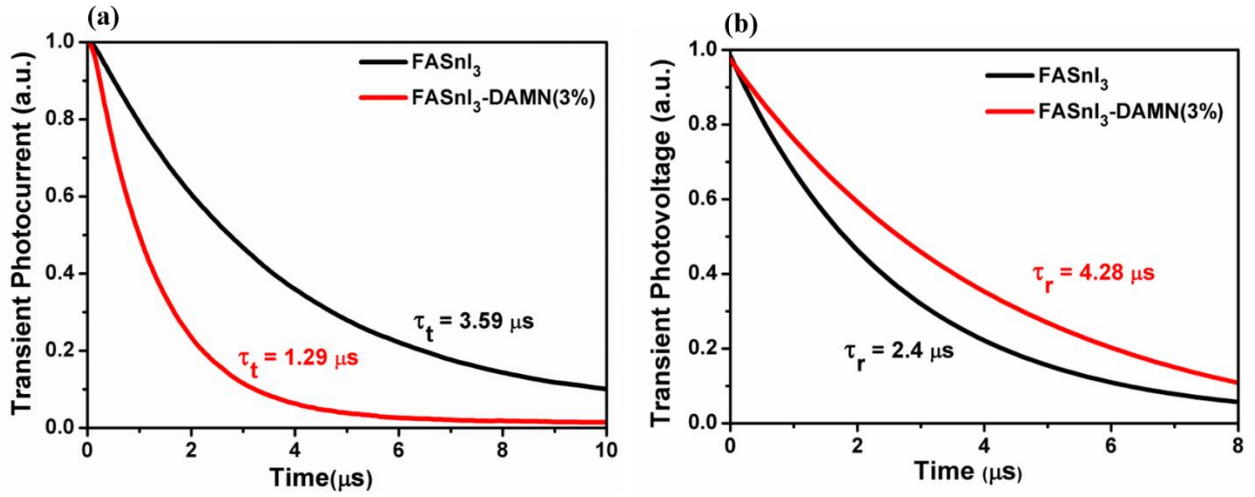

Figure 18. (a) Transient photocurrent decay and (b) transient photovoltage decay of the $FASnI_3$- compared to $FASnI_3$-DAMN (3 mol %)-based PSCs.

The charge recombination of the PSCs was also examined using EIS. The corresponding Nyquist plots were obtained with/without DAMN. As shown in **Figure 19 a**, a larger semicircle was obtained for $FASnI_3$-DAMN-based PSCs compared to $FASnI_3$, indicating higher resistance to recombination. The lower recombination rate can be explained due to the presence of DAMN, which guarantees efficient electron extraction from the $FASnI_3$ layer and faster transfer to the adjacent C_{60}. To further reveal the recombination dynamics in the respective PSCs, the dark $J-V$ curves of the

pristine and modified PSCs was measured as shown in **Figure 19 b**. The PSC based on the DAMN additive exhibited a relatively lower leakage current density ($J_0 = 4.35 \times 10^{-6}$ mA cm^{-2}) than that of the pristine FASnI3 one ($J_0 = 7.66 \times 10^{-5}$ mA cm^{-2}), associated with less charge recombination in the respective PSCs. These results are consistent with the reduction in recombination rate and indicate an efficient collection of photogenerated carriers. The above results unambiguously show the improvement in the electron transportation dynamics and thus the device performance after inclusion of DAMN.

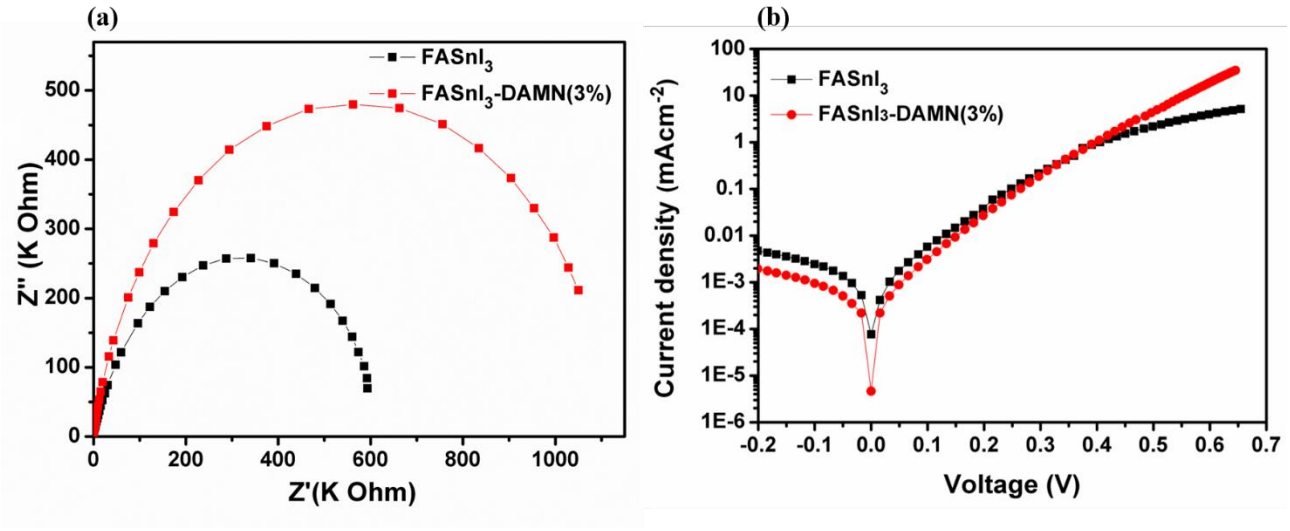

Figure 19. (a) Nyquist plot, and (b) dark J−V curves of the $FASnI_3$ compared to $FASnI_3$-DAMN (3 mol %) based PSCs.

3.2.9 Stability of PSCs

The effect of the shelf-life stability inside the N_2 glovebox on the performance of the fabricated PSCs was examined, as shown in **Figure 20 a**. The pristine $FASnI_3$-based PSCs started to degrade after 200 h, while the $FASnI_3$-DAMNbased PSCs showed better stability for over 1400 h. Most importantly, superior operational stability was observed for the $FASnI_3$-DAMN-based PSCs (**Figure 20 b**). The PCE was almost stabilized for over 300 h under continuous light illumination at maximum power point tracking (MPPT) conditions. The improved stability under MPPT conditions can be explained based on reduction of the lattice strain using DAMN in the $FASnI_3$ perovskite layer in addition to the hydrogen bonding, which stabilized the iodide ions in the perovskite lattice.

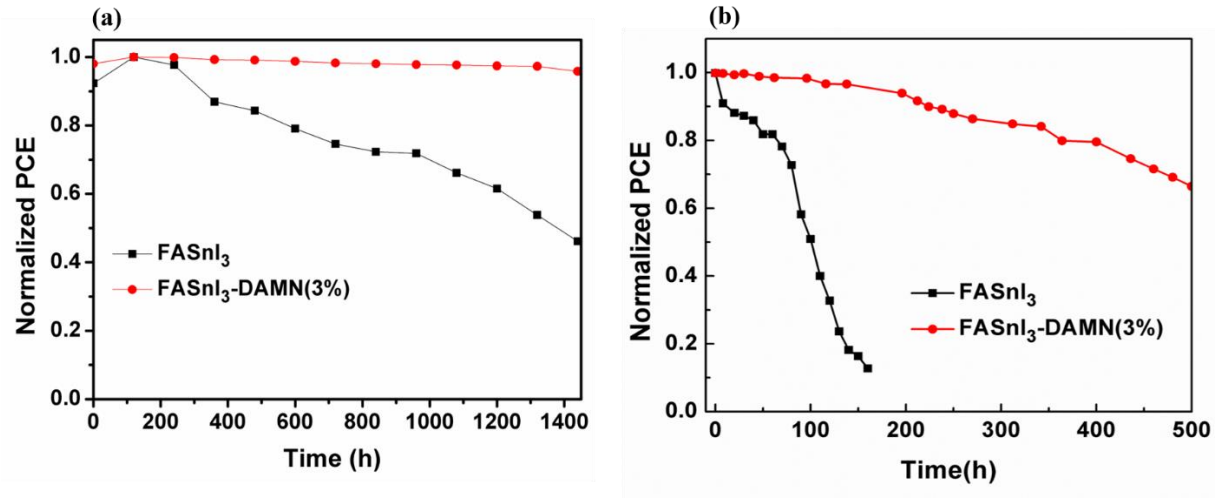

Figure 20. (a) Shelf-life stability of the FASnI3 and FASnI3-DAMN (3 mol %)-based PSCs in a N_2-filled glovebox. (b) Stability of the $FASnI_3$- DAMN (3 mol %) compared to the pristine $FASnI_3$ PSCs under maximum power point tracking and continuous AM 1.5G 1 sun illumination (with a 420 nm cutoff UV filter at 25 °C) conditions in ambient air.

3.2.10 Summary

In summary, an effective approach to improve electron transportation from the perovskite film to the electron-transport layer in Sn-PSCs by incorporating a DAMN Lewis base additive was demonstrated. Inclusion of DAMN with $FASnI_3$ reduced the lattice strain, improved the electron mobility, enhanced the electron extraction process, and reduced the recombination rate of Sn-PSCs. Consequently, the PCE of the $FASnI_3$-DAMN-based PSCs increased to 8.11% compared to 6.56% for the pristine $FASnI_3$-based PSCs. More importantly, the $FASnI_3$-DAMN-based PSCs exhibited remarkable long-term stability in efficiency for over 300 h of operation at the maximum power point tracking conditions. Furthermore, the hydrogen bonding improved the crystallinity and stabilized the perovskite film. These results can provide a new perspective for using additives to extract electrons more effectively from the perovskite absorber to the adjacent ETL layer, which can contribute to the development of Sn-PSCs.

3.2.11 References

(1) Gao, W.; Chen, C.; Ran, C.; Zheng, H.; Dong, H.; Xia, Y.; Chen, Y.; Huang, W. A-Site Cation Engineering of Metal Halide Perovskites: Version 3.0 of Efficient Tin-Based Lead-Free Perovskite Solar Cells. *Adv. Funct. Mater.* **2020**, 30, No. 2000794.

(2) Jeong, J.; Kim, M.; Seo, J.; Lu, H.; Ahlawat, P.; Mishra, A.; Yang, Y.; Hope, M. A.; Eickemeyer, F. T.; Kim, M.; Yoon, Y.; Choi, I.; Darwich, B.; Choi, S.; Jo, Y.; Lee, J.; Walker, B.; Zakeeruddin, M.; Emsley, L.; Rothlisberger, U.; Hagfeldt, A.; Kim, D.; Grätzel, M.; Kim, J. Pseudo-halide anion engineering for α-$FAPbI_3$ perovskite solar cells. *Nature* **2021**, 592, 381-385.

(3) Wang, R.; Wang, J.; Tan, S.; Duan, Y.; Wang, Z.-K.; Yang, Y. Opportunities and challenges of lead-free perovskite optoelectronic devices. *Trends Chem.* **2019**, 1, 368-379.

(4) Abdel-Shakour, M.; Chowdhury, T. H.; Matsuishi, K.; Bedja, I.; Moritomo, Y.; Islam, A. High-Efficiency Tin Halide Perovskite Solar Cells: The Chemistry of Tin (II) Compounds and Their Interaction with Lewis Base Additives during Perovskite Film Formation. *Sol. RRL* **2021**, 5, No. 2000606.

(5) Nasti, G.; Abate, A. Tin halide perovskite (ASnX3) solar cells: a comprehensive guide toward the highest power conversion efficiency. *Adv. Energy Mater.* **2020**, 10, No. 1902467.

(6) Cao, K.; Cheng, Y.; Chen, J.; Huang, Y.; Ge, M.; Qian, J.; Liu, L.; Feng, J.; Chen, S.; Huang, W. Regulated Crystallization of $FASnI_3$ Films through Seeded Growth Process for Efficient Tin Perovskite Solar Cells. *ACS Appl. Mater. Interfaces* **2020**, 12, 41454-41463.

(7) Kamarudin, M. A.; Hirotani, D.; Wang, Z.; Hamada, K.; Nishimura, K.; Shen, Q.; Toyoda, T.; Iikubo, S.; Minemoto, T.; Yoshino, K.; Hayase, S. Suppression of charge carrier recombination in lead-free tin halide perovskite via lewis base post-treatment. *J. Phys.Chem. Lett.* **2019**, 10, 5277-5283.

(8) Shao, S.; Dong, J.; Duim, H.; Gert, H.; Blake, G. R.; Portale, G.; Loi, M. A. Enhancing the crystallinity and perfecting the orientation of formamidinium tin iodide for highly efficient Snbased perovskite solar cells. *Nano Energy* **2019**, 60, 810-816.

(9) Kayesh, M. E.; Chowdhury, T. H.; Matsuishi, K.; Kaneko, R.; Kazaoui, S.; Lee, J.-J.; Noda, T.; Islam, A. Enhanced photovoltaic performance of $FASnI_3$-based perovskite solar cells with hydrazinium chloride coadditive. *ACS Energy Lett*. **2018**, 3, 1584-1589.

(10) Tai, Q.; Guo, X.; Tang, G.; You, P.; Ng, T. W.; Shen, D.; Cao, J.; Liu, C. K.; Wang, N.; Zhu, Y.; Lee, C.; Yan, F. Antioxidant grain passivation for air-stable tin-based perovskite solar cells. *Angew. Chem., Int. Ed.* **2019**, 58, 806-810.

(11) Lin, Z.; Liu, C.; Liu, G.; Yang, J.; Duan, X.; Tan, L.; Chen, Y. Preparation of efficient inverted tin-based perovskite solar cells via the bidentate coordination effect of 8-hydroxyquinoline. *Chem. Commun.* **2020**, 56, 4007-4010.

(12) Kayesh, M. E.; Matsuishi, K.; Kaneko, R.; Kazaoui, S.; Lee, J.-J.; Noda, T.; Islam, A. Coadditive engineering with 5-ammonium valeric acid iodide for efficient and stable Sn perovskite solar cells. *ACS Energy Lett.* **2019**, 4, 278-284.

(13) Chowdhury, T. H.; Kayesh, M. E.; Lee, J.-J.; Matsushita, Y.; Kazaoui, S.; Islam, A. Post- Deposition

Vapor Annealing Enables Fabrication of 1cm^{2}Lead-Free Perovskite Solar Cells. *Sol. RRL* **2019**, 3, No. 1900245.

(14) Kumar, M. H.; Dharani, S.; Leong, W. L.; Boix, P. P.; Prabhakar, R. R.; Baikie, T.; Shi, C.; Ding, H.; Ramesh, R.; Asta, M.; Graetzel, M.; Mhaisalkar, S-G.; Mathews, N. Lead-free halide perovskite solar cells with high photocurrents realized through vacancy modulation. *Adv. Mater.* **2014**, 26, 7122-7127.

(15) Meng, X.; Lin, J.; Liu, X.; He, X.; Wang, Y.; Noda, T.; Wu, T.; Yang, X.; Han, L. Highly Stable and Efficient $FASnI_3$-Based Perovskite Solar Cells by Introducing Hydrogen Bonding. *Adv. Mater.* **2019**, 31, No. 1903721.

(16) Jokar, E.; Chien, C.-H.; Fathi, A.; Rameez, M.; Chang, Y.-H.; Diau, E. W.-G. Slow surface passivation and crystal relaxation with additives to improve device performance and durability for tin-based perovskite solar cells. *Energy Environ. Sci.* **2018**, 11, 2353-2362.

(17) Li, X.; Dar, M. I.; Yi, C.; Luo, J.; Tschumi, M.; Zakeeruddin, S. M.; Nazeeruddin, M. K.; Han, H.; Grätzel, M. Improved performance and stability of perovskite solar cells by crystal crosslinking with alkylphosphonic acid ω-ammonium chlorides. *Nat. Chem.* **2015**, 7, 703-711.

(18) Li, N.; Tao, S.; Chen, Y.; Niu, X.; Onwudinanti, C. K.; Hu, C.;Qiu, Z.; Xu, Z.; Zheng, G.; Wang, L.; Zhang, Y.; Li, L.; Liu, H.; Lun, Y.; Hong, J.; Wang, X.; Liu, Y.; Xie, H.; Gao, Y.; Bai, Y.; Yang, S.; Brocks, G.; Chen, Q.; Zhou, H. Cation and anion immobilization through chemical bonding enhancement with fluorides for stable halide perovskite solar cells. *Nat. Energy* **2019**, 4, 408-415.

(19) Li, B.; Fei, C.; Zheng, K.; Qu, X.; Pullerits, T.; Cao, G.; Tian, J. Constructing water resistant $CH_3NH_3PbI_3$ perovskite films via coordination interaction. *J. Mater. Chem. A* **201**6, 4, 17018-17024.

(20) Rameez, M.; Lin, E. Y.-R.; Raghunath, P.; Narra, S.; Song, D.; Lin, M.-C.; Hung, C.-H.; Diau, E. W.-G. Development of hybrid pseudohalide tin perovskites for highly stable carbon electrode solar cells. *ACS Appl. Mater. Interfaces* **2020**, 12, 21739-21747.

(21) Liu, X.; Wu, T.; Chen, J.-Y.; Meng, X.; He, X.; Noda, T.; Chen, H.; Yang, X.; Segawa, H.; Wang, Y.; Han, L. Templated growth of $FASnI_3$ crystals for efficient tin perovskite solar cells. *Energy Environ. Sci.* **2020**, 13, 2896-2902.

(22) Abdel-Shakour, M.; Chowdhury, T. H.; Matsuishi, K.; Moritomo, Y.; Islam, A. Chemical passivation of the under coordinated Pb^{2+} defects in inverted planar perovskite solar cells via β- diketone Lewis base additives. *Photochem. Photobiol. Sci.* **2021**, 20, 357-367.

(23) Vashista, M.; Paul, S. Correlation between full width at half maximum (FWHM) of XRD peak with residual stress on ground surfaces. *Philos. Mag.* **2012**, 92, 4194-4204.

(24) Wu, J.; Liu, S.-C.; Li, Z.; Wang, S.; Xue, D.-J.; Lin, Y.; Hu, J.-S. Strain in perovskite solar cells: origins, impacts, and regulation. *Natl. Sci. Rev.* **2021**, 8, No. nwab047.

(25) Zhu, C.; Niu, X.; Fu, Y.; Li, N.; Hu, C.; Chen, Y.; He, X.; Na, G.; Liu, P.; Zai, H.; Ge, Y.; Lu, Y.; Ke, X.; Bai, Y.; Yang, S.; Chen, P.; Li, Y.; Sui, Y.; Zhang, L.; Zhou, H.; Chen, Q. Strain engineering in perovskite solar cells and its impacts on carrier dynamics. *Nat. Commun.* **2019**, 10, No. 815.

(26) Steele, J. A.; Jin, H.; Dovgaliuk, I.; Berger, R. F.; Braeckevelt, T.; Yuan, H.; Martin, C.; Solano, E.; Lejaeghere, K.; Rogge, S.; Notebaert, S.; Vandezande1, W.; Janssen, K.; Goderis, B.; Debroye, E.; Wang, Y.;

Dong, Y.; Ma, D.; Saidaminov, M.; Tan, H.; Lu, Z.; Dyadkin, V.; Chernyshov, D.; Speybroeck, V.; Sargent, E.; Hofkens, J.; Roeffaers, M. Thermal unequilibrium of strained black $CsPbI_3$ thin films. *Science* **2019**, 365, 679-684.

(27) Zhao, J.; Deng, Y.; Wei, H.; Zheng, X.; Yu, Z.; Shao, Y.; Shield, J. E.; Huang, J. Strained hybrid perovskite thin films and their impact on the intrinsic stability of perovskite solar cells. *Sci. Adv.* **2017**, 3, No. eaao5616.

(28) Nishimura, K.; Hirotani, D.; Kamarudin, M. A.; Shen, Q.; Toyoda, T.; Iikubo, S.; Minemoto, T.; Yoshino, K.; Hayase, S. Relationship between lattice strain and efficiency for Sn perovskite solar cells. *ACS Appl. Mater. Interfaces* **2019**, 11, 31105-31110.

(29) Majumdar, A.; Das, S. C.; Shripathi, T.; Hippler, R. Chemical synthesis and surface morphology of amorphous hydrogenated carbon nitride film deposited by N_2/CH_4 dielectric barrier discharge plasma. *Compos. Interfaces* **2012**, 19, 161-170.

(30) Ran, C.; Gao, W.; Li, J.; Xi, J.; Li, L.; Dai, J.; Yang, Y.; Gao, X.; Dong, H.; Jiao, B.; Spanopoulos, I.; Malliakas, D.; Hou, X.; Kanatzidis, G.; Wu, Z. Conjugated organic cations enable efficient self-healing $FASnI_3$ solar cells. *Joule* **2019**, 3, 3072-3087.

(31) Gu, W.; Xu, X.; Chen, J.; Ma, B.; Qin, M.; Zhu, W.; Qian, J.; Qin, Z.; Shen, W.; Lu, Y.; Zhang, W.; Chen, S.; Lu, X.; Huang, W. Oriented Perovskite Crystal towards Efficient Charge Transport in FASnI3 Perovskite Solar Cells. *Sol. RRL* **2020**, 4, No. 2000153.

(32) Golubev, T.; Liu, D.; Lunt, R.; Duxbury, P. Understanding the impact of C60 at the interface of perovskite solar cells via drift diffusion modeling. *AIP Adv.* **2019**, 9, No. 035026.

(33) Li, Y.; Zhao, Y.; Chen, Q.; Yang, Y.; Liu, Y.; Hong, Z.; Liu, Z.; Hsieh, Y.-T.; Meng, L.; Li, Y.; Yang, Y. Multifunctional fullerene derivative for interface engineering in perovskite solar cells. *J. Am. Chem. Soc.* **2015**, 137, 15540-15547.

(34) Kakavelakis, G.; Paradisanos, I.; Paci, B.; Generosi, A.; Papachatzakis, M.; Maksudov, T.; Najafi, L.; Del Rio Castillo, A. E.; Kioseoglou, G.; Stratakis, E.; Bonaccorso, F.; Kymakis, E. Extending the continuous operating lifetime of perovskite solar cells with a molybdenum disulfide hole extraction interlayer. *Adv. Energy Mater.* **2018**, 8, No. 1702287.

3.3 Formamidinesulfinic acid Lewis base additive for reduced oxidation and improved stability in tin-based perovskite solar cells

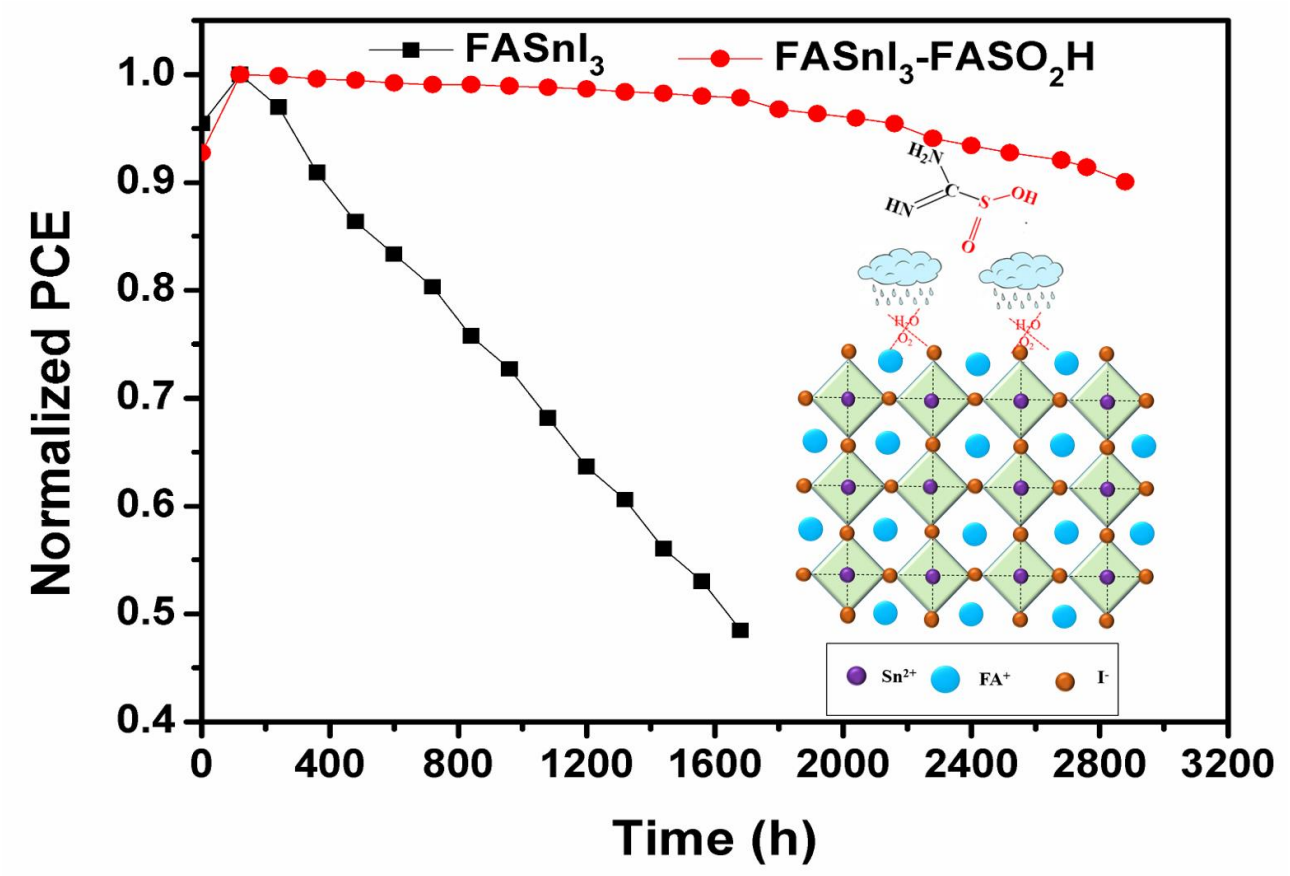

3.3.1 Formamidinesulfinic acid Lewis base additive

Perovskite solar cells have increased their power conversion efficiency by 25.6% in less than a decade, have established themselves as a leading candidate for next-generation solar cells, and are currently competing against traditional silicon solar cells.[1] The toxicity of Pb and its negative environmental impacts, on the other hand, make commercialization and large-scale manufacture of Pb-PSCs difficult.[2] Recently, researchers have focused their attention on Sn-PSCs as a possible alternative for fabricating nontoxic PSCs. Along with being less poisonous, Sn perovskite materials exhibit superior optoelectronic properties to Pb analogs, including a narrower band gap, lower exciton binding energy, and a smaller radius than Pb^{2+}.[3] Sn-PSCs suffer from critical problems such as the $FASnI_3$ absorber layer of Sn-PSCs form Sn vacancies due to the quicker oxidation of Sn^{2+} to Sn^{4+}. Furthermore, the Perovskite crystallinity and morphology are also affected by the rapid interaction between perovskite components in the precursor solution. Due to these drawbacks, Sn-PSCs possess a higher recombination rate than Pb-PSCs, which has a negative effect on their photovoltaic performance and stability under solar irradiation. [4] To reduce oxidation of Sn^{2+} to Sn^{4+} and improve the crystallinity of Sn perovskite materials, Lewis base additions were widely used in Sn-PSC fabrication. In order to improve the quality of the fabricated Sn-based perovskite film, Lewis base additives can be used as morphological controller, reducing agents, and/or antioxidants using their effective functional groups.[5] Although the incorporation of additives within the perovskite precursor improved the respective Sn-PSC performances, the easier oxidation of Sn^{2+} to Sn^{4+} resulted in an increased recombination rate of the photogenerated electron-hole pairs, which is challenging factor for achieving high photovoltaic performance. In this work the strong reducing agent $FASO_2H$ Lewis base additive was added to perovskite precursor to reduce the oxidation of Sn^{2+} to Sn^{4+}. [6] Furthermore, the sulfinic acid group in $FASO_2H$ can interact with perovskite precursor to improve the morphology and prevent the permeation of oxygen and moisture to the absorber layer because it is hydrophobic nature.[7] The utilizing of $FASO_2H$ retarded the oxidation of the perovskite film,

improved the crystallinity and morphology of the fabricated perovskite films, which improved the PCE 6.7 % to 7.4 % after the inclusion of $FASO_2H$. Furthermore, the water contact angle of the $FASnI_3$-$FASO_2H$ perovskite film increased compared to the pristine $FASnI_3$, which resulted in very stable devices after inclusion of $FASO_2H$ by keeping 90% of the initial PCE till 2880 h under nitrogen storage.

3.3.2 Interaction of formamidinesulfinic acid with perovskite precursor

The $FASO_2H$ Lewis base can interact with SnI_2 in the perovskite precursor using the SO_2H and amino groups. To observe the interaction, the SnI_2-$FASO_2H$ was prepared, then The FTIR of SnI_2-$FASO_2H$ powder was measured compared to SnI_2 and $FASO_2H$ as shown in **Figure 1a**. The two peak at 991 and 1024 cm^{-1}, which corresponding to SO_2H group in $FASO_2H$ was shifted to 996 and 1026 cm^{-1}, respectively for $FASnI_3$-$FASO_2H$ adduct. [8] This can be attributed to the donation of a lone pair of electrons from the oxygen of the SO_2H group in $FASO_2H$ to the vacant orbital of the SnI_2 as explained in **Figure 1b**. [9] This interaction improves the morphology of the perovskite films by retarding the interaction between SnI_2 and FAI. Furthermore, the stretching vibration of the NH group of SnI_2-$FASO_2H$ was shifted from 3020 to 3025 cm^{-1}, and from 3226 to 3235 cm^{-1} with increasing intensity of these peaks compared to $FASO_2H$, while for SnI_2, no peaks appeared in this region as shown on **Figure 1c**.

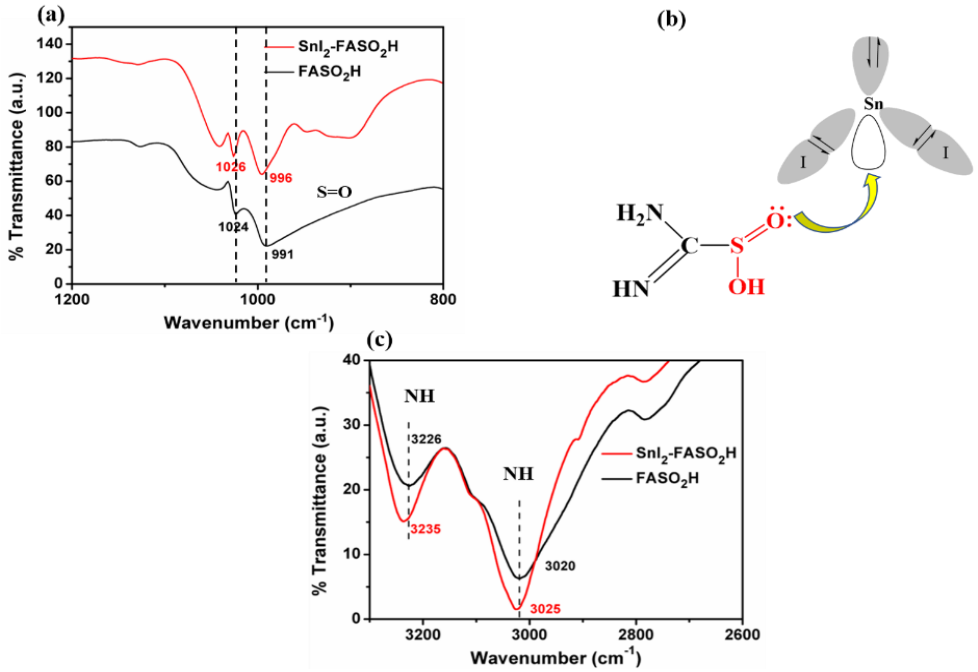

Figure 1. (a, c) FTIR spectra of $FASO_2H$ compared to SnI_2-$FASO_2H$ adduct. (b) Illustration of interaction between $FASO_2H$ Lewis base with the vacant orbital of SnI_2.

The formation of hydrogen bonds between the hydrogen atoms in the amino group and the iodide anion in SnI_2 is responsible for these shifts with changed intensities. [10,11] By forming hydrogen bonds, it is possible to control the crystal growth of the $FASnI_3$ film and so obtain a compact perovskite film. Additionally, the H···I hydrogen bonding interactions can inhibit iodide ions from migration and maintain the weak Sn–I bond strong, which is important for the long-term stability of the PSCs.

3.3.3 Oxidation the perovskite precursor solution over time

To investigate the effect of adding $FASO_2H$ Lewis base additive on the oxidation of the perovskite precursor solution, 3mol% of $FASO_2H$ was added to modified solution compared to the pristine. As shown in **Figure 2** the oxidation of the perovskite solution $FASnI_3$-$FASO_2H$(3mol%) started later than the pure $FASnI_3$ precursor solution, which indicates retarding the oxidation of the perovskite solution after adding $FASO_2H$ Lewis base additive. This can be attributed to the strong reducing ability of $FASO_2H$. [6]

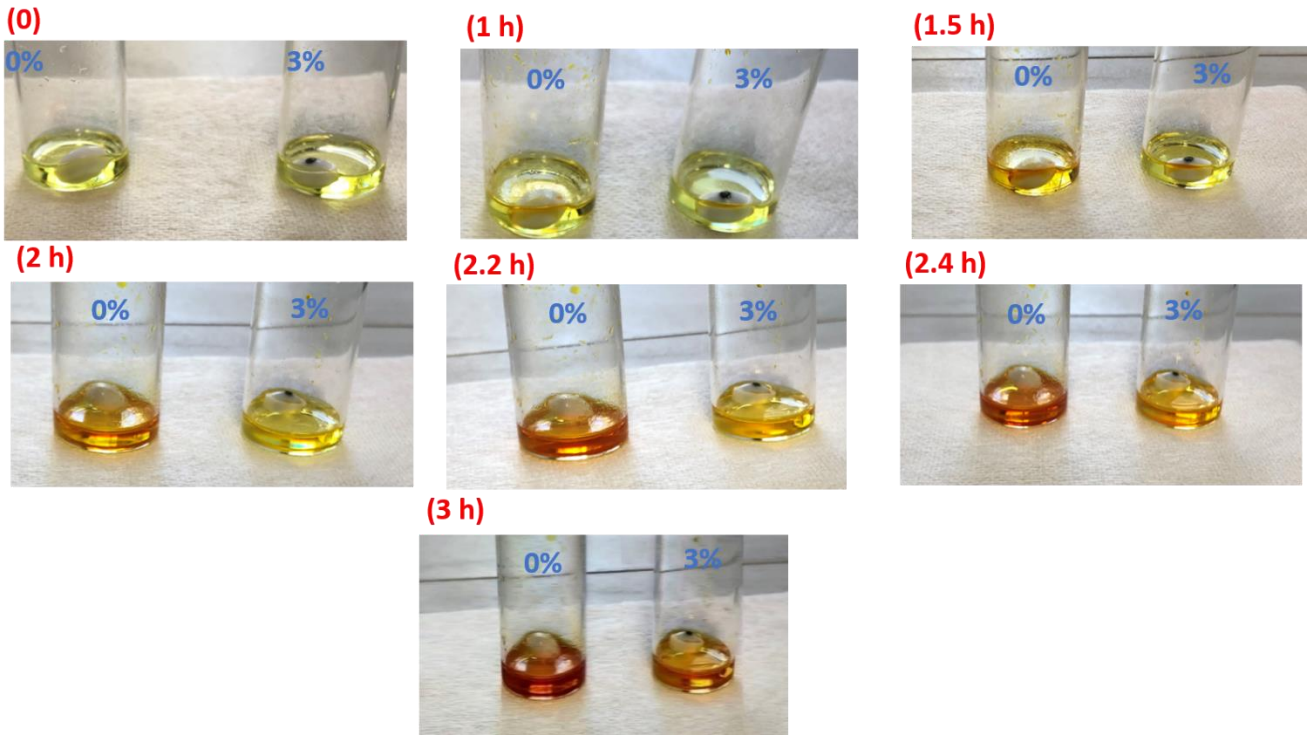

Figure 2. Oxidation over time for the perovskite solutions $FASnI_3$ and $FASnI_3$-$FASO_2H$ (3mol%) over time

3.3.4 Crystallinity and morphology of the perovskite films

The XRD pattern of the pristine $FASnI_3$ film was compared to that of the $FASnI_3$-$FASO_2H$ films to investigate the influence of $FASO_2H$ on the crystal structure of $FASnI_3$. The XRD peaks of the fabricated films were located at 13.96, 24.31, 28.15, and 31.53°, which correspond to the orthorhombic $FASnI_3$ perovskite phase's (100), (102), (200), and (122) crystal planes, respectively, as shown in **Figure 3**.[12] The perovskite films become oriented preferably to (100) and (200) direction with $FASO_2H$ additives. Furthermore, the modified $FASnI_3$-$FASO_2H$ perovskite films showed a decrease in the full width at half-maximum (FWHM) compared to pristine $FASnI_3$ (see **Table 1**). The reduction in FWHM occurred in all angles, which indicates better crystallinity across the $FASnI_3$ absorber layer after the inclusion of the $FASO_2H$ additive. [13, 14] This improved in the crystallinity can be attributed to the interaction of $FASO_2H$ with the perovskite precursor, which decrease the strength of interaction and resulted in more crystalline perovskite film.

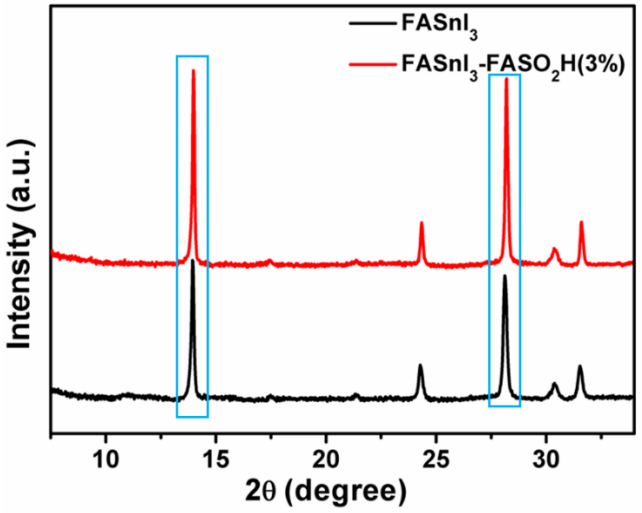

Figure 3. XRD patterns of $FASnI_3$ and $FASnI_3$-$FASO_2H$ (3mol%) perovskite films.

Table.1 The FWHM of $FASnI_3$ and $FASnI_3$-$FASO_2H$ (3mol%) perovskite films.

2-Theta	$FASnI_3$	$FASnI_3$-$FASO_2H$(3%)
13.94	0.121	0.0928
24.25	0.1943	0.1069
28.11	0.1623	0.1002
31.51	0.1995	0.1102

To investigate the effect of adding $FASO_2H$ on the surface morphology of the perovskite films, the SEM of $FASnI_3$ and $FASnI_3$-$FASO_2H$ was measured. As given in **Figure 4 a, b**, the pristine $FASnI_3$ film showed a small grain size. On adding 3 mol % of $FASO_2H$, a compact and denser perovskite films with bigger grain size was obtained. Furthermore, the crystalline size calculated using the Scherrer equation showed an increase after inclusion of $FASO_2H$ (3mol%) as shown in **Table 2**. SEM images revealed that using $FASO_2H$ improved the quality of the perovskite film, which is important for enhancing photovoltaic performance. From the XRD and SEM results, we noticed improved crystallinity and morphology of the $FASnI_3$ film on inclusion of $FASO_2H$.

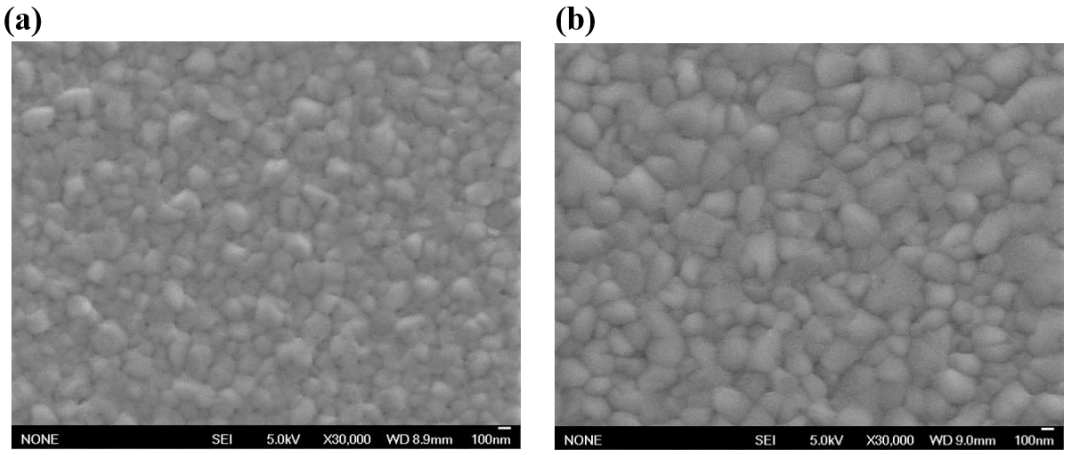

Figure 4. SEM images of (a) $FASnI_3$ and (b) $FASnI_3$-$FASO_2H$ (3mol%) perovskite films.

Table 2. The crystalline size calculated from the XRD peaks of the $FASnI_3$ and $FASnI_3$- $FASO_2H$ (3mol%) perovskite film

Perovskite film / 2 Theta (degree)	$FASnI_3$	$FASnI_3$-$FASO_2H$(3%)
13.94°	66.14	86.24
24.25°	41.82	76.01
28.11°	50.45	81.73
31.51°	41.37	74.90

3.3.5 Perovskite films resistance to water

Using $FASO_2H$ with the -SO_2H hydrophobic group is expected to increase resistance to water. To investigate that, the water contact angle of perovskite films $FASnI_3$ and $FASnI_3$-$FASO_2H$ was measured. As Shown in **Figure 5** the $FASnI_3$-$FASO_2H$ exhibited an increase in the contact angle (31.2°) compared to the pristine $FASnI_3$ (39.6°).

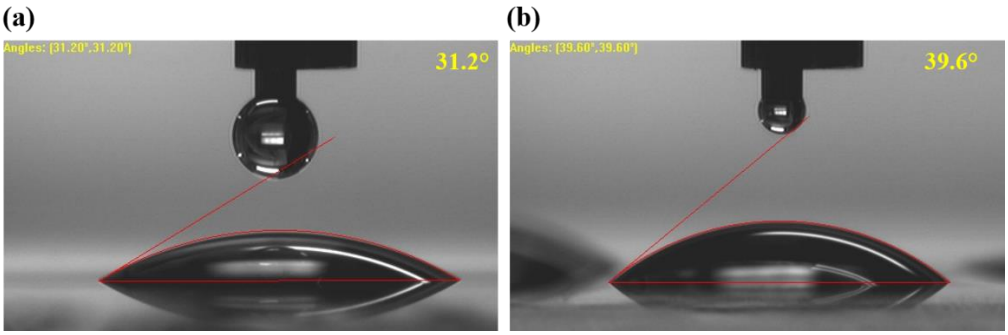

Figure 5. Water contact angle of (a) $FASnI_3$ and (b) $FASnI_3$-$FASO_2H$ (3mol%) perovskite films.

3.3.6 Photophysical properties of the perovskite films

By adding $FASO_2H$ to the perovskite films, the UV-visible absorption spectra exhibit a small blue shift at the band edge as shown in **Figure 6**. Furthermore, the PL spectrum shows the emission peak of pristine $FASnI_3$ at ~882 nm. On adding 3 mol% $FASO_2H$ to $FASnI_3$, the emission peak was blue-shifted and the blue shift to 874 nm (**Figure 7a**). This blue shift indicates that the introduction $FASO_2H$ lead to formation of perovskite films with less defect and improved film quality.

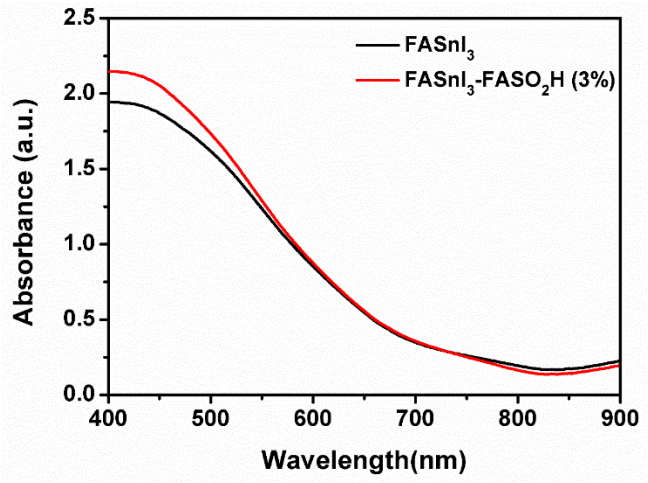

Figure 6. The UV-visible spectra of (a) $FASnI_3$ and (b) $FASnI_3$-$FASO_2H$ (3mol%) perovskite films.

The PL spectra of the $FASnI_3$-$FASO_2H$ perovskite film was measured and compared to $FASnI_3$ perovskite film to better understand the effect of $FASO_2H$ on the photophysical properties of the perovskite layer (**Figure 7a**). Adding the $FASO_2H$ (3mol%) to the perovskite solution leads to increasing the intensity of the PL peak, which indicate that adding $FASO_2H$ reduces the non-radiative recombination. To understand more about the charge transfer kinetics, the TRPL of the perovskite film was measured (**Figure 7 b**). It is found from the TRPL measurements that the decay life time was increased from 5 to 7.7 ns after adding the $FASO_2H$, which suggest decreasing the recombination rate after adding $FASO_2H$. This behavior can be expected, because adding $FASO_2H$ to the perovskite layer improve the morphology and reduced the defects, which lead to reduced recombination rate.

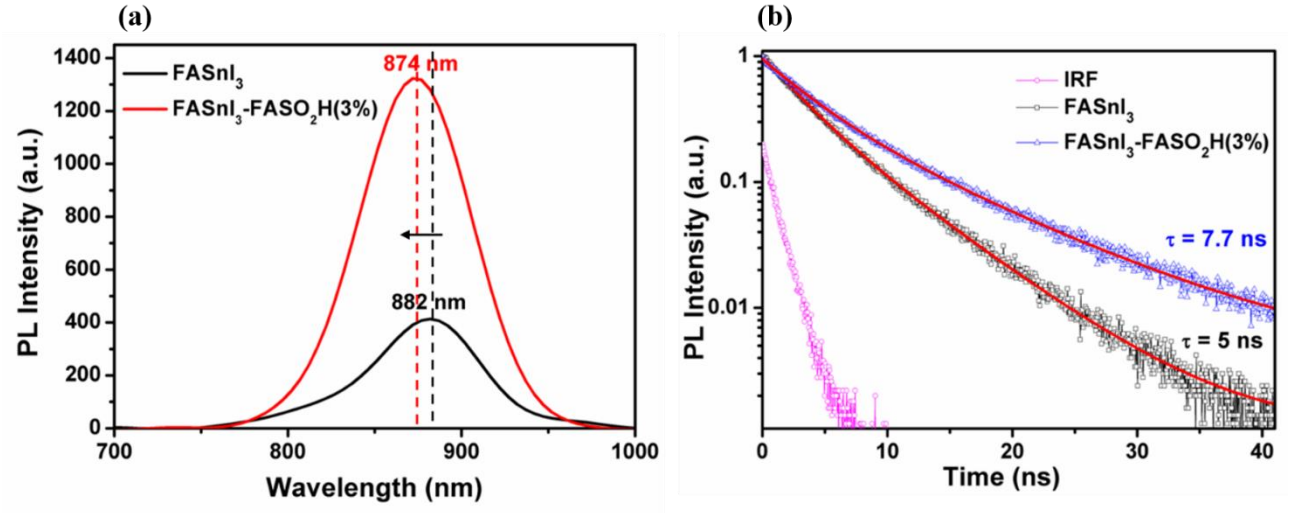

Figure 7. (a)The Steady-state PL spectra and (b) Normalized time-resolved photoluminescence spectra (TRPL) of $FASnI_3$ and $FASnI_3$-$FASO_2H$ (3mol%) perovskite films.

3.3.7 Photovoltaic performance and reproducibility

The inverted planar PSCs with configuration ITO/PEDOT:PSS/$FASnI_3$/C_{60}/BCP/Ag were fabricated to evaluate the influence of $FASO_2H$ on the photovoltaic performance of PSCs.

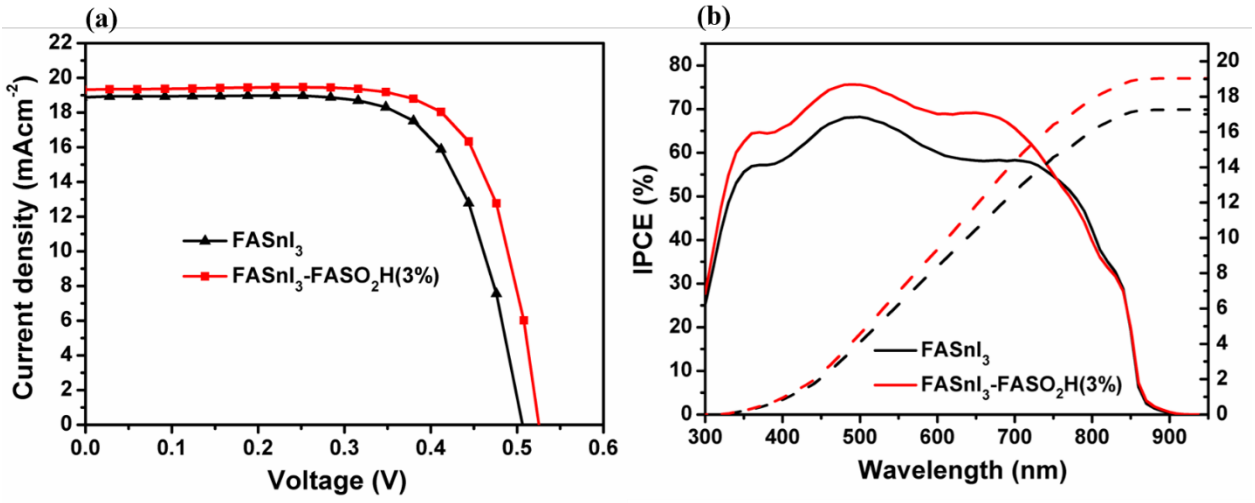

Figure 8. (a) IPCE and (b) the *J*−*V* curves of the $FASnI_3$ and $FASnI_3$-$FASO_2H$ (3mol%) based PSCs.

Table 3. The photovoltaic data of the $FASnI_3$ and $FASnI_3$-$FASO_2H$(3mol%) based PSCs

Device	J_{SC}(mAcm^{-2})	V_{OC} (V)	F.F.	PCE [%]
$FASnI_3$	18.88	0.506	0.697	6.67
$FASnI_3$-$FASO_2H$ (3mol%)	19.32	0.525	0.732	7.43

Figure 8a shows the IPCE of the fabricated PSCs using $FASO_2H$. The addition of $FASO_2H$ (3mol%) increased the photogenerated current of the modified PSCs. The *J*−*V* curves of the fabricated PSCs were measured under 1 sun illumination conditions at 100 mW cm^{-2}. The *J*−*V* curve of pristine $FASnI_3$ compared to those of $FASnI_3$- $FASO_2H$ is shown in **Figure 8b**. The $FASnI_3$-$FASO_2H$ based PSCs with 3 mol % $FASO_2H$ showed J_{SC} of 19.32 mA cm^{-2}, V_{OC} of 0.525 V, and FF of 0.732, yielding a PCE of 7.43%. While, the $FASnI_3$-based PSCs showed a PCE of 6.67% with lower J_{SC} and V_{OC} values of 18.88 mA cm^{-2} and 0.506 V, respectively. The detailed PSC parameters are summarized in **Table 3**. The photovoltaic results show that adding 3 mol % $FASO_2H$ to $FASnI_3$ boosted the J_{SC} of the PSCs due to the improved quality of the perovskite film and reduced the Sn^{2+} oxidation to Sn^{4+}, which decreased the carrier recombination and hennce the V_{OC} and FF were increased. Interestingly, the photovoltaic parameters of the fabricated PSCs showed good reproducibility, as shown in **Figure 9**, and the PSCs based on $FASO_2H$ (3 mol %) gave the best average performance.

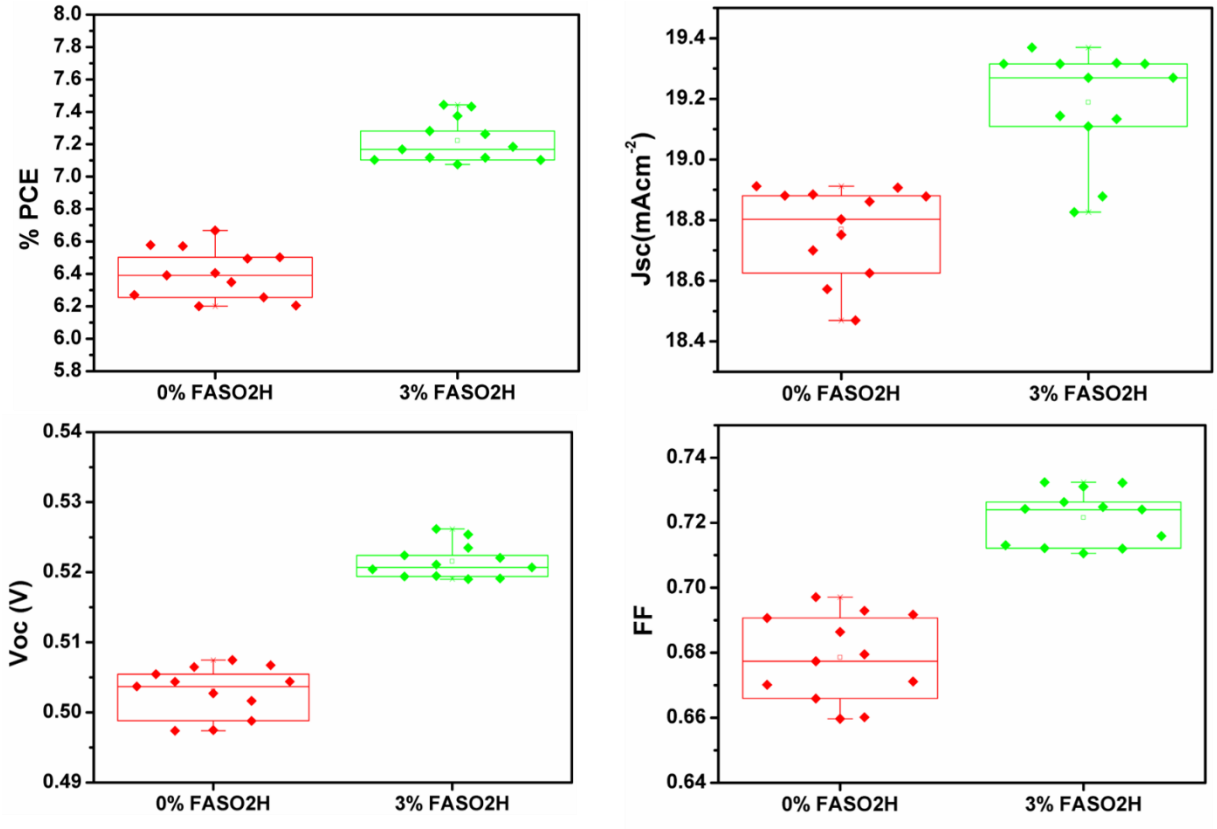

Figure 9. The statistical distribution of the (a) PCE, (b) J_{SC}, (c) V_{OC}, (d) FF of the $FASnI_3$ and $FASnI_3$-$FASO_2H$ (3mol%) based PSCs.

3.3.8 Stability of PSCs

The effect of the shelf-life stability inside the N_2 glovebox on the performance of the fabricated PSCs was examined, as shown in **Figure 10**. The pristine $FASnI_3$ based PSCs started to degrade after 200 h and loss more than 50% of the initial PCE after 1600h. While the $FASnI_3$-$FASO_2H$ based PSCs keep 90% of the initial PCE till 2880 h. The improved stability can be attributed to the presence of the hydrophobic group -SO_2H in $FASO_2H$, which prevent the moisture and water permeation to the perovskite materials. IN addition to the formation of hydrogen bonding between iodide anions in the perovskite with the hydrogen atoms of amino groups of $FASO_2H$.

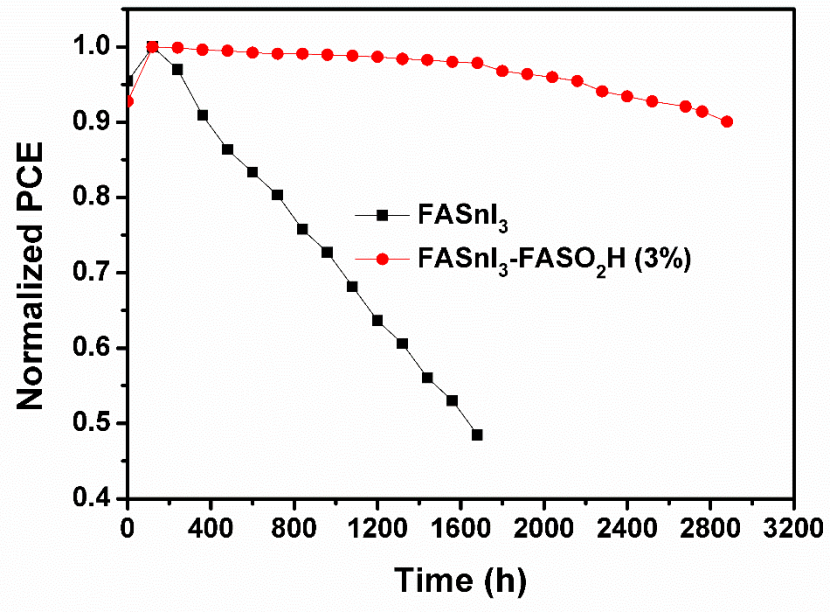

Figure 10. Shelf-life stability of the $FASnI_3$ and $FASnI_3$-$FASO_2H$ (3 mol %) based PSCs in a N_2-filled glovebox.

3.3.9 Summary

In summary, the $FASO_2H$ Lewis base additive could diminish the oxidation of Sn^{2+} to Sn^{4+} due to its strong reduction ability. The interaction of $FASO_2H$ with SnI_2 in the perovskite film reduce the interaction strength between the perovskite precursor, which improved the crystallinity and the morphology of the perovskite film as indicated from the XRD and SEM. Adding the $FASO_2H$ to the perovskite solution leads to increasing the intensity of the PL peak, which indicate reduction the non-radiative recombination. Consequently, the PCE of the $FASnI_3$-$FASO_2H$-based PSCs increased to 7.43 % compared to 6.67% for the pristine $FASnI_3$-based PSCs. More importantly, the $FASnI_3$-$FASO_2H$-based PSCs exhibited remarkable long-term stability by keep 90% of the initial PCE till 2880 h under N_2 storage.

3.3.10 References

(1) Li, D.; Zhang, D.; Lim, K. S.; Hu, Y.; Rong, Y.; Mei, A.; Park, N. G.; Han, H. A Review on Scaling Up Perovskite Solar Cells. *Adv. Funct. Mater.* **2021,** 31, 2008621.

(2) Liu, F.-W.; Biesold, G.; Zhang, M.; Lawless, R.; Correa-Baena, J.-P.; Chueh, Y.-L.; Lin, Z. Recycling and recovery of perovskite solar cells. *Mater. Today* **2021**, 43, 185-197.

(3) Abdel-Shakour, M.; Chowdhury, T. H.; Matsuishi, K.; Bedja, I.; Moritomo, Y.; Islam, A. High-Efficiency Tin Halide Perovskite Solar Cells: The Chemistry of Tin (II) Compounds and Their Interaction with Lewis Base Additives during Perovskite Film Formation. *Sol. RRL* **2021**, 5, No. 2000606.

(4) Li, Z.; Li, X.; Wang, M.; Cai, M.; Shi, X.; Mo, Y.; Chen, X.; Ren, D.; Yang, M.; Liu, X.; Dai, S. Enhanced Photovoltaic Performance via a Bifunctional Additive in Tin-Based Perovskite Solar Cells. *ACS Appl. Energy Mater.* **2021**.

(5) Yao, H.; Zhou, F.; Li, Z.; Ci, Z.; Ding, L.; Jin, Z. Strategies for Improving the Stability of Tin-Based Perovskite ($ASnX_3$) Solar Cells. *Adv. Science* **2020,** 7, 1903540.

(6) Shashoua, V. E. Formamidine sulfinic acid as a biochemical reducing agent. *Biochemistry*, **1964,** *3*, 1719-1720.

(7) Dacquin, J.-P.; Cross, H. E.; Brown, D. R.; Düren, T.; Williams, J. J.; Lee, A. F.; Wilson, K. Interdependent lateral interactions, hydrophobicity and acid strength and their influence on the catalytic activity of nanoporous sulfonic acid silicas. *Green Chem.* **2010,** 12, 1383-1391.

(8) Lewis, D.; Mama, J.; Hawkes, J. An investigation into the structure and chemical properties of formamidine sulfinic acid. *Appl. Spectrosc.***2014,** 68, 1327-1332.

(9) Rameez, M.; Lin, E. Y.-R.; Raghunath, P.; Narra, S.; Song, D.; Lin, M.-C.; Hung, C.-H.; Diau, E. W.-G. Development of hybrid pseudohalide tin perovskites for highly stable carbon-electrode solar cells. *ACS Appl. Mater. Interfaces* **2020,** *12* (19), 21739-21747.

(10) Meng, X.; Lin, J.; Liu, X.; He, X.; Wang, Y.; Noda, T.; Wu, T.; Yang, X.; Han, L. Highly Stable and Efficient $FASnI_3$-Based Perovskite Solar Cells by Introducing Hydrogen Bonding. *Adv. Mater.* **2019**, 31, No. 1903721.

(11) Li, B.; Fei, C.; Zheng, K.; Qu, X.; Pullerits, T.; Cao, G.; Tian, J. Constructing water resistant $CH_3NH_3PbI_3$ perovskite films via coordination interaction. *J. Mater. Chem. A* **2016**, 4, 17018-17024.

(12) Abdel-Shakour, M.; Chowdhury, T. H.; Matsuishi, K.; Karim, M. A.; He, Y.; Moritomo, Y.; Islam, A. Diaminomaleonitrile Lewis Base Additive for Push–Pull Electron Extraction for Efficient and Stable Tin-Based Perovskite Solar Cells. *ACS Appl. Energy Mater.* **2021,** 4, 12515-12524.

(13) Liu, X.; Wu, T.; Chen, J.-Y.; Meng, X.; He, X.; Noda, T.; Chen, H.; Yang, X.; Segawa, H.; Wang, Y.; Han, L. Templated growth of $FASnI_3$ crystals for efficient tin perovskite solar cells. *Energy Environ. Sci.* **2020**, 13, 2896-2902.

(14) Abdel-Shakour, M.; Chowdhury, T. H.; Matsuishi, K.; Moritomo, Y.; Islam, A. Chemical passivation of the under coordinated Pb^{2+} defects in inverted planar perovskite solar cells via β- diketone Lewis base additives. *Photochem. Photobiol. Sci.* **2021**, 20, 357-367.

Chapter 4 Conclusions

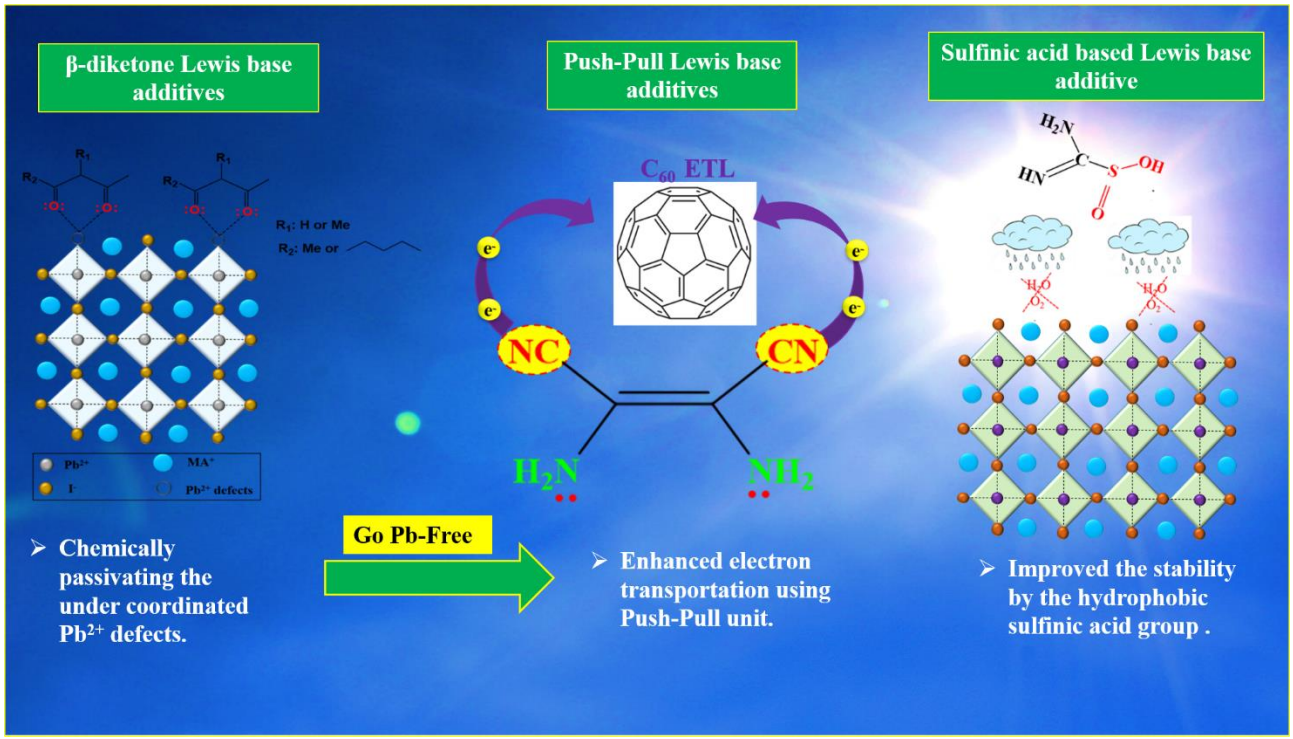

Conclusions

The most efficient approach for mankind to meet its future energy demands is through the development of renewable energy sources. In this regard, the sun is the most dependable and never-ending renewable energy source. As a result, technological advancements in solar cells, which convert sunlight into electricity, have undergone continuous improvement over time. Perovskite solar cells have been identified as a promising new technique for capturing solar energy. Within a few years, as a result of global research efforts, the power conversion efficiency of PSCs has approached that of proven photovoltaic technology. Because PSCs are inexpensive and easy to fabricated, researchers have been inspired to overcome the challenges they face.

In PSCs, the crucial component impacting performance is the perovskite absorber layer. Thus, by fabricating a perovskite layer with ideal properties and a robust stable nature, the efficiency and stability difficulties will be resolved. Innovative design, rigorous analysis, and optimization of fabrication technologies are all being pursued in order to accomplish these aims. The major goal of this thesis is to study the influence of various types of Lewis base additions on crystallinity, carrier recombination, and the resulting photovoltaic performance and stability.

The Lewis additives can affect the performance of PSCs in different ways; such as interacting with the perovskite precursor to control the morphology of the perovskite film and/or reducing the oxidation process. While, another Lewis base additives using their effective functional groups can passivate the defects, improve the electron mobility and reduce the lattice strain.

In this research, I have successfully introduced the use of bidentate Lewis base additives, which effectively passivated the surface defects of the Pb-PSCs. Through a one-step spin-coating method, the two bidentate anchoring acac and R-acac chemically passivated the under coordinated Pb^{2+} defects generated on the perovskite films. The two carbonyl groups of the β-diketone passivators could successfully interact with Pb^{2+} defects by forming a coordination bond. The FTIR for the modified perovskite films showed a clear peak for C=O group, which ensured the interaction between the two β-diketone Lewis base additives and the undercoordinated Pb^{2+}. Furthermore, the enhanced

intensity of the PL peaks and the blue shift of the passivated perovskite films using the two Lewis bases additives demonstrated improved passivation for defects compared to the pristine perovskite films. As a result, the PCE of the acac and R-acac passivated PSCs was higher than that of the pristine PSCs by 19% and 45%, respectively. Indeed, the longer alkyl chains in R-acac assist in the formation of a more stable bond with the under coordinated Pb^{2+} defects, which explains the better passivation and improved photovoltaic performance. These findings ensured the enhancing impact of using the bidentate ligands, which can efficiently passivate the surface defects of the PSCs.

In attempt to improve electron mobility, minimize lattice strain, and decrease the recombination rate of Sn-PSCs, the effective strategy of utilizing push-pull Lewis base additive DAMN was used. The electron withdrawing group in the DAMN Lewis base additive, which has two cyano groups in its structure, efficiently extracted electrons from the perovskite layer and transferred them to the neighboring ETL. The $FASnI_3$-DAMN based PSCs exhibit a 42 percent increase in electron mobility over pristine $FASnI_3$ and a 2.3-fold increase in transient photocurrent decay life time, indicating an increase in electron transport after incorporation of DAMN. Aside from the successful electron transportation enhancement, the $FASnI_3$-DAMN perovskite absorbers demonstrated a lower carrier recombination rate, thanks to the simultaneous reduction of lattice strain of the $FASnI_3$-DAMN film. It was thus found that the fabricated $FASnI_3$-DAMN based PSCs resulted in an 8.11 percent in PCE, as well as a highly light soaking stable performance of over 300 h w operation at the maximum power point tracking conditions. Furthermore, the hydrogen bonding improved the crystallinity and stabilized the perovskite film. These findings could open up new avenues for employing additives to extract electrons more efficiently from the perovskite absorber to the neighboring ETL layer, which can assist in the development of Sn-PSCs.

With the goal of decreasing Sn^{2+} to Sn^{4+} oxidation and increasing Sn-PSCs crystallinity and stability the strong reducing agent $FASO_2H$ Lewis base additive with its hydrophobic group in its formula was used.

The addition of $FASO_2H$ enhanced the PCE from 6.7% to 7.4% by delaying the oxidation of the perovskite film and improving the crystallinity and morphology of the fabricated perovskite films. Additionally, the water contact angle of the $FASnI_3$-$FASO_2H$ perovskite film increased when compared to the pristine $FASnI_3$, resulting in extremely stable devices with the $FASO_2H$ incorporation by retaining 90% of the initial PCE until 2880 h under nitrogen storage.

In conclusion, utilizing molecularly effective Lewis base additives with different functional groups can control many factors during the fabrication processes of PSCs such as interaction process, crystallinity and carrier recombination, which can contribute to the development of the photovoltaic performance and stability of PSCs.

List of Publications

(A) Related to my PhD studies

I) Peer-Reviewed Journals

[1] **Muhammad Abdel-Shakour**, Towhid H. Chowdhury, Kiyoto Matsuishi, Idriss. Bedja, Yutaka Moritomo and Ashraful Islam. "High-Efficiency Tin Halide Perovskite Solar Cells: The Chemistry of Tin (II) Compounds and Their Interaction with Lewis Base Additives during Perovskite Film Formation". *Sol. RRL* **2021**, 5, 2000606, 1-24.

[2] **Muhammad Abdel-Shakour**, Towhid H. Chowdhury, Kiyoto Matsuishi, Yutaka Moritomo and Ashraful Islam. "Chemical passivation of the undercoordinated Pb^{2+} defects in inverted planar perovskite solar cells via β-diketone lewis base additives". *Photochem. Photobiol. Sci.* **2021**, 20, 357-367.

[3] **Muhammad Abdel-Shakour**, Towhid H. Chowdhury, Kiyoto Matsuishi, Md. Abdul Karim, Yulu He, Yutaka Moritomo, and Ashraful Islam. "Diaminomaleonitrile Lewis Base Additive for Push-Pull Electron Extraction for Efficient and Stable Tin-Based Perovskite Solar Cells". *ACS Appl. Energy Mater.* **2021**, 4, 11, 12515– 12524.

[4] **Muhammad Abdel-Shakour**, Kiyoto Matsuishi, and Ashraful Islam. Formamidinesulfinic acid Lewis base additive for reduced oxidation and improved stability in tin-based perovskite solar cells. **(Under Preparation For Submission)**

[5] Yulu He, Imane Abdellaoui, **Muhammad Abdel-Shakour**, Towhid Hossain Chowdhury, Muhammad Akmal Kamarudin, Ana Flávia Nogueira, Qing Shen, Shuzi Hayase, Ashraful Islam, Takeaki Sakurai. "Study of open circuit voltage loss mechanism in perovskite solar cells". *Jpn. J. Appl. Phys.* **2021**, 60 SBBF13.

II) Conferences

[1] **Muhammad. Abdel-Shakour**, Towhid H. Chowdhury, Kiyoto Matsuishi, Ashraful Islam. "Suppression of the Pb^{2+} defects in the perovskite films using Lewis- base additives in perovskite solar cells". *International online conference on Hybrid materials and optoelectronic devices, Nano Ge*, **2020.**

(B) Other Publications

[1] Md Faiz Shah, Antoine Mirloup, Towhid H. Chowdhury, Alexandra Sutter, Abdulkader S. Hanbazazah, Anas Ahmed, Jae-Joon Lee, **Muhammad Abdel-Shakour**, Nicolas Leclerc, Ryuji Kaneko and Ashraful Islam. "Cross-Conjugated BODIPY Pigment for Highly Efficient Dye Sensitized Solar Cells". *Sustain. Energy Fuels*, **2020**,4, 1908-1914

[2] Waleed A. El-Said, **Muhammad Abdelshakour**, Jin-Ha Choi and Jeong-Woo Choi. "Application of Conducting Polymer Nanostructures to Electrochemical Biosensors". *Molecules*, **2020**, 25(2), 307.

[3] Md Faiz Shah, Antoine Mirloup, Towhid H. Chowdhury, Sutter Alexandra, Abdulkader S. Hanbazazah, Anas Ahmed, Jae-Joon Lee, Nicolas Leclerc, **Muhammad Abdel-Shakour** and Ashraful Islam. "A near-Infrared Thienyl-Bodipy Co-Sensitizer for High-Efficiency Dye-Sensitized Solar Cells". *Sustain. Energy Fuels*, **2019**, 3, 2983-2989.

[4] **Muhammad Abdel-Shakour**, Waleed A. El-Said, Islam M. Abdellah, Rui Su and Ahmed ElShafei. "Low-cost Schiff bases chromophores as efficient co-sensitizers for MH-13 in dye-sensitized solar cells". *J. Mater. Sci. Mater. Electron.*, **2019**, 30, 5081–5091.

Acknowledgments

First and foremost, all praise be due to God, the Almighty, for his countless blessings and favors.

I would like to express my heartfelt appreciation to **Prof. Ashraful Islam,** Photovoltaic Materials Group, National Institute for Materials Science (NIMS). Prof. Islam placed a great deal of trust in me and provided unwavering support from the start of my studies. He spent an endless time for discussing and explaining the research findings and reviewing my published papers. Always his advice and comments push my work forward. I am grateful for his kind support and am pleased to study under his supervison. It is an honor to learn under his guidance and I am grateful for his kind assistance.

Also, I would like to express my deepest gratitude to **Prof. Kiyoto Matsuishi**, faculty of pure and applied sciences, university of Tsukuba. He gave me continuous advice, encouragement, and all support to successfully pursue my PhD studies. Prof. Matsuishi was always available to answer my questions, review my papers, and provide unlimited support. I believe that my doctoral studies have progressed based of his keen interest and wisdom.

I would also like to thank all the present and past Matsuishi lab members for their friendly behavior, technical support and kind help inside and outside of laboratories. I would like to convey my gratitude and profound acknowledgements to my group member at National Institute of Materials Science (NIMS) namely Dr. Towhid H. Chowdhury, Mr. Md. Abdul Karim, Mr.Yulu He, Mr. komyia-san and Ms. Harue Nagata

I am highly thankful to the Egyptian Ministry of Higher Education and Scientific Research for financial support through Egypt− Japan Education Partnership (EJEP), the 3rd call.

Finally, I would like to thank my parents and my family for their encouragement, patience, sacrifice and unconditional love during my work. I would like to thank my wife Mai Ali Mahmoud

Mohamed Khashabafor her sacrifice, patience, care, love, support, knowledge that providing me the wisdom to pursue my Ph.D. degree throughout all these years. I would like to send my love to my dear son Ali who born these days in Egypt and I couldn’t see him because I am doing my PhD studies in Japan. I hope to see him soon and tell him how much I love him and how I am happy that he came into our life. I wish you all success in your life, my dear son Ali.

Muhammad Abdelshakour Muhammad Youssef

February, 2022

Tsukuba, Japan